CLUSTERING FLYASH PARTICLES USING IMAGE

PROCESSING TECHNIQUES

By

Ali Asmari

Bachelor of Science in Mechanical Engineering
Ferdowsi University of Mashhad
Mashhad, Khorasan Razavi, Iran
2009

Master of Science in Mechanical Engineering
Oklahoma State University
Stillwater, Oklahoma
2011

CLUSTERING FLYASH PARTICLES USING IMAGE

PROCESSING TECHNIQUES

Dissertation Approved:

Dr. Lawrence L. Hoberock

_____

Dissertation Adviser

Dr. Jay C. Hanan

_____

Dr. Gary E. Young

_____

Dr. Damon M. Chandler

_____

ACKNOWLEDGEMENTS

I would like to express my deep appreciation and gratitude to my advisor, Dr. Lawrence Hoberock, for the patient guidance and mentorship he provided to me. I am truly fortunate to have had the opportunity to work with him. I would also like to thank the members of my committee for their contributions and feedback to this work.

I would like to thank my fellow graduate students—those who have moved on, those in the quagmire, and those just beginning—for their support, feedback, and friendship. I wish to extend my appreciation to my friends who have always been there for me and made my time memorable here.

Most importantly, I wouldn't have been where I am right now, without the sacrifices made by my parents. I wish to express my sincerest thanks for all their supports and encouragement and would like to dedicate this work to my dad, Mr. Abbas Asmari and my mom, Mrs. Najmeh Kamali and my little brother, Navid.

Name: Ali Asmari

Date of Degree: JULY, 2014

Title of Study: CLUSTERING FLYASH PARTICLES USING IMAGE PROCESSING
        TECHNIQUES

Major Field: MECHANICAL AND AEROSPACE ENGINEERING

Abstract:
Fly ash is one of the residues generated in combustion, and comprises the fine particles that rise with the flue gases. In the US about 43% is recycled and is often used to supplement Portland cement in concrete production. Fly ash can improve the concrete's mechanical properties and decrease cost. Depending upon the source and makeup of the coal being burned, the components of fly ash vary considerably. These variations affect the quality of the final product. Accordingly it is important for cement manufacturers to know the amount and type of the components in these particles.
The objective of this project is segmentation of images of fly-ash particles acquired using a Micro computed Tomography (µCT) imaging device. A set of grayscale images is produced, with each image representing a particular slice of the particle. The desired segmentation operation should identify particles and label regions of a given image based on "similarity", as perceived by human observers. Two techniques are proposed for segmenting different phases of material in these images.
The first technique uses Contrast Stretching and Histogram Matching and is based solely on the gray scale value of the pixels in the image slices. But some of the segmented regions, although having the same gray value, contain a different composition of material and show up with a porous texture in µCT images. Distinguishing these regions by using only the Gray value produces inaccurate results.
In the second proposed technique, Circular Gabor Filters (CGF) are used to segment the regions of impurity with porous textures in the cross section of the particle. We have also proposed a technique for designing the CGF such that when applied to the gray scale images, the filter passes the porous regions of components accurately, while blocking non-porous regions.
By combining these techniques, we have developed a program that is able to segment different types and regions of impurities in the cross sections of a flyash particle based on their gray values and textures. Using AMIRA software we then create 3D models of these particles, presenting the locations and sizes of different phases of material.

TABLE OF CONTENTS

LIST OF TABLES

LIST OF FIGURES

Figure   Page

Figure   Page

CHAPTER I

INTRODUCTION

1.1 – Objective of the Project

The objective of this project is segmentation of images of fly-ash particles acquired using a Micro

Computed Tomography (μCT) imaging device (images supplied by Dr. Jay Hanan, Associate

Professor, School of Mechanical & Aerospace Engineering, Oklahoma State University and Dr.

Tyler Ley, Associate Professor, School of Civil and Environmental Engineering, Oklahoma State

University). Each particle produces a set of grayscale images, with each image representing a

particular slice of the particle. The desired segmentation operation should identify particles and

label regions of a given image based on "similarity" as perceived by human observers. While a

feature set that will facilitate the measurement of such similarity is not readily available, it is most

likely that a feature set based on pixel intensity, position, and texture values would suffice.

1.2 – Fly-Ash Particles

Fossil-fuels are burned at high temperatures to produce heat and power for electricity generation

and other industries. At temperatures of up to 1750 °C [1] and at a rate of heating of approaching

approaching $10^4 °C \ s^{-1}$ [2], the droplets, or pulverised grains of fuel, are efficiently burned, even though they remain in the furnace for only a matter of seconds. The products of this combustion are porous spheroids composed primarily of elemental carbon [3] and fused inorganic particles formed from the mineral component of the original fuel [4]. These spheroidal carbonaceous particles (SCPs) (Fig. 1) and inorganic ash spheres (IASs) (Fig. 2) are collectively known as fly-ash, the term used to describe the particulate matter within emitted flue-gases.
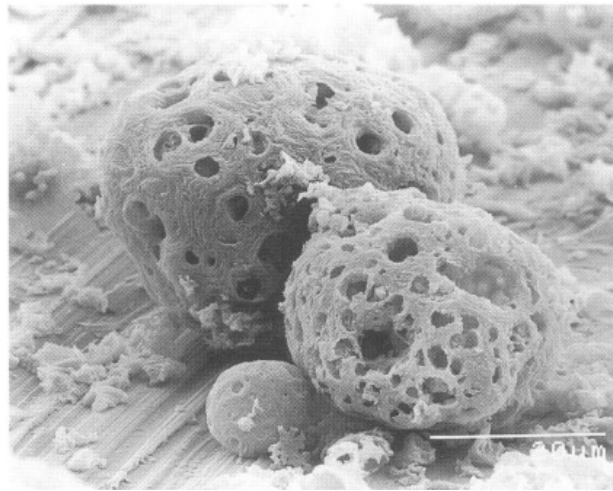
Figure 1.1 – SEM photograph of Spheriodal carbon particles (SCPs) from oil combustion [5]
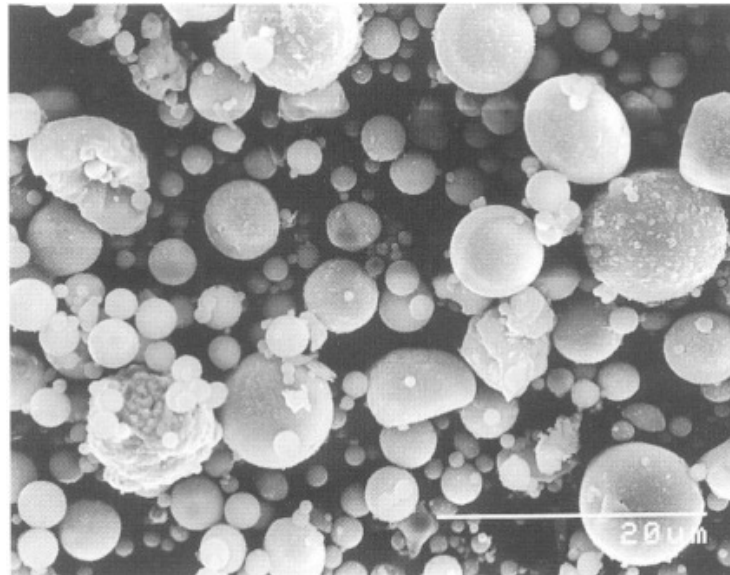
Figure 1.2 – SEM photograph of inorganic ash spheres (IASs) from the combustion of coal [5]

In the past, fly ash produced from coal combustion was simply entrained in flue gases and dispersed into the atmosphere. This created environmental and health concerns that prompted laws which have reduced fly ash emissions to less than 1% of combustion byproducts. Worldwide, more than 65% of fly ash produced from coal power stations is disposed of in landfills and ash ponds. The recycling of fly ash has become an increasing concern in recent years due to increasing landfill costs and current interest in sustainable development. [6]

Fly ash is commonly used as a low cost construction binder for stabilization of soil, partial replacement of portland cement in a concrete mixture, and the predominate binder in a geopolymer concrete. It increases the durability of concrete and can also be used to shrink its environmental footprint by reducing the amount of portland cement in the mix. Nearly a ton of carbon dioxide is emitted in the production of each ton of portland cement, while fly ash is a byproduct of energy generation. Mixes in which up to 25% of the cement is replaced by fly ash are quite common, and some designers are specifying over 50% substitution for certain applications [7].

Despite the widespread use of fly ash particles in concrete, many unknowns remain that need to be answered to increase the applicability of fly-ash particles. High-volume fly ash mixes must be tested before each application, because the chemistry of fly ash is more variable than that of portland cement. Fly ash can either act as a supplementary binder or through a secondary pozzolanic reaction combine with the alkaline pore solution and calcium hydroxide, depending on the properties of the fly ash. Substitution levels for portland cement in a concrete mixture are commonly limited to 20% by mass. [8] This limit is imposed because fly ash is not a manufactured material, and therefore not all sources have the same performance in concrete. If this material was better understood, usage levels might be increased. Fly ash cement mixtures must be managed differently as they cure, because they tend to cure and gain strength more slowly than mixes with more cement.

1.3 – Literature Review

1.3.1 – Improved unsupervised clustering [9]

Venu Lolla [9] proposed a method for clustering all the data points in a dataset and applied his method to the clustering of fly-ash particles. It is known that data can display different structures at different scales [10]. The term "scale" as applied to a given dataset can be loosely interpreted as the size of the smallest spatial structure that can be perceived from the dataset. Any structure smaller than a given "scale" will be suppressed in the rendering of the data at that scale. Since clustering can be interpreted as a method for detecting structure present in the data, different cluster configurations may be detected at different scales. For example, at very large scales all the data will be treated as one cluster, and at very small scales each data point can be treated as a cluster. Meaningful structures, and thus meaningful clusters, will be perceived when operating at the "right" scale(s) for the data.

Lolla's method [9] uses The Watershed Algorithm for clustering. The Watershed Algorithm borrows its intuitive idea from geography, mainly that when a landscape or a topographic relief is flooded by water, water collects in catchment regions, and the catchment regions are divided by watershed lines [11]. The method [12] proposes that a grid be constructed over the feature space and then a density function be defined over the grid. The density of each cell of the grid is treated as a height. Thus the density function takes on an interpretation of a landscape (3–D landscape for 2–D dataset). This landscape is then inverted and subjected to the Watershed Algorithm. As a result of the Watershed Algorithm, the minima in the inverted landscape, corresponding to the high density regions in the grid, are detected. Thus clusters are implicitly defined as regions of high density in the feature space, and are marked by corresponding catchment regions in the inverted landscape. The number of catchment regions found is taken to be the number of clusters present, and the catchment region itself represents the region spanned by the corresponding cluster.

Figure 1.3 (a), (b) and (c) show sample slice images of three fly-ash particles. As can be seen in these figures, the μCT (Micro X-Ray Computer Tomography) imaging process produces images with regions of different grayscale and texture. These different regions correspond to different chemical compositions present in the particle.
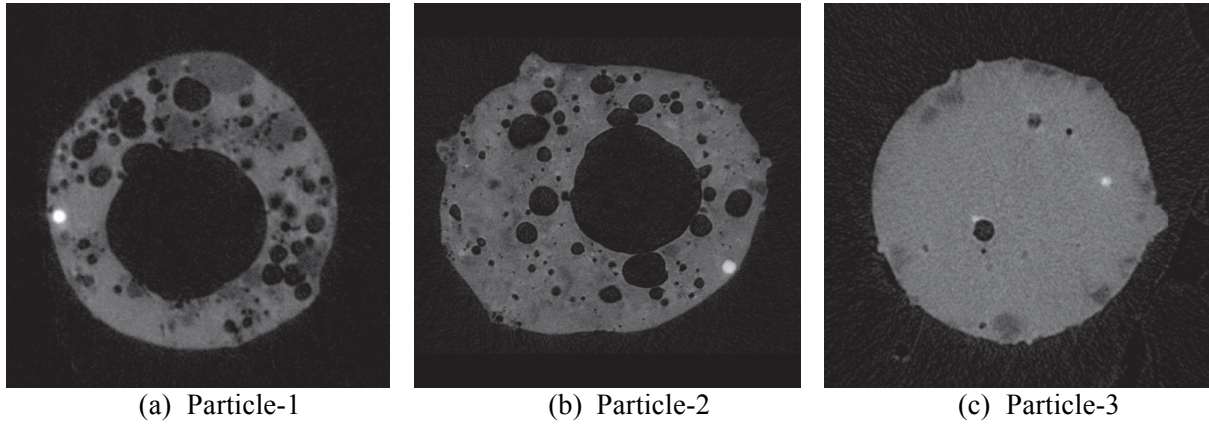
(a) Particle-1   (b) Particle-2   (c) Particle-3
Figure 1.3 – Sample images of slices of three fly-ash particles

The Clustering Algorithm of Lolla [9] was employed on the images of Particle–1. The grayscale values of the pixels in the image were supplied as input to this clustering algorithm. For Particle–1, the results are presented in Fig. 1.4, showing very reasonable segmentation. However, for Particle–2 and Particle–3, the clustering algorithm did not correctly detect the number of phases present in the particle. The failure of the method in clustering these two slices is due to the particle having predominantly large proportions of one phase as compared to other phases. In other words, grayscale values of the pixels alone are not sufficient to determine the phase associated with a particular pixel in Particle–2 and Particle–3 [9].

By visual examination of the images, Lolla suggested that a texture-based feature set might probably separate the phases better. However, attempting to employ the clustering algorithm on a Gabor filter-derived texture data encountered insurmountable computational difficulties.
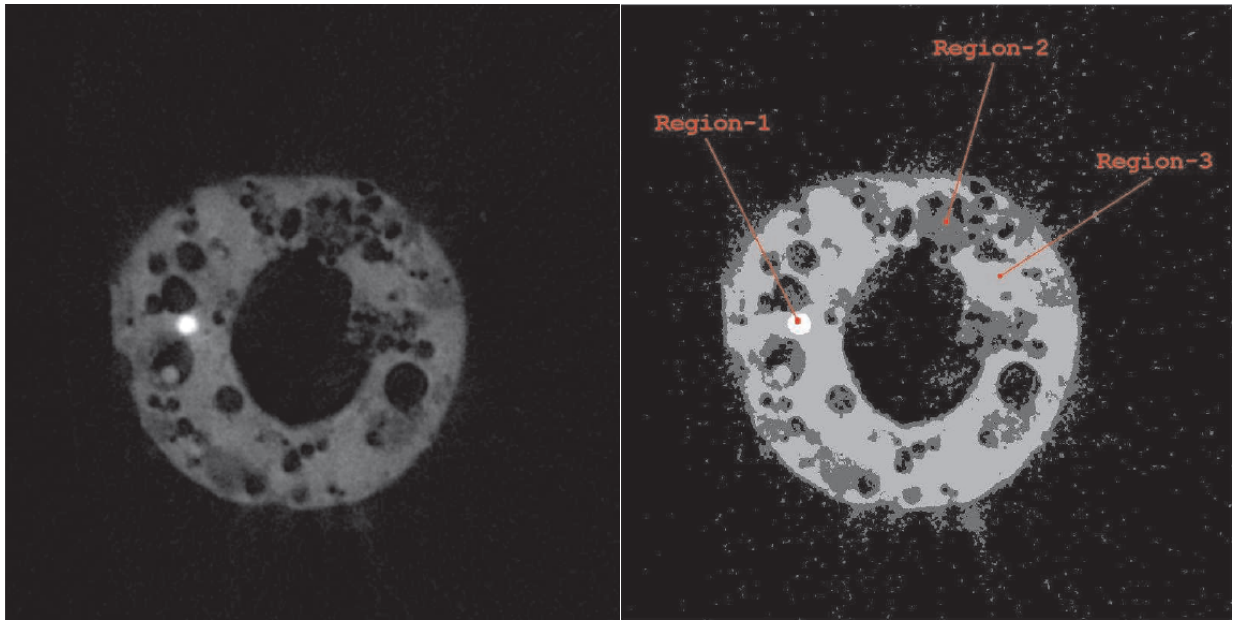
(a) Original Image   (b) Segmented Image (3 regions)

Figure 1.4 – Original and Segmented slice images – Particle-1

1.3.2 – TACCo (Tomography Assisted Chemical Correlation)

A common approach for segmenting the μCT data sets is to choose a range of gray values that corresponds to different constituents in the material. But because of the overlap between different constituents in μCT results of fly-ash particles, it is very difficult to set these ranges and perform segmentation [13]. Figure 1.5 shows the grayscale histogram of a μCT result of a slice of a flyash particle. This graph represents the frequency of pixels versus the gray value. As stated before, the gray values in this graph correspond to the chemistry of the material. From this data, it is suggested that there are two primary phases, and it is not possible to rationalize a segmentation of any other material.

6
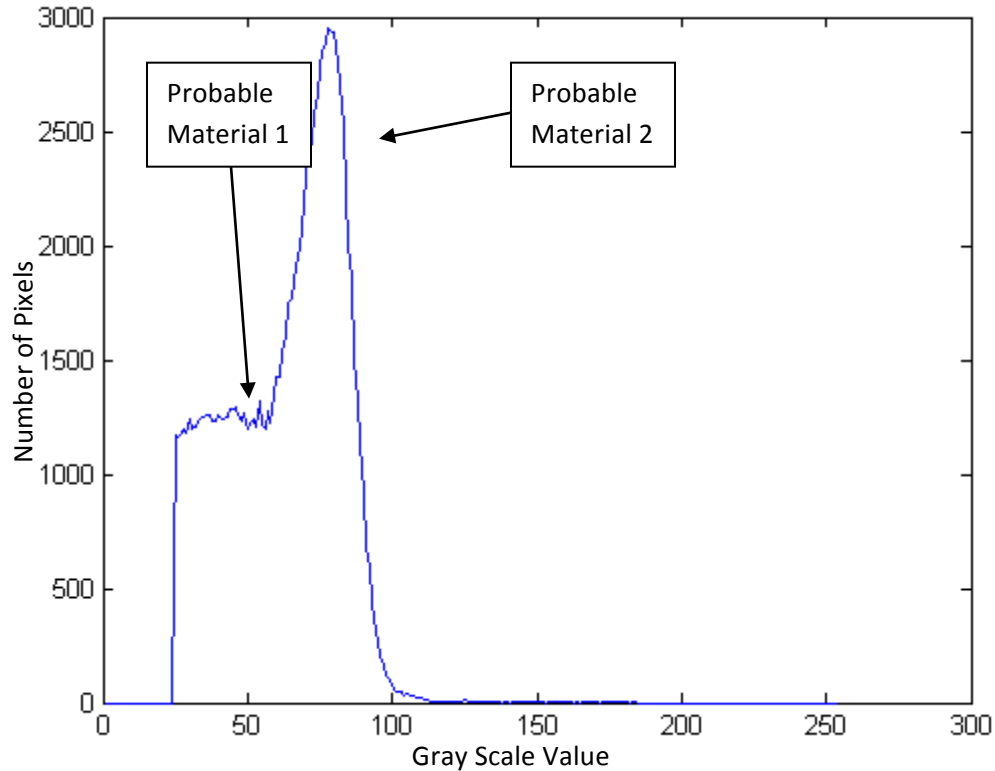
Figure 1.5 – Grayscale histogram of a flyash particle slice showing the number of phases [13]

In this method, called Tomography Assisted Chemical Correlation (TACCo)[13], by using a combination of electron microprobe based electron microanalysis (EM) and micro X-ray computed tomography (μCT), differnet chemical phases are identified.

Electron microprobe analysis (EMPA) [13], also called electron probe microanalysis, is an analytical technique that is used to establish the composition of small areas on specimens. EM is one of several particle-beam techniques. A beam of accelerated electrons is focused on the surface of a specimen using a series of electromagnetic lenses, and these energetic electrons produce characteristic X-rays within a small volume (typically 1 to 9 cubic microns) of the specimen. The characteristic X-rays are detected at particular wavelengths, and their intensities are measured to determine concentrations. All elements (except H, He, and Li) can be detected because each element has a specific set of X-ray wavelength that it emits. This analytical technique has high spatial resolution and sensitivity, and individual analyses are reasonably short, requiring only a minute or two in most cases [14]. However

in order to obtain valid data with this technique, a sample must be polished, coated with a conductive

coating, and imaged in a vacuum. While this technique is useful, it destroys the sample, allows only

surface observations to be made, and is a restrictive viewing environment. Figure 1.6 shows EM

result of a fly ash particle [13].
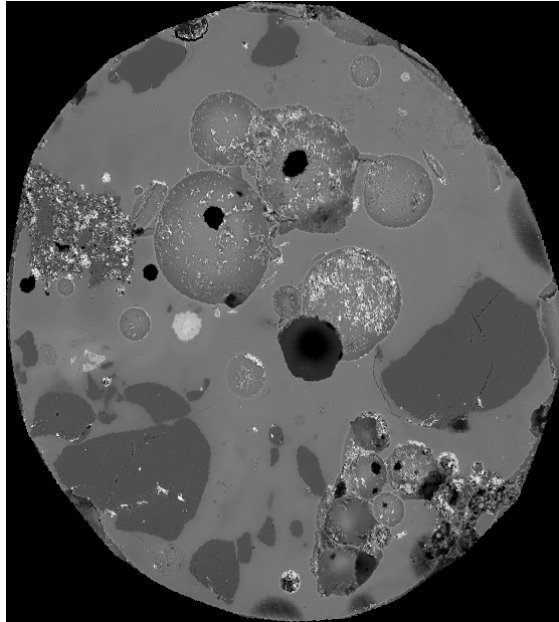
Figure 1.6 – Electrone Microanalysis (EM) of a flyash particle [13]

In the TACCo method [13], by fusing the EM and µCT datasets and using a symmetric and

statistically based approach, the limits of segmentation can be determined. In this method, the µCT

results are correlated with the EM results. By assuming the data to be normally distributed, Gaussian

statistics are used to find the mean and standard deviation for the gray scale value of each phase.

These values are then used to find acceptable segmentation ranges. First, the materials that are most

prevalent in the cross section are found, and using the standard deviation, an acceptable gray range is

selected.

Using this method the pixels in an image will be categorized based on their gray value, independent

of their location. This means that if a pixel in the region of material A has a gray value in the material

B gray region it will be segmented and counted as material B. Accordingly after segmenting the entire

image, these misclassifications will likely give inaccurate results about the volume of each material in the fly ash particle.

1.3.3 – Segmentation of Ultrasound Images Using Gabor Filtering [14]

Among all the popular image modalities, Ultrasound Imaging (US) is widely used for real-time diagnostic situations. Image segmentation is often the first step for image analysis and is a key basis of many higher-level activities, such as visualization, compression, and medical diagnosis. US images contain strong speckle noise, such that attenuation artifacts and organs don't appear homogeneous, rendering it difficult to segment these images. Many creative methods have been adopted for proper segmentation of US images [15]. However it is difficult to classify human body organ tissues using shape or gray level information because the shape of each organ is not consistent throughout all slices of medical images, and the gray level intensities overlap considerably for soft tissues. However, texture information in US images can be used to discriminate among different organ tissues. In this work, a linear Gabor filter is applied to the gray scale image, and the responses of different patterns in the image belonging to different organs in the body are different, which helps cluster these regions using various segmentation techniques. This procedure is shown in Figure 1.7 for an US scan.

a b c   Figure 1.7 – An US image of a human liver containing a cyst; (a) Original Image; (b) Gabor Filtered Image; (c) Segmentation Result

1.3.4 - Texture Segmentation Using Multichannel Gabor Filtering [16]

In [16] the authors extended the single-channel method for texture segmentation to a multi-channel method by using multiple Gabor filters. Based on this extension, their work deals with multi-channel texture segmentation of gray scale and color images. Specifically, the project deals with multi-channel texture segmentation of color and gray scale images to find out the different textures present in composite images. The paper addresses the design of multiple Gabor filters for segmenting multi-textured images. The authors designed a Gabor filter bank that is used to decompose the input image into a number of filtered images by using a set of spatial frequency orientations, covering the frequency space of interest, capturing texture information as much as possible. In the segmentation stage of the project, the authors proposed a method for fusing the results to obtain best results based on the application, while avoiding aliasing. The stages of this process are demonstrated in Figure 1.8.

Original Image

Bank of Gabor Filters

Filtered Images

Feature Extraction

Images after
Feature Extraction

Clustering

Segmented Image
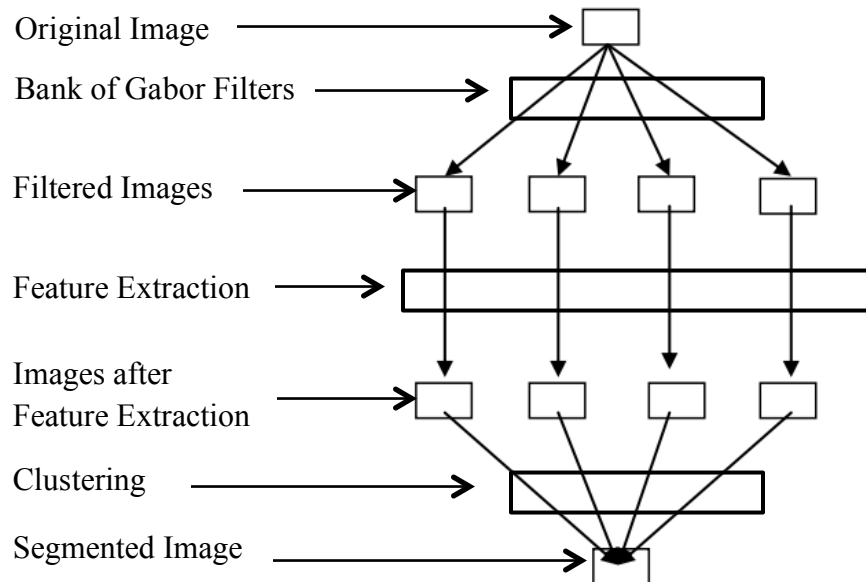
Figure 1.8 – Texture Segmentation, Adapted from [16]

In this method the Gabor filter bank was designed by considering different frequencies and orientations as the image is passed through the bank, and is then decomposed into a number of filtered images. Then, features are extracted from the filter bank outputs. In an image, the low

frequency components represent contrast and intensity, whereas the high frequency components represent edges and sharp details present in the image. By applying smoothing, all low frequency components are allowed and high frequency components are attenuated. In other words the contrast and intensities are highlighted, and edges and sharp details are attenuated.

The final step is clustering the pixels; after clustering each pixel is labeled to produce the segmented image. The authors have used the K-mean algorithm which is as follows:

1) K random centroids are initialized.

2) Each sample is assigned to the nearest centroid

3) Centroids (means) of K-clusters are calculated

4) If centroids are unchanged, end; otherwise go to step 2

When clustering is completed, each pixel is labeled with its respective cluster, producing the segmented image.

The Results of segmentation using this method on sample images are shown in Figures 1.9 and 1.10.

(a)   (b)
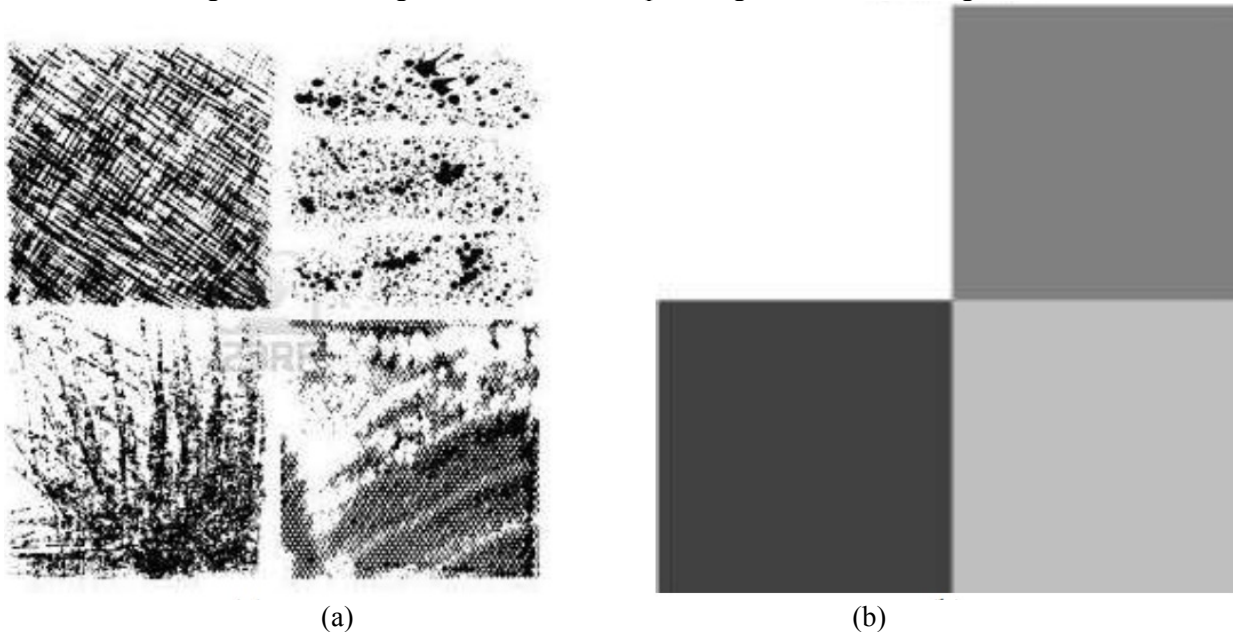
Figure 1.9 – Segmentation of a four texture gray scale image; (a) Input image; (b) Segmented image [16]

<div align="center">(a)   (b)</div>
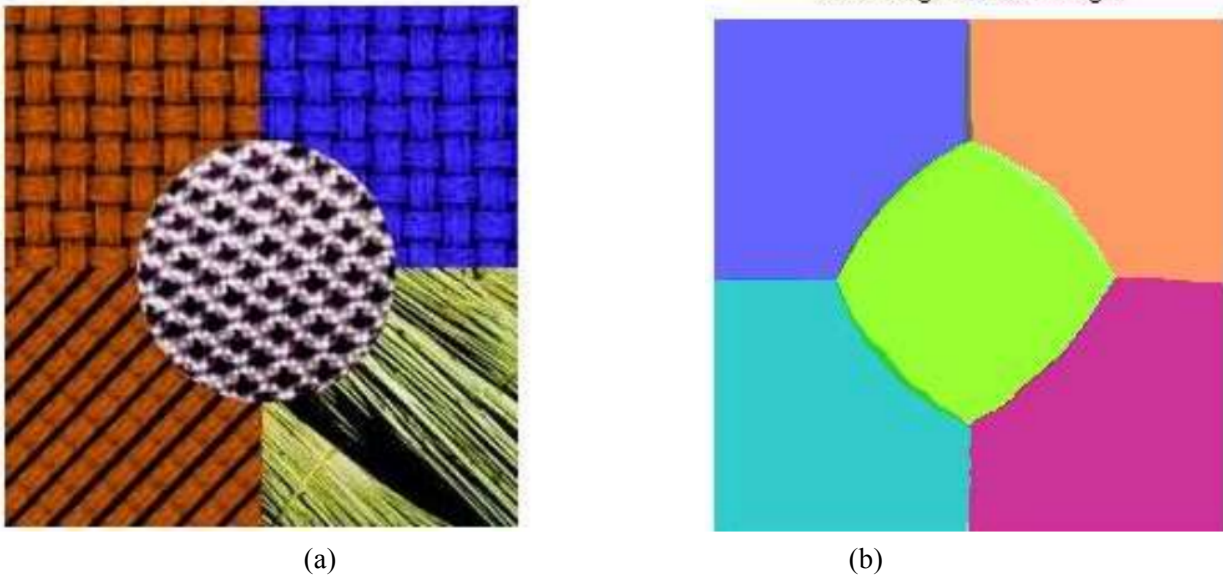
Figure 1.10 – Segmentation of a five texture image; (a) Input image; (b) Segmented image [16]

These results show that the multichannel Gabor filtering acheme is suitable for the segmentation of multi textured images, and also clear discrimination of the edges of the textures.

This technique is very applicable for cases in which different patterns in the image are very distinct from each other. In flyash particles, since the patterns of different phases of material are very similar, The K-mean technique will likely not properly converge to the centroids of different phases of material.

1.3.5 – Gabor filter-based feature extraction for character recognition [17]

In this project a new method for character recognition using Gabor filters with gray scale images is proposed. This work illustrates the advantages of using Gabor filtering in images with noisy backgrounds and complex textures over traditional edge detection techniques. Methods such as the discrete cosine transformation (DCT) or moment transform [18] and direct edge detection from the gray scale image [19] are very sensitive to illumination variance and character distortion. However

the authors of the paper claim that their proposed feature extraction method based on Gabor filters

solves this difficult problem.

The various steps of this method are shown in Fig 1.11. Gabor filter-based feature extraction is

divided into four sequential parts: (1) design and apply multi directional Gabor filters to extract the

information about the edges in the image; (2) adaptively regulate the outputs of Gabor filters to

remove background and illumination noise; (3) extract histogram features from the filtered images;

(4) compress histogram features to quantitative values for recognizing different objects and shapes in

the image. In this project the authors are interested in recognizing alphabetic characters in

handwritten texts.
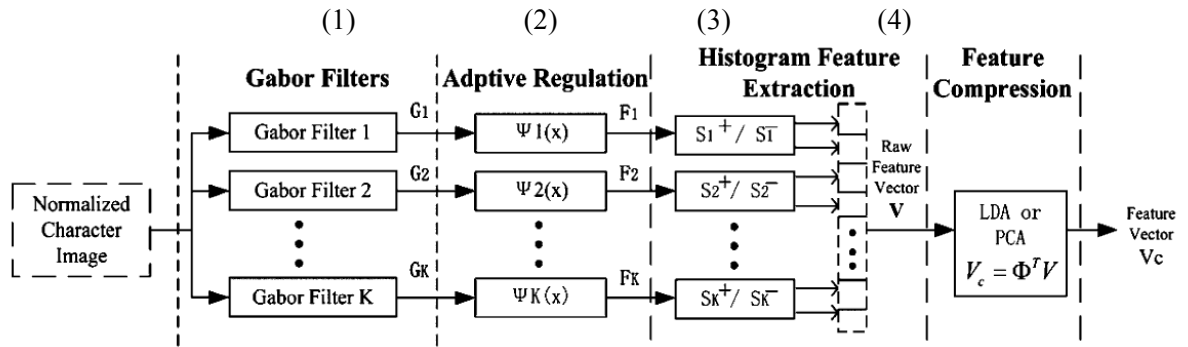
Figure 1.11 – The flowchart of the Gabor filters-based feature extraction method [17]

The authors applied the method on printed Chinese character images, using the 3755 characters in

commonly used fonts with 200 sets of printed samples. The reported recognition accuracy ranged

from 74.41% to 99.87%.

This technique is very good for detecting regions with patterns in certain directions. The Gabor filter

bank in this technique is composed of different sizes of Gabor filter in different directions. Since the

pattern of the phases of material in the images of cross sections of flyash particles are not directional,

the filter bank used in this technique will not create a meaningful output that can be segmented.

1.4 – Literature Review of Histogram Matching

Histogram matching is transforming a grayscale or truecolor image so that the histogram of the output image approximately matches the histogram of a reference image.

1.4.1 - Merging radiometric grids using histogram matching [20]

Large-scale compilations of airborne geophysical data are an important part of regional-scale mineral exploration. In most cases, the compilation involves merging datasets of varying quality, acquired over a long period of time. A major problem in merging radiometric datasets is that many older surveys were flown with spectrometer systems which had not been calibrated, making comparison between adjacent areas difficult. The modern technique suggests a holistic approach to grid merging, where a number of grids are adjusted in a least-squares sense rather than piecemeal. Base-level shift and scaling factors are calculated for each grid and then the edges are feathered. The merged grids allow comparison of radiometric signatures from one area to another. However, even with modern calibrated spectrometer surveys, soil moisture differences between surveys introduce scaling errors into the estimated radioelement concentrations.

Merging radiometric data grids by using a base level shift and a scaling factor can give excellent results when the difference between two surveys consists of only a base level shift or a scaling factor. However, in practice the relationship between the two datasets may be more complicated, and can take on any form (like differences in statistical properties due to different amounts of moisture in the soil). Histogram matching makes no assumptions about the statistics of the datasets or of the relationship between them. Fig. 1.12 shows a comparison of merging two grids from the Karelia Craton in Eastern Finland. The northern grid is part of a survey flown in spring 1976 using a DC-3 platform, flown east–west at a nominal elevation of 30m with 200m line spacing. The southern grid is part of a survey flown in summer 1987 using a Twin Otter platform, flown east–west at a nominal elevation of 30m with 200m line spacing. The north–south overlap between the two 50m mesh grids

14

is only 600m, providing 7200 data points for histogram generation. In this case, the more recent data, flown at the best time of year were selected as the control dataset. Fig. 1.12A is a K, eU, eTh RGB ternary image, produced by conventional grid merging of the individual radioelement grids. Conventional grid merging has been unsuccessful in matching radioelement distributions with clear differences remaining between the northern and southern grids. Fig. 1.12B shows the results of grid merging using histogram matching. The image in Fig. 1.12B is clearly superior to that in Fig. 1.12A, providing continuity across the join of the two grids. Comparison of the histogram-matched data with a summer 2001 high-resolution infill survey shows excellent correlation, suggesting that histogram matching has performed well.

A
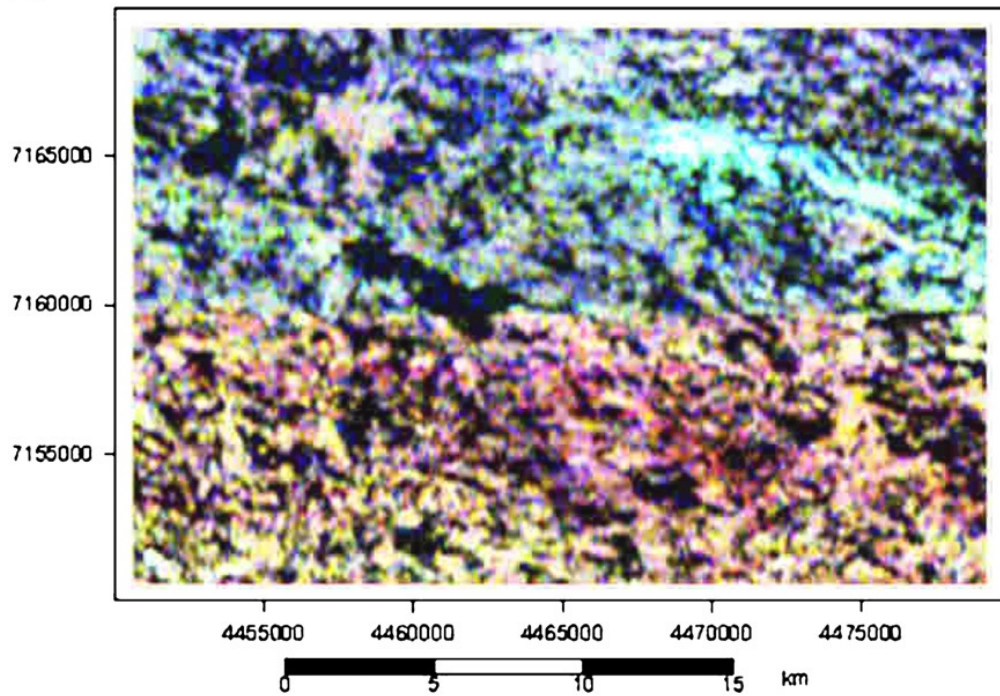
B
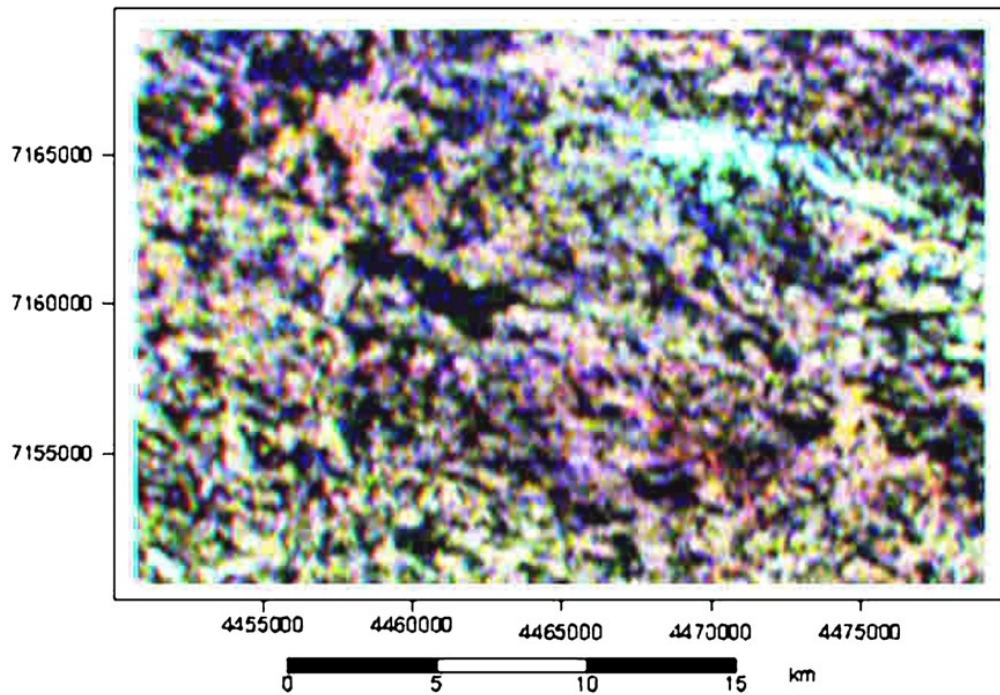
Figure 1.12 (A) Standard grid merge radiometric ternary image, K = red, eTh = green, eU = blue. Black = low in all three radioelements. White = high in all three radioelements. (B) Histogram-matched grid merge radiometric tenary image, K = red, eTh = green, eU = blue. Black = low in all three radioelements. White = high in all three radioelements [20]

1.4.2 - Cyclone intensity estimation using similarity of satellite IR images based on histogram matching approach [21]

IR imagery from geostationary satellites is used widely for the estimation of intensity of Tropical Cyclones (TCs) due to the continuous temporal and spatial monitoring. However, deriving direct information about TC inner core structure and evolution from infrared (IR) images becomes difficult because upper level cirrus clouds are opaque at typical IR wavelengths. This is the main problem in the images of TC, which displays a central dense overcast (CDO) aloft because the structure of the eye-wall and surrounding rain-bands becomes obscured. Although TC diagnosis and forecasting are challenged by the presence of upper-level cirrus, the frequent sampling and long history of IR data collection have resulted in large-volume archival datasets that allow for calculation of indirect relationships between IR-measured brightness temperature (BT) values and intensity of the cyclone.

A widely applied technique for estimating TC intensity is a subjective technique based on the indirect relationships between cloud patterns and intensity. It employs manual or automated recognition of cloud patterns recognition and empirically based rules to derive an estimate of TC intensity. In general there are two approaches for operational estimation of TC intensity from satellite observations (a) regression of image parameters and TC intensity and (b) using the characteristic patterns, history etc. for estimation of intensity.

In the present study an alternative approach is suggested for estimation of intensity of TCs by comparing a given image of TC to the images of past events. One advantage of the present method is that the spatial distribution of convective features is matched in terms of BT distribution. For this, a database has been prepared using the IR images of cyclones of diverse intensities. Radial and angular histograms of BT values of the images archived in the database were computed and matched to the histograms of IR image of cyclone whose intensity is to be estimated (test image). The intensity of the cyclone in the best matched image from the database is assigned to the intensity of the cyclone in test

17

image. The best matched image is the one that has the least histogram change to match the histogram of the test image.

The 'radial-angular histogram' approach has been employed in this work for image matching. This includes the matching of the radial and angular histograms of the two images. In the radial angular histogram, the image intensity (gray level) distribution is estimated in radial and angular directions. The radial histogram is ideally adapted to inspect the circular regions whose intensity patterns possess circular symmetry. The angular histogram is used to inspect the orientation features. The radial and angular partitioning of a cyclone image is shown in the Fig. 1.13(a).
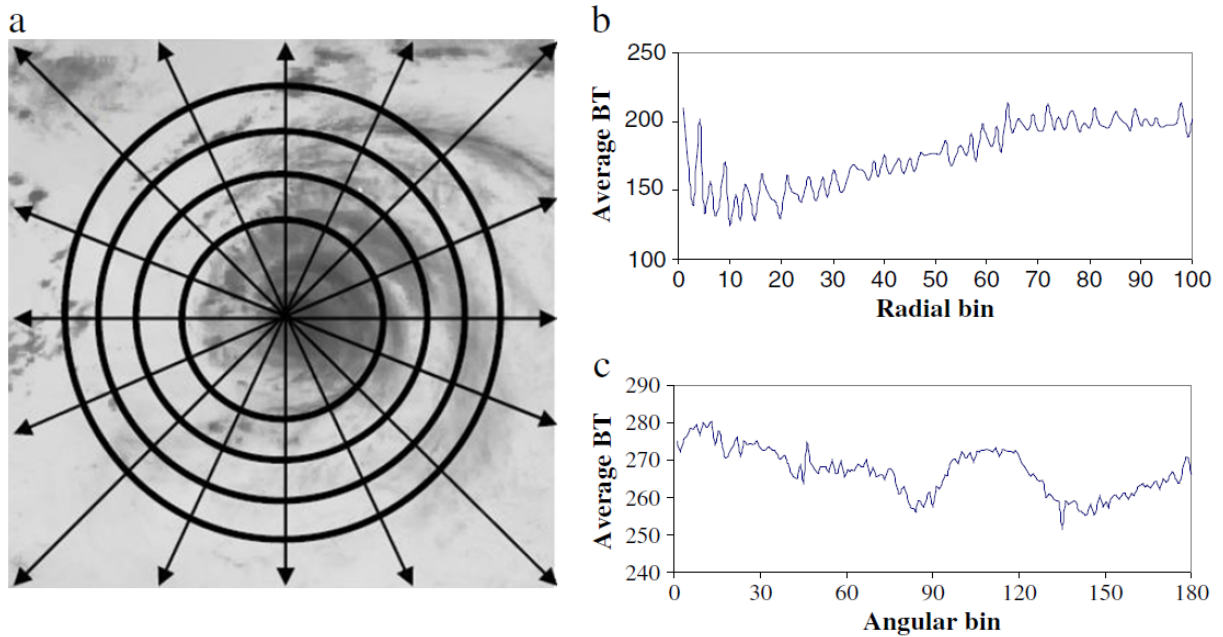
Figure 1.13 – (a) Cyclone images showing the radial and angular partitioning, (b) radial histogram and (c) angular histogram [21]

All the cleaned images of the cyclone from the archived data have been matched using this methodology. Fig. 1.14 shows the pair of six images with different intensities that were matched using the method. The images have been tagged with their date and intensity in kt (YYYYMMDD-INT). It can be seen that the six randomly picked images (top row) with the intensities 35, 43, 65, 95

and 130 kt are matched with images (bottom row) with intensities of 25, 45, 65, 105, and 115 kt, respectively.
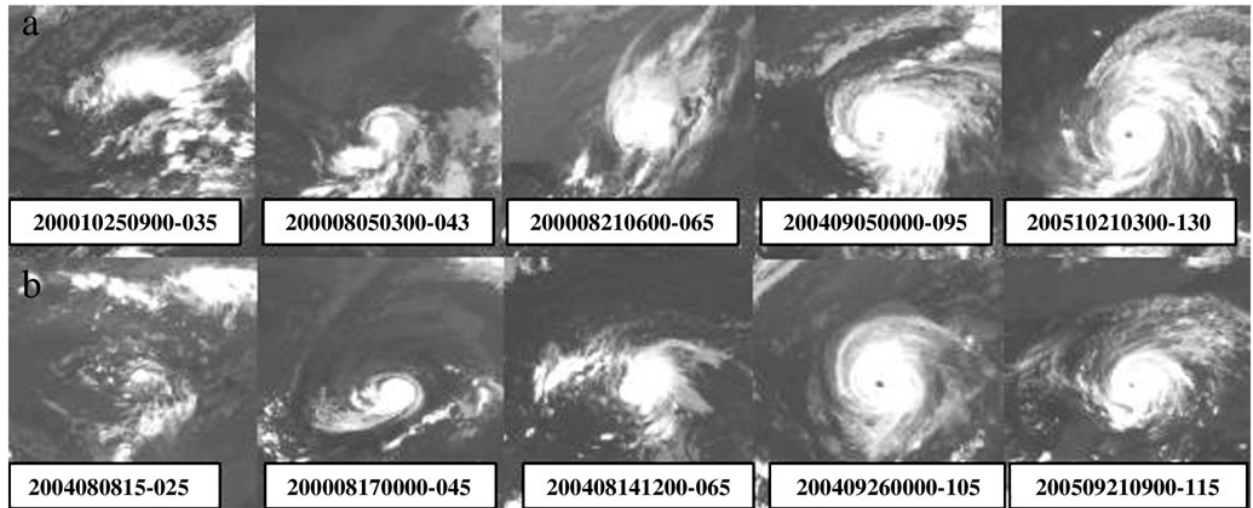
Figure 1.14 – Randomly picked images (top) and the best match image (bottom) [21]

1.4.3 – Contrast enhancement of optical coherence tomography images using least squares fitting and histogram matching [22]

Optical coherence tomography (OCT) is a novel imaging technology that can produce high resolution cross-sectional images of the internal microstructure of biological tissues. The backscattered light is utilized, the intensity of which from the detected specimen is diminished rapidly with the depth, especially for a high scattering specimen. The intensity of the light scattered from the interior of the specimen is much lower than that from the surface, so the deeper internal details are barely seen, and the unprocessed OCT image often has a relatively low contrast.

Histogram matching, which modifies an image histogram in a way, is a method of image enhancement. In this work, the algorithm of least squares fitting [23] is used to fit the histogram of the original image before histogram matching so that parameters of the specified function can be determined without subjective selection. One of the characteristics of many OCT images is that most pixels are in low gray levels, which means a sharp peak at low gray levels exists in the gray level

histogram. The number of pixels falls rapidly on both sides of the peak. According to this characteristic, some typical functions, such as the Gaussian function, can be adopted as the probability density functions (PDF) of the image histogram.

The whole algorithm is performed as follows:

1) Calculate the normalized histogram of the input image.

2) Select a proper function as the PDF of the input image histogram and fit the normalized histogram using least squares algorithm to determine the parameters of the PDF.

3) Adjust the parameter of the PDF of the input image histogram to stretch the width of the PDF and use the stretched PDF to simulate the PDF of the output image histogram.

4) Transform the input image using histogram matching with assumed PDF of the output image histogram.

The PDF of the image histogram can be assumed as a Gaussian function, inverse proportional (IP) function or exponential function, or other functions whose shapes are similar to the image histogram.

In this work, the skin of a human fingertip is used as the specimen for an experiment, which has a size of 180 by 150 pixels and shows an area of 1.8 mm by 1.5 mm. The unprocessed OCT image of the specimen is shown in Fig. 1.15a. Its normalized histogram is shown in Fig. 1.15b. Least squares fitting and histogram matching are implemented to enhance the image of Fig. 1.15a. The processed images of Fig. 1.15a after least squares fitting and histogram matching using Gaussian function, inverse proportional function and exponential function are shown in Figs. 1.16a, 1.17a and 1.18a, respectively. Their normalized histograms are shown in Figs. 1.16b, 1.17b and 1.18b, respectively. It is obvious that the pixels in the densely populated regions of gray levels are "stretched". As they have much higher contrasts, the details can be seen much more clearly.
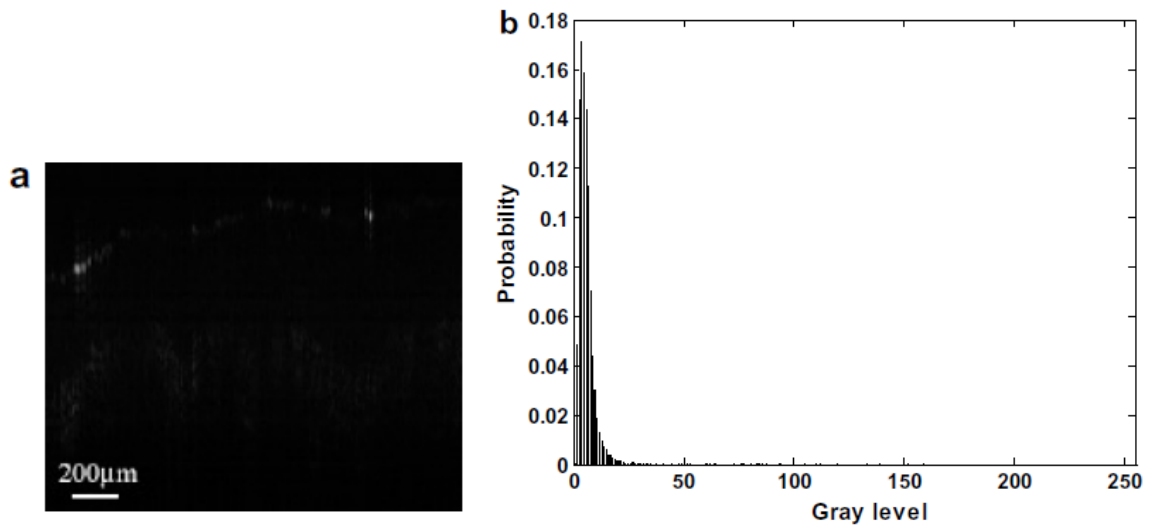
Figure 1.15 – (a) The unprocessed OCT image of the skin of a human fingertip and (b) its normalized histogram [22]
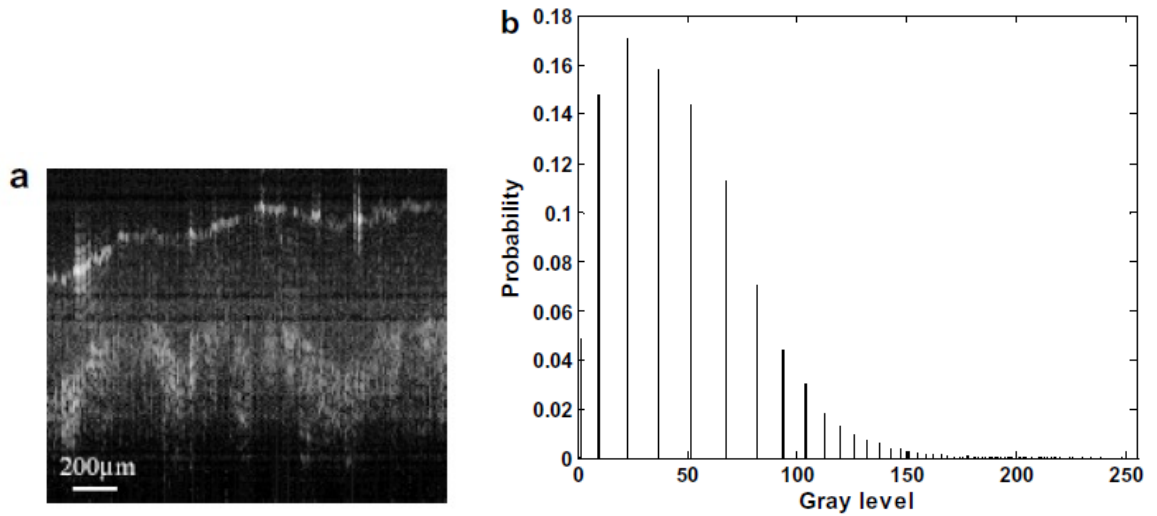
Figure 1.16 – (a) The image after least squares fitting and histogram matching using a Gaussian function and (b) its normalized histogram [22]
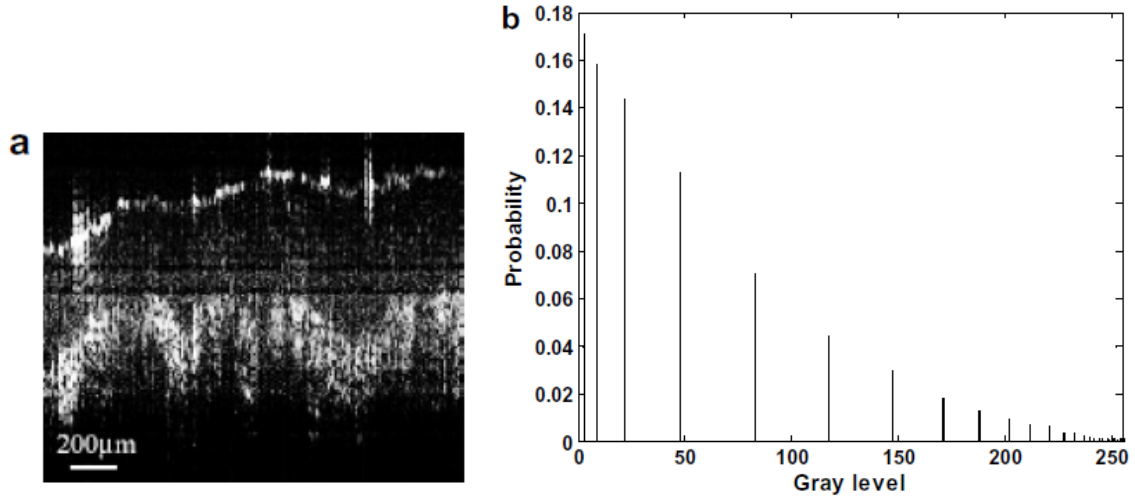
Figure 1.17 – (a) Image after least squares fitting and histogram matching using an inverse proportional function and (b) its normalized histogram [22]
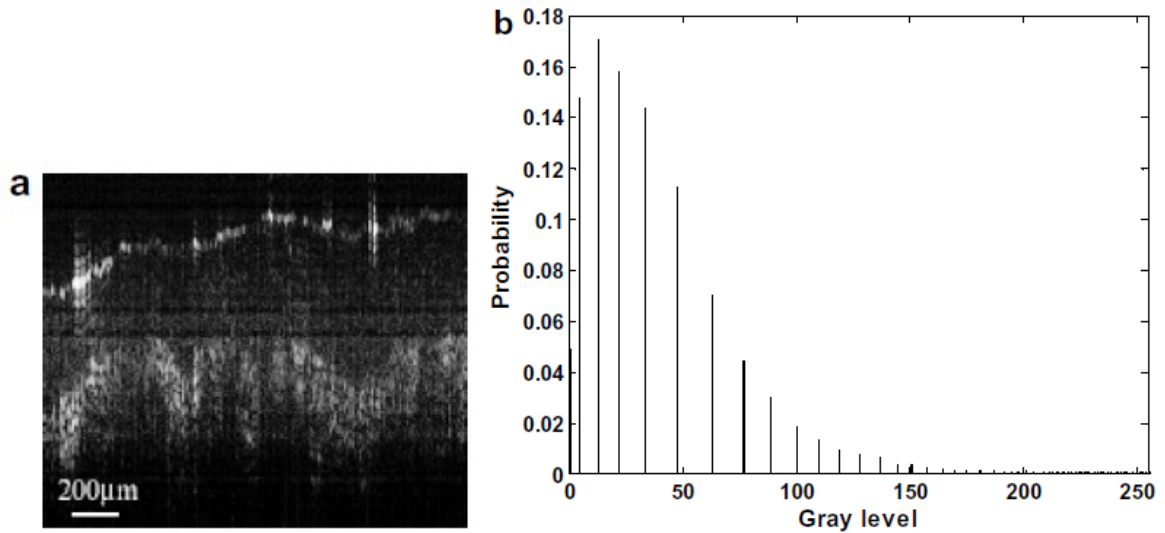
Figure 1.18 – The image after least squares fitting and histogram matching using an exponential function and (b) its normalized histogram [22]

1.5 – Remaining Sections of the Report

In Chapter 2 a segmentation technique using contrast stretching is explained, and a primary

insufficiency of the method to fully segment fly ash particles is explained. Chapter 3 introduces the

approach for segmenting different phases of material based on their patterns in the gray scale image

using circular Gabor filters. In Chapter 4, data post processing stages and combination of all of the

22

introduced techniques are presented. The results of this method, conclusions and proposed future

work are presented in Chapter 5.

CHAPTER II

SEGMENTATION USING CONTRAST STRETCHING

2.1 - Contrast Stretching Technique

Contrast stretching transformation is a well-known basic tool for dynamic range manipulation in image processing [23]. The function s=T(r) illustrated in Fig. 2.1(a) is called a contrast stretching transformation function because it expands a narrow range of input levels into a wide (stretched) range of output levels. The result is an image of higher contrast. In the limiting case shown in Fig. 2.1(b), the output is binary, and the corresponding T(r) is called a thresholding function.

(a)   (b)
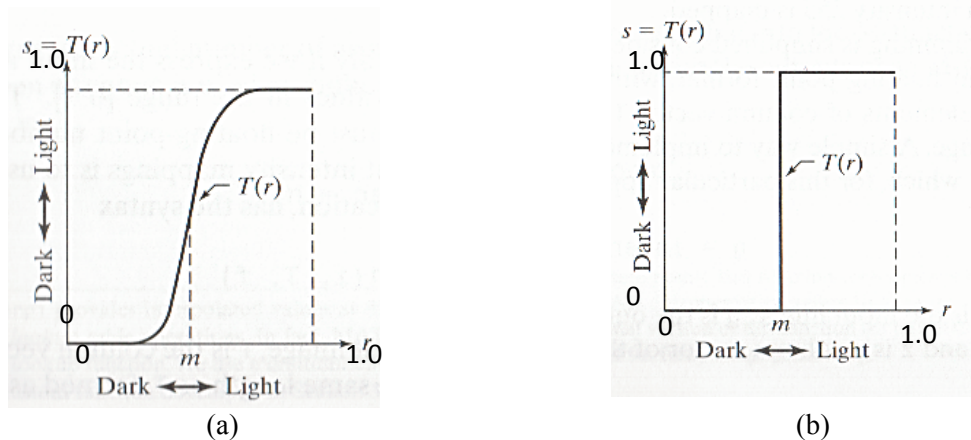
Figure 2.1 – (a) Contrast Stretching Transformation. (b) Thresholding Transformation

The function in Fig. 2.1(a) is given by:

$$s = T(r) = \frac{1}{1+(m/r)^E} \qquad\qquad (2.1)$$

In this equation r denotes the intensities of the input image and E controls the slope of the function. As demonstrated in the Fig. 2.1(a), m is defined as the center of transformation (threshold).

For fly ash particles, we used the contrast stretching transformation to segment different materials, whereby for every input image, we improved the contrast. In our approach, we improve the contrast of the gray scale image with two different thresholds, and the outcome of subtracting the results amplifies the regions of the different phases of material. By changing the contrast in the selected thresholds, the pixels with gray scale values in the threshold range experience the highest change. So by subtracting these contrast stretched images, the remainder magnifies the locations where the different phases of material exist. After subtracting contrast stretched images, in order to segment the particles, we employed a post processing algorithm to remove noise.

The results of amplifying the different phases using the contrast stretching technique are shown in Figure 2.2. In Figure 2.3 the results of segmentation after noise removal stage are demonstrated.

a b
c d
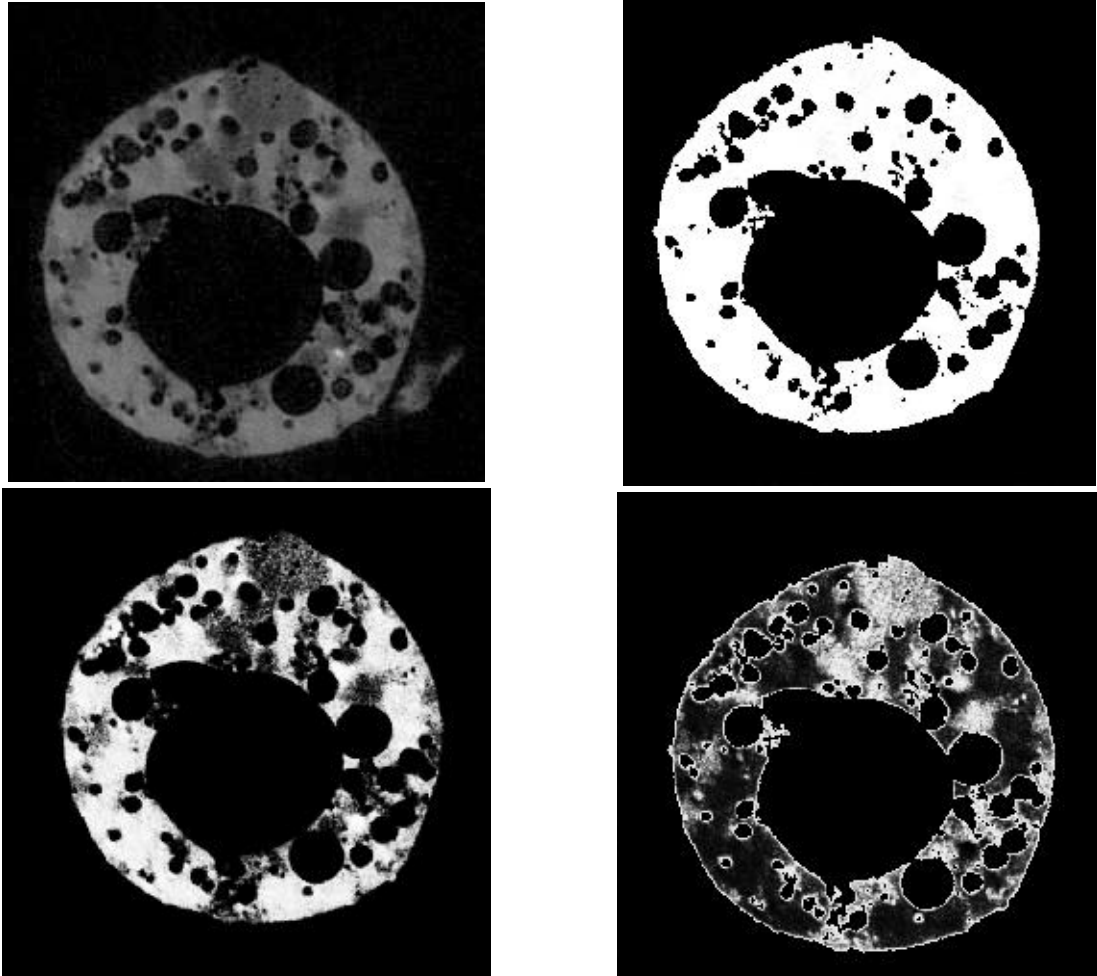
Figure 2.2 – Results of Implementing the Contrast Stretching Transformation;
(a) Original Image; (b) Contrast stretching result with a low threshold value; (c) Contrast
stretching with high threshold value; (d) Subtraction of (b) from (c)
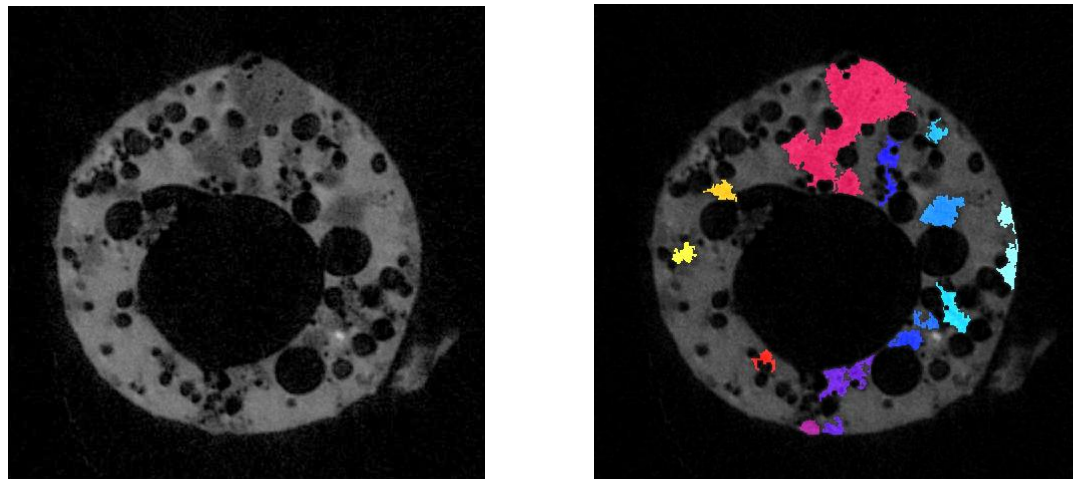
Figure 2.3 - The Original Image (left) and The Clustered Image (right) – Different colors in this
image represent different regions of different phases

2.2 – Difficulties of Contrast Stretching Technique

As explained in the previous section, in order to segment different phases in the cross section of a particle, we improved the contrast level of an image with two different thresholds and subtracted the results. When these thresholds are selected properly, the results appear reasonably accurate compared with manual segmentation. The challenge in this technique is that this selection must be done for every slice separately to achieve good results, and there are images of approximately 400 slices for a single particle to be analyzed. Experimental results show that a single set of thresholds does not segment all the images properly (compared to results from human observation).

Figure 2.4(a) shows a cross section of a fly ash particle. The histogram of this slice after removing the noise is presented in Fig 2.4(b). In this histogram two areas of interest appear. The high peak, marked with the blue arrow in Fig 2.4(b) is formed by the majority of the pixels in the image which contain the major phase having a light gray value. The curve shown in this figure is similar to a Gaussian function in which the left leg is extended. This extension, marked with the red arrow is formed by the pixels of the phases of the material that have slightly darker gray values. Two of the regions in the cross section of the particle that contain these phases are marked with red circles in Fig 2.4(a). The curve in Fig 2.4(b) can be approximated by the summation of three Gaussian functions, similar to the curves shown in red in Fig 2.4(c). Notice that the red curve exhibits three peaks. The summation of the two small Gaussian functions on the left is shown in green and contains the pixel values of the phases of interest with darker gray levels. This curve can be the result of summation of even more than two small Gaussian functions. The region of interest is presented as the summation of only two small Gaussian functions to be able to recreate the histogram of the image as accurately as possible with only a few Gaussian functions for simplicity. In reality, the pixel values of the region of interest (pixels with darker

values) fall into the range of the summation of a multitude of smaller Gaussian functions.
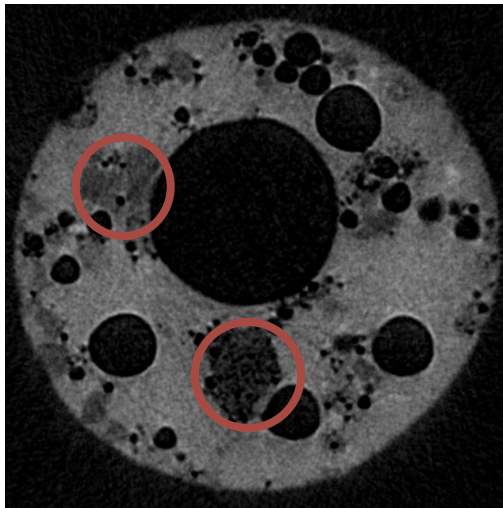
(a) FlyAsh Cross Section
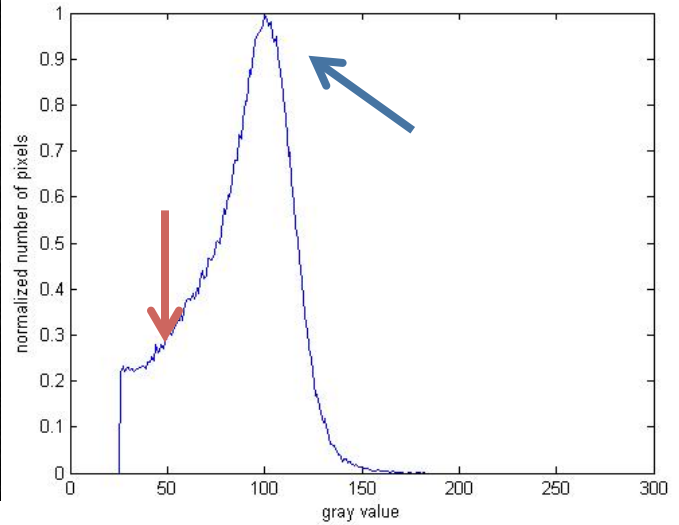
(b) Normalized Gray Histogram After Noise Removal

Figure 2.4 – A sample cross section of the particle with the corresponding gray scale histogram after noise removal
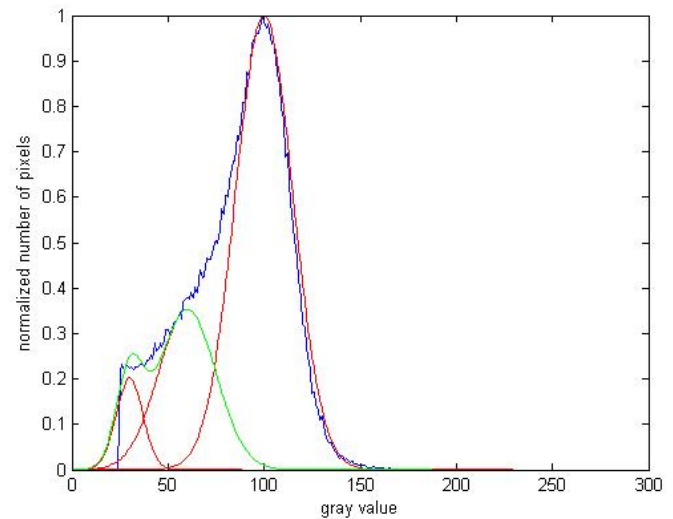
(a) Possible Gaussian Functions Representing Different Phases of Material

The purpose of using the contrast stretching technique, explained in the previous section, is to create more distinct differences in gray values between the phases that created these two areas.

In Fig 2.5 the blue line shows the histogram of the cross section presented in Fig 2.4(a). The red

line in this figure shows the contrast stretching curve (explained in Fig 2.1(a)). This curve was

calculated using Eq 2.1 with a threshold properly selected to divide the phases of material

creating the major areas of interest in the histogram. The contrast stretching curve shown in this

figure will yield the slightly lighter gray values of the pixels that created the major peak (blue

arrow in Fig 2.4(b)) in the histogram, and the slightly darker gray values of the pixels that created

the red arrow area in the histogram (Fig 2.4(a)). This creates a more distinct separation between

the phases in the histogram of that cross section. Fig 2.6 shows the contrast stretched result for

the particle slice in Fig 2.4(a).
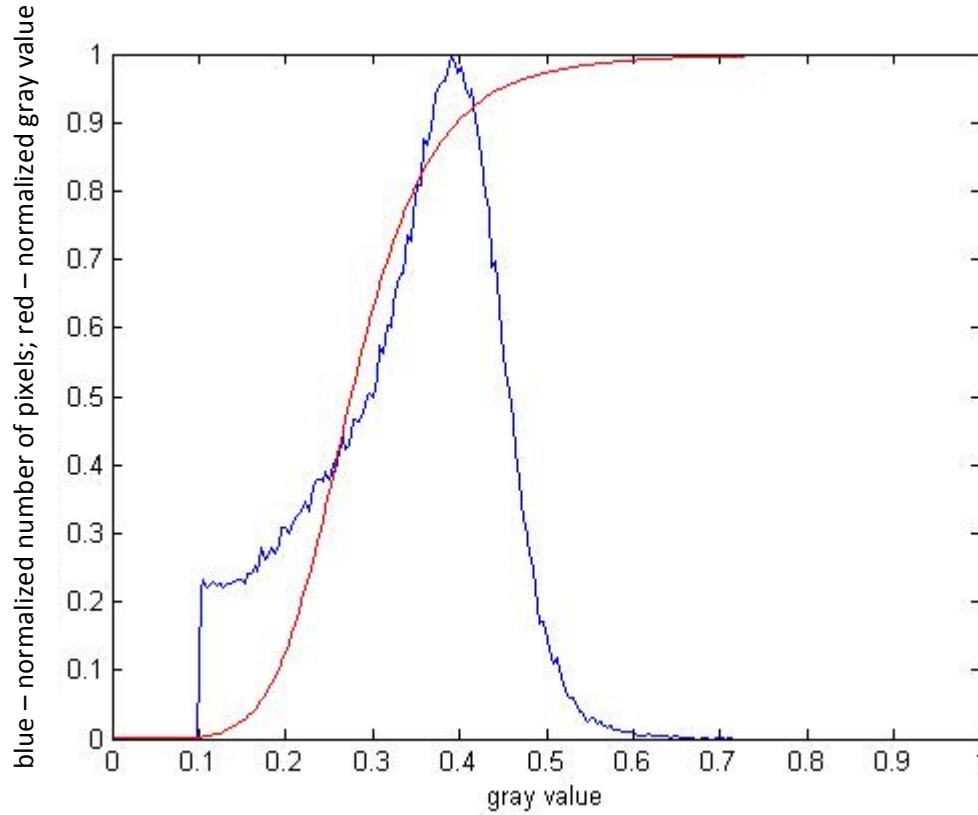
Figure 2.5 – Gray scale histogram (blue curve) and contrast stretching curve (red curve) for a
cross section of the particle
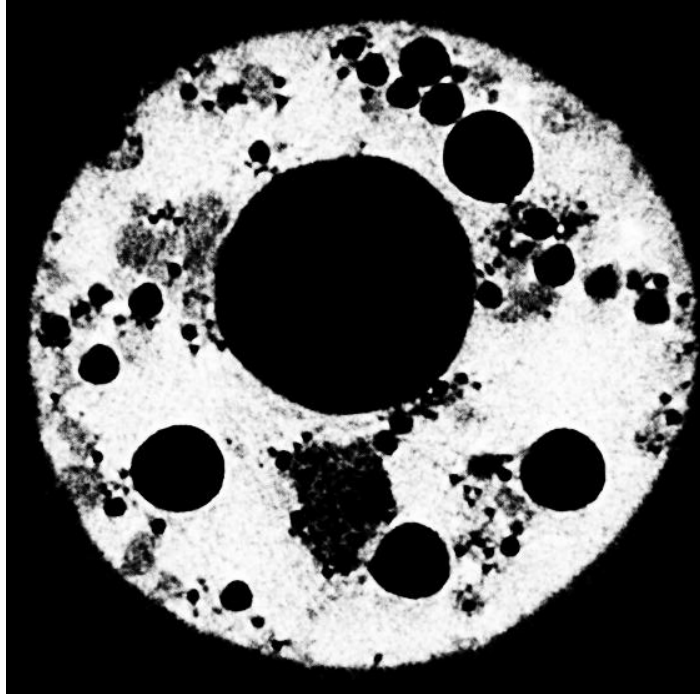
Figure 2.6 – The contrast stretched result for the particle slice in Fig 2.3(a)

The problem with this technique is that if the threshold for contrast stretching is not selected accurately, instead of creating a clear distinction between the phases, the technique will segment the phases incorrectly. In the cross section images of flyash particles, the gray value of different phases are very close together, and if there is a slight shift in the histogram, from one slice to the other, the contrast stretching curve that was working accurately for one slice might not work accurately for the other slices.

2.3 – Histogram Matching Technique

Our approach to solve the problem outlined above was to select one slice as a reference and find the threshold values for segmenting it properly (compared to manual segmentation). Then for segmenting any other slice, first, using the "histogram matching technique" (explained below) we change that slice's histogram such that it is as close as possible to the histogram of the reference

image. Then using the same threshold levels that were used for segmenting the reference image, we improve the desired slice's contrast and conduct the segmentation.

Histogram equalization [16] achieves enhancement by spreading the gray levels of the input image over a wider range of the intensity scale. On the other hand, in histogram matching [23], we are able to specify the shape of the histogram that we wish the processed image to have. In what follows, we use only histogram matching.

Fig 2.7(a) and (b) respectively show a section of a flyash particle and the result of segmentation when the threshold values are properly selected for this slice. In Fig 2.7(c), a different slice from the same particle used in Fig 2.7(a) is given. Fig 2.7(d) shows the result of segmentation when the threshold values, selected for segmenting the slice in Fig 2.7(a), were used to segment this slice. As explained above, the threshold values must be selected specifically for the slice being segmented. The slice in Fig 2.7(a) was then used as the reference image, and its histogram was used as a reference for conducting histogram matching on the slice shown in Fig 2.7(c). The result was then segmented using the same threshold values, and the segmentation result is shown in Fig. 2.7(e). Accordingly, by using histogram matching, we are able to segment every slice using the threshold values selected for the reference slice.
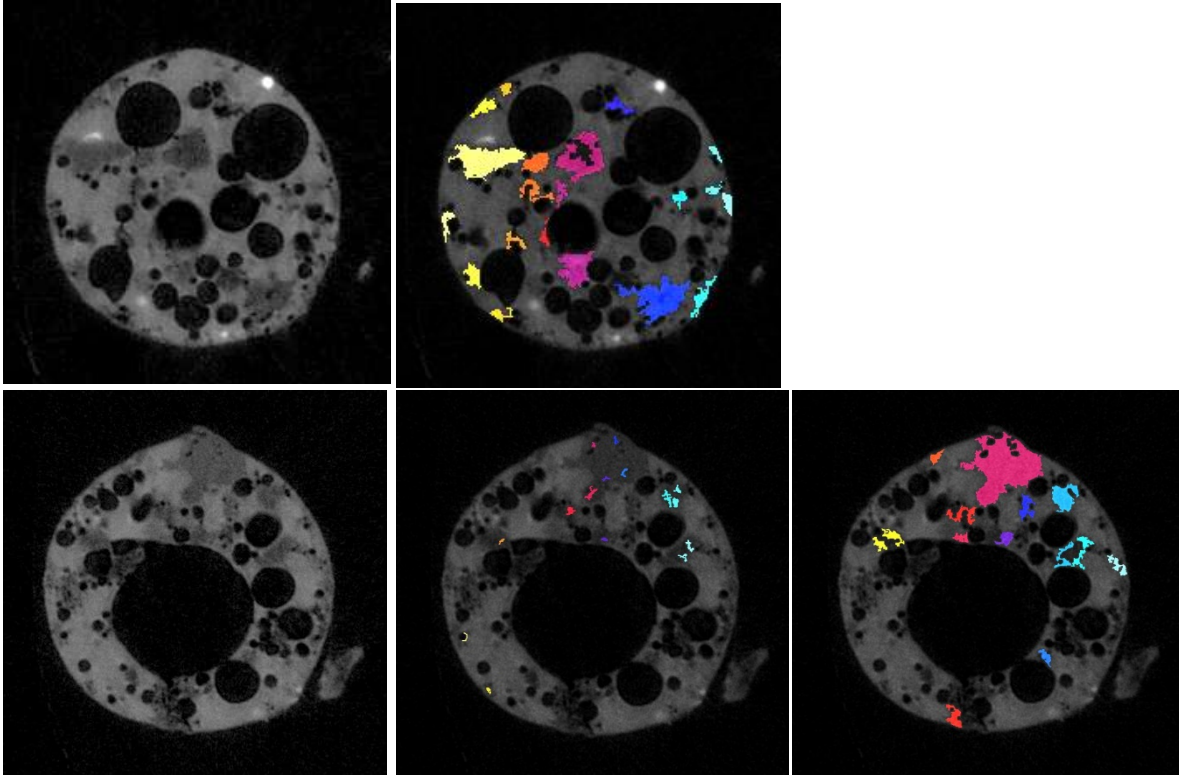
Figure 2.7 – Effect of histogram matching on segmentation result;
(a) Reference slice; (b) Segmentation with proper threshold values defined manually;
(c) A sample slice; (d) Segmentation of the sample slice without histogram matching
(same threshold values); (e) Segmentation of the sample slice after histogram
matching (same threshold values)

a b
c d e

In Fig 2.8(a) the gray scale histogram of the two slices shown in Fig 2.7(a) and (c) are plotted in

red and blue, respectively. We then used the slice in Fig 2.7(a) as the reference, and using

histogram matching, we changed the histogram for the slice in Fig 2.7(c). The new gray scale

matched histogram is plotted in Fig 2.8(a) in green. The CDF (cumulative distribution function)

of the curves in Fig 2.8(a) are plotted in Fig 2.8(b). As can be seen in this figure after histogram

matching, the CDF of the image matches the CDF of the CDF of the target image (reference

image).

Blue – Histogram of Fig 2.3(c)

Red – Histogram of Fig 2.3(a)

Green - Histogram of Fig 2.3(c) after histogram matching
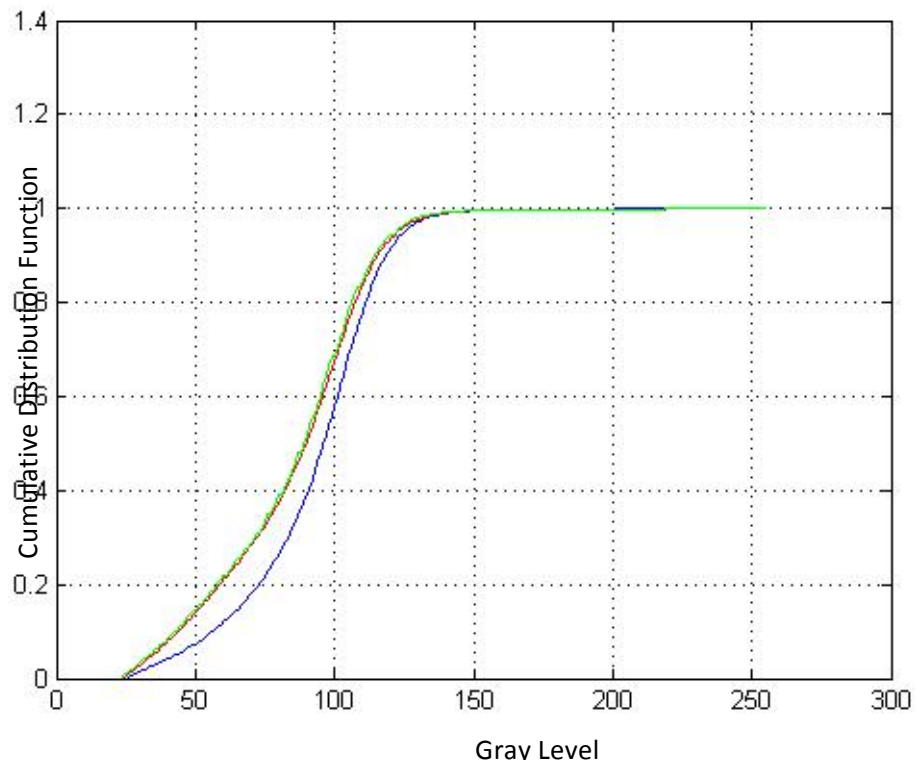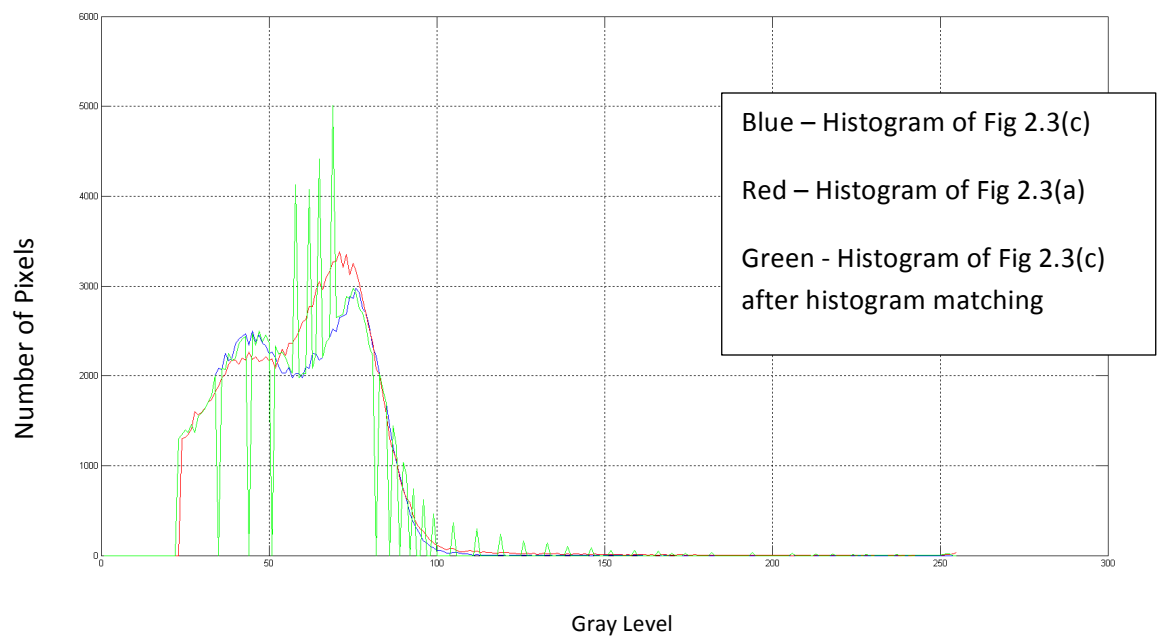
Figure 2.8 – Histogram equalization result

2.4 - Histogram Matching Using Artificial Histogram

Fig 2.9(a) shows an image, of the Mars moon, Phobos and Fig 2.9(b) shows its histogram [23]. The image is dominated by large, dark areas, resulting in a histogram characterized by a large concentration of pixels in the dark end of the gray scale (pixel values near zero).
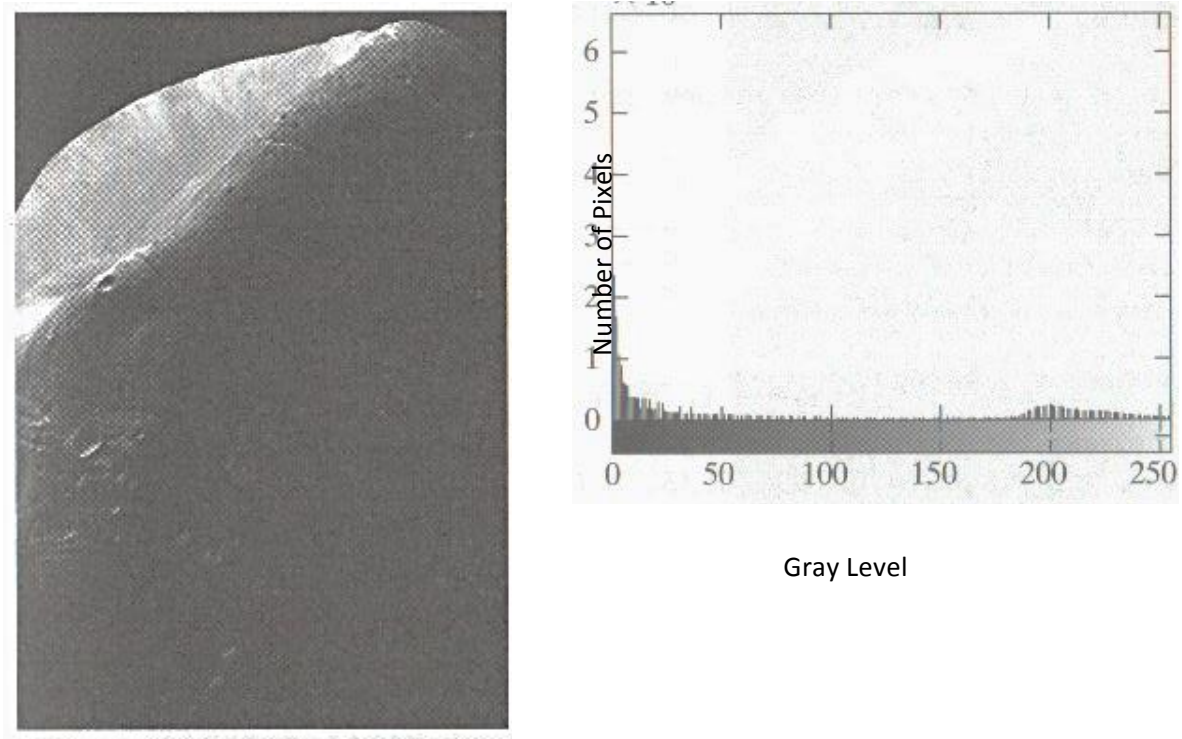
   (a) Image of the Mars moon Phobos   (b) Gray Scale Histogram

Figure 2.9 [23]

Using histogram matching, with the desired histogram having a smaller concentration of components in the low end of the gray scale, but maintaining the general shape of the histogram of the original image, more details in this image can be seen. Figure 2.10 shows a plot of a function that somewhat preserves the general shape of the original histogram, but has a smoother transition of levels in the dark region of the intensity scale. An image with the specified histogram was then generated shown in Fig 2.11(a); the result of the histogram of this new image

is shown in Fig 2.11(b). The most distinguishing feature of this histogram is how its low end has been moved closer to a lighter region of the gray scale.
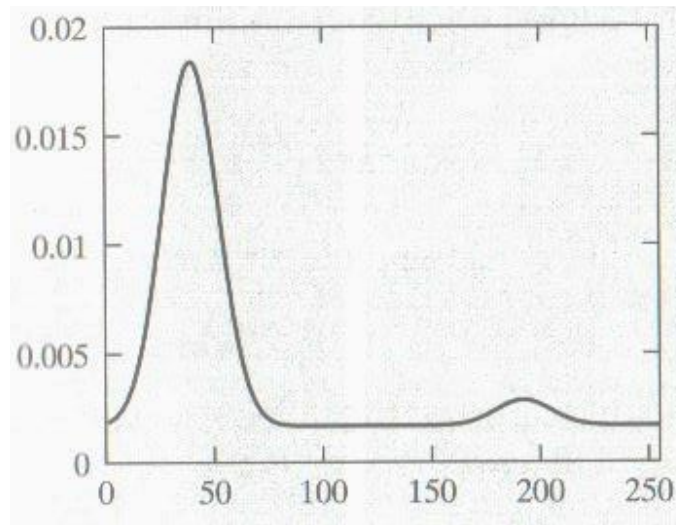
Figure 2.10 – Specified Histogram [23]
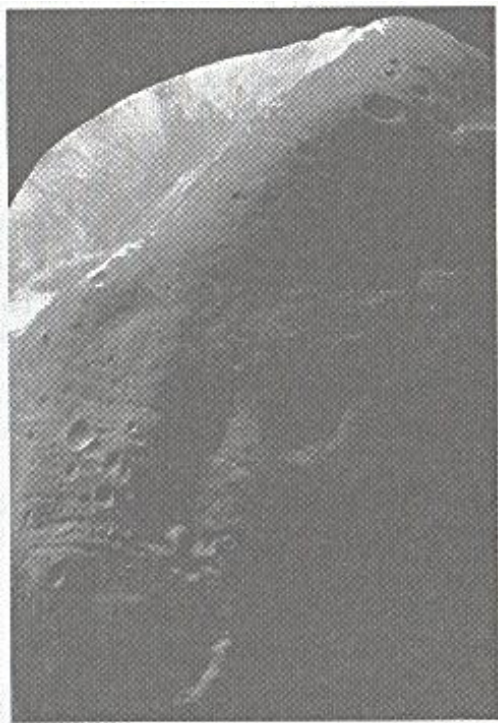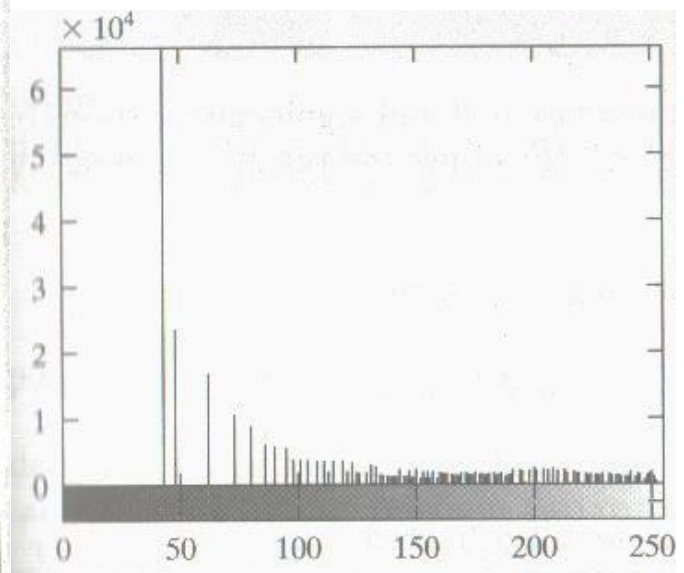
(a)   (b)
Figure 2.11 – (a) Result of Enhancement by Histogram Matching; (b) Histogram of Figure(a) [23]

In the problem of segmenting different phases of material in cross sections of flyash particles, as discussed before and presented in Fig 2.4 there are two major areas of interest in the material. So if we select a desired histogram that is composed of two Gaussian functions, the same size as the red curves shown in Fig 2.4(c), but further apart, which makes the different phases more distinct in gray value, by matching the histogram of all the slices to this desired histogram, we can segment different phases more easily.

We note from Fig 2.4 that the histogram is basically bimodal with one large mode containing the major phase of the particle and another smaller mode very close to the major one, containing the phase of material with slightly darker gray values. These types of histograms can be modeled by using multimodal Gaussian functions. Fig 2.12 shows a plot of a function that preserves the bimodality of the histogram in Fig 2.4(c), but further separates the red curve peaks.
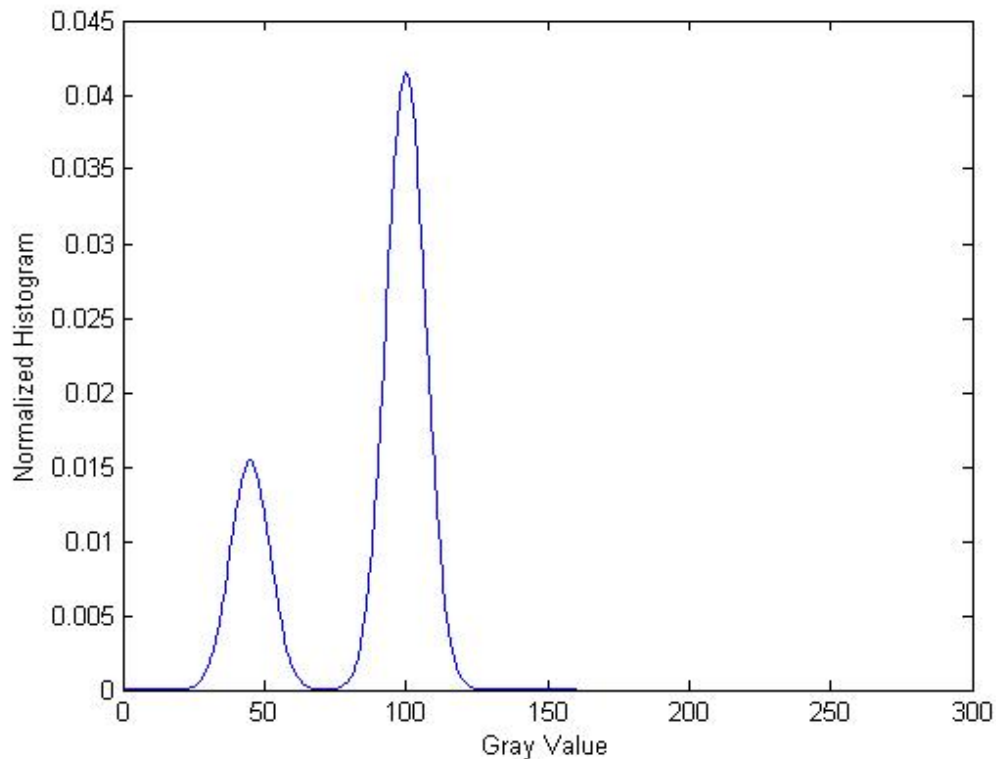
Figure 2.12 – Desired Artificial Histogram

The image shown in Fig 2.4(a) was then changed using the histogram matching technique explained in Section 2.3, such that its histogram matches the desired artificial histogram. The result is presented in Fig 2.13(a), with its histogram shown in Fig 2.13(b).

Since the peaks in Fig 2.13(b) are very distinct and separated, there is no need for contrast stretching, and segmentation can be done by setting a simple threshold which can be easily defined by a point of separation between the two peaks in the matched histogram.

(a)   (b)
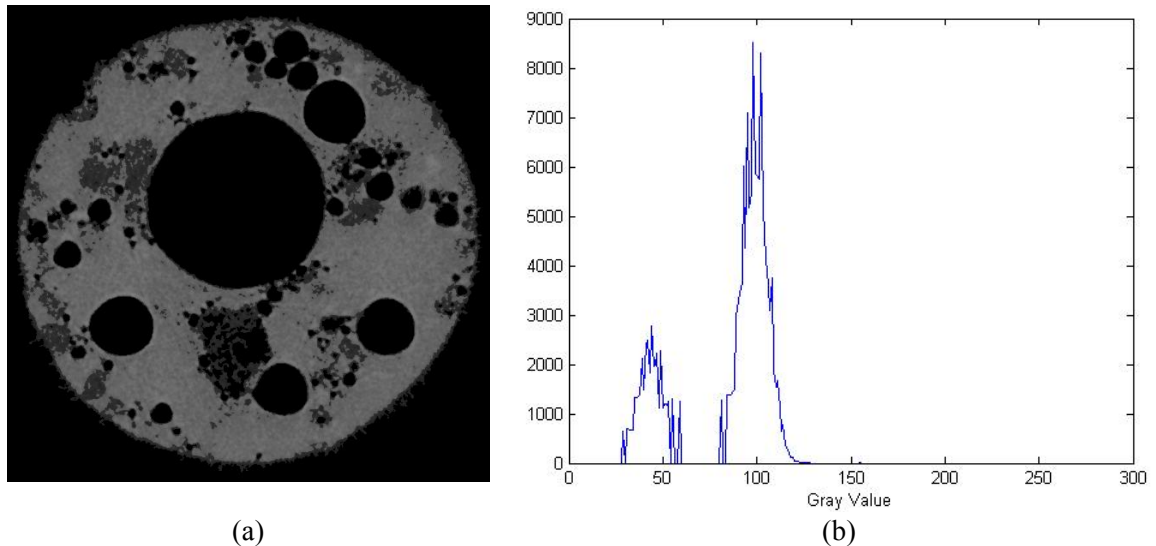
Figure 2.13 - (a) Result of Enhancement using Histogram Matching; (b) Histogram of (a)

2.5 - Inadequacies of Contrast Stretching and Histogram Matching

The two methods explained in this chapter (1- histogram matching with contrast stretching and 2- histogram matching using an artificial histogram) are capable of segmenting different phases of material in the body of the particle. Figure 2.14 (a) and (b) show the SEM (Scanning Electron Microscope) and the corresponding µCT slice results for a flyash particle slice. By comparing the µCT images with the SEM results, we notice that there are some visual differences between different phases. SEM results show that these differences are due to the different compositions of

the material, but detecting them by looking only at the gray scale µCT images is very difficult, even for a skillful human observer.
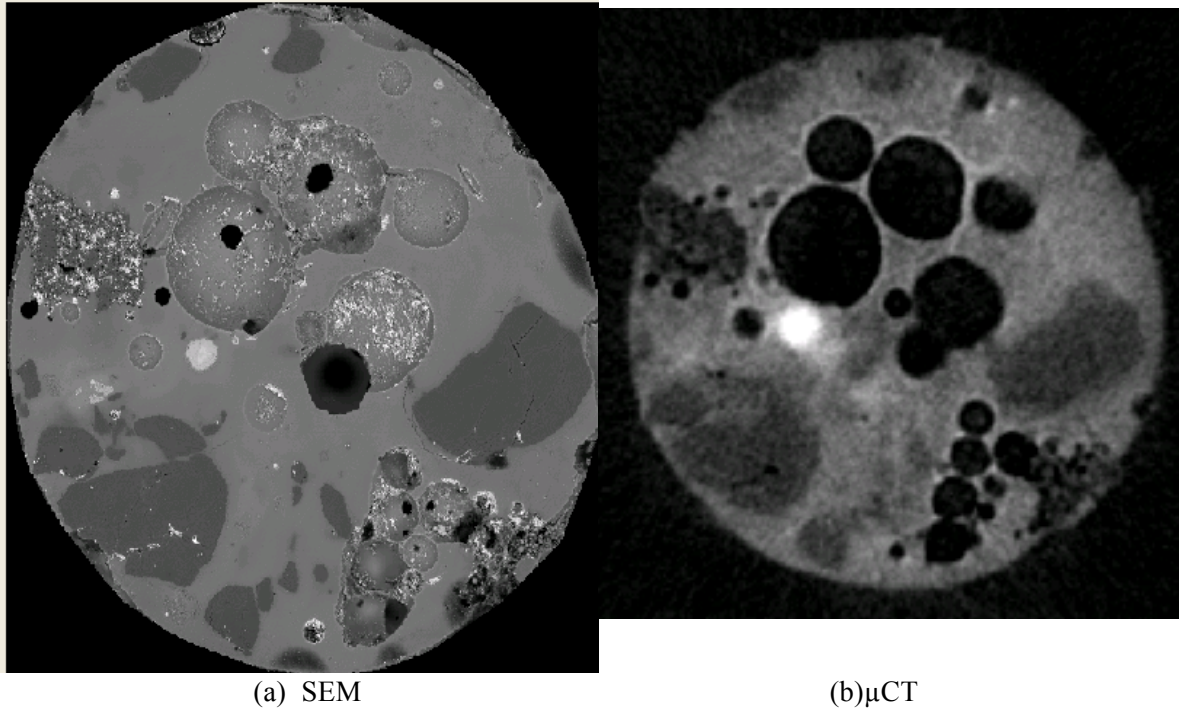
(a) SEM   (b)µCT
Figure 2.14 – SEM of a fly ash particle slice with the µCT of the corresponding slice

Based on our studies of the gray scale values of the pixels in these regions, it does not appear possible to accurately cluster them based only on gray scale values alone. However, after segmenting these regions from the rest of the particle, by studying the texture and pattern of the changes in pixel values in these regions, we can extract more information from the µCT images and associate them to specific materials. A proposed method for pattern recognition using Gabor filters enables us to segment the phases more accurately. The details of this method and the improvements in the segmentation of flyash particles are explained in the next chapter.

CHAPTER III

GABOR FILTERING

3.1 – Introduction to the Gabor Filter

Gabor filters are bandpass filters that are used in image processing for feature extraction, texture analysis [17], and stereo disparity estimation [18]. J. G. Daugman discovered that simple cells in the visual cortex of mammalian brains can be modeled by Gabor functions [19]. Thus, image analysis by Gabor functions is similar to perception in the human visual system.

The impulse response of these filters is created by multiplying a Gaussian function with a complex oscillation. Because of the multiplication-convolution property (Convolution Theorem), the Fourier transform of a Gabor filter's impulse response is the convolution of the Fourier transform of the harmonic function and the Fourier transform of the Gaussian function. The filter has a real and an imaginary component representing orthogonal directions and is represented in the following equations, where x, y are rectangular coordinates of a point on an image and other parameters are defined below.

complex:

$$g(x, y; \lambda, \theta, \psi, \sigma, \gamma) =$$

$$exp\left(-\frac{x'^2 + \gamma^2 y'^2}{2\sigma^2}\right) exp\left(i\left(2\pi\frac{x'}{\lambda} + \psi\right)\right) \tag{3.1}$$

real:
$$g(x, y; \lambda, \theta, \psi, \sigma, \gamma) = exp\left(-\frac{x'^2 + \gamma^2 y'^2}{2\sigma^2}\right) cos\left(2\pi\frac{x'}{\lambda} + \psi\right) \tag{3.2}$$

imaginary:
$$g(x, y; \lambda, \theta, \psi, \sigma, \gamma) = exp\left(-\frac{x'^2 + \gamma^2 y'^2}{2\sigma^2}\right) sin\left(2\pi\frac{x'}{\lambda} + \psi\right) \tag{3.3}$$

where

$$x' = xcos\theta + ysin\theta \tag{3.4}$$

$$y' = -xsin\theta + ycos\theta \tag{3.5}$$

In these equations λ represents the wavelength of the oscillatory factor, θ represents the orientation of the normal to the parallel stripes of the Gabor function, ψ is the phase offset, σ is the standard deviation of the Gaussian function and γ is the spatial aspect ratio, which specifies the elipticity of the base of the Gabor function.

Examples of Gabor filters with different frequencies and orientations are represented in Figure 3.1.
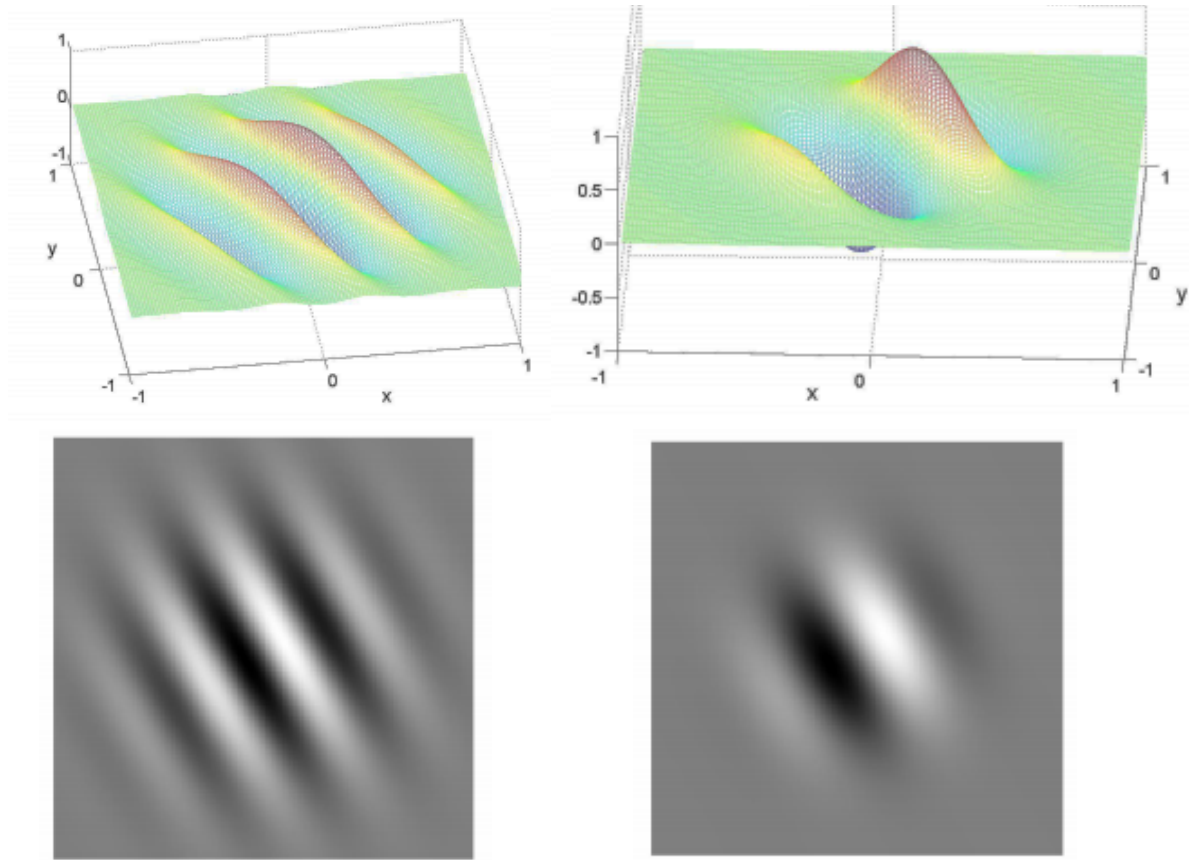
Figure 3.1 – Examples of Gabor Filters with different frequencies and orientations. First row shows their 3D plots, and the second row shows the intensity plots of their amplitude in the image plane.

3.2 – Circular Gabor Filter

Multichannel Gabor functions have been recognized as very useful tools in computer vision and image processing, especially for texture analysis. The increasing research on Gabor analysis is motivated by biological findings. Numerous papers have been published on Gabor analysis since Gabor proposed the 1-D Gabor function [23, 24, 25]. Researchers have agreed that Gabor-like linear spatial filtering plays a crucial role in the function of mammalian biological vision systems, particularly with regard to textures [19]. In this work, based on the texture of the particles we are to segment, we use invariant texture segmentation based on multichannel analysis. The method is based on using a traditional Gabor filter (TGF), modified into a circular symmetric version. Gabor filters are very useful in the detection of texture direction, but in rotation invariant texture

analysis, the orientation of texture becomes less important. In TGF, the sinusoidal waves propagate in one direction. For sinusoidal wave propagation in all directions (2D), we may use circular Gabor filters (CGF), which are circularly symmetric. The circular Gabor filter g(x,y;F,ψ,σ,γ) is described by:

$$g(x, y; F, \psi, \sigma, \gamma) =$$

$$exp\left(-\frac{x^2 + \gamma^2 y^2}{2\sigma^2}\right) cos\left(2\pi F\sqrt{x^2 + y^2} + \psi\right) \tag{3.6}$$

In this equation F represents the frequency of the oscillatory factor, ψ is the phase shift, σ is the standard deviation of the Gaussian function and γ is the spatial aspect ratio, which allows the CGF to become an elliptical Gabor function by specifying the elipticity of the base of the circular Gabor function (γ=1.0 for CGFs).

An example of a circular Gabor filter is represented in Figure 3.2. The image on the right is the 2D representation of the filter shown in the image on the left. Brighter colors represent higher values in the filter.
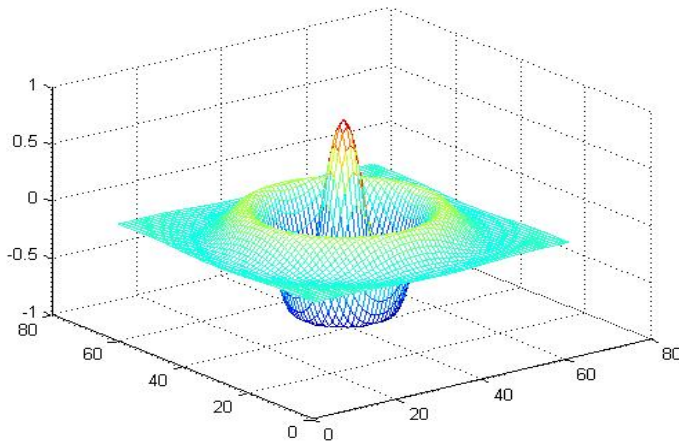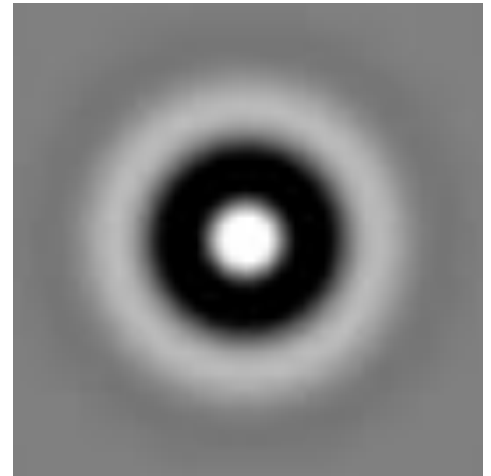
3D plot   Intensity Plot of the Amplitude
Figure 3.2 – Example of circular Gabor filter

3.3 - The Proposed Technique

3.3.1 – Problem Description

Fig 3.3(a) shows a sample flyash cross section, and in Fig 3.3(b) the same cross section is presented, but different materials are represented with different colors. This segmentation is based on SEM data available for this cross section [32]. The SEM procedure employs a destructive test and is only available for one cross section of a particle. Comparing Fig 3.3 (a) and (b), we notice three major phase in the cross section, which are marked with circles in Fig 3.3(a). Based on the color differences of these regions in Fig 3.3(b), we know that the region marked with a blue circle in Fig 3.3(a) contains a different material than the regions marked with red circles. Comparing the patterns of these regions in the gray scale image for these two materials, it is noticeable that the region marked with the blue circle is more "porous" than the region marked with red circles.

(a)   (b)
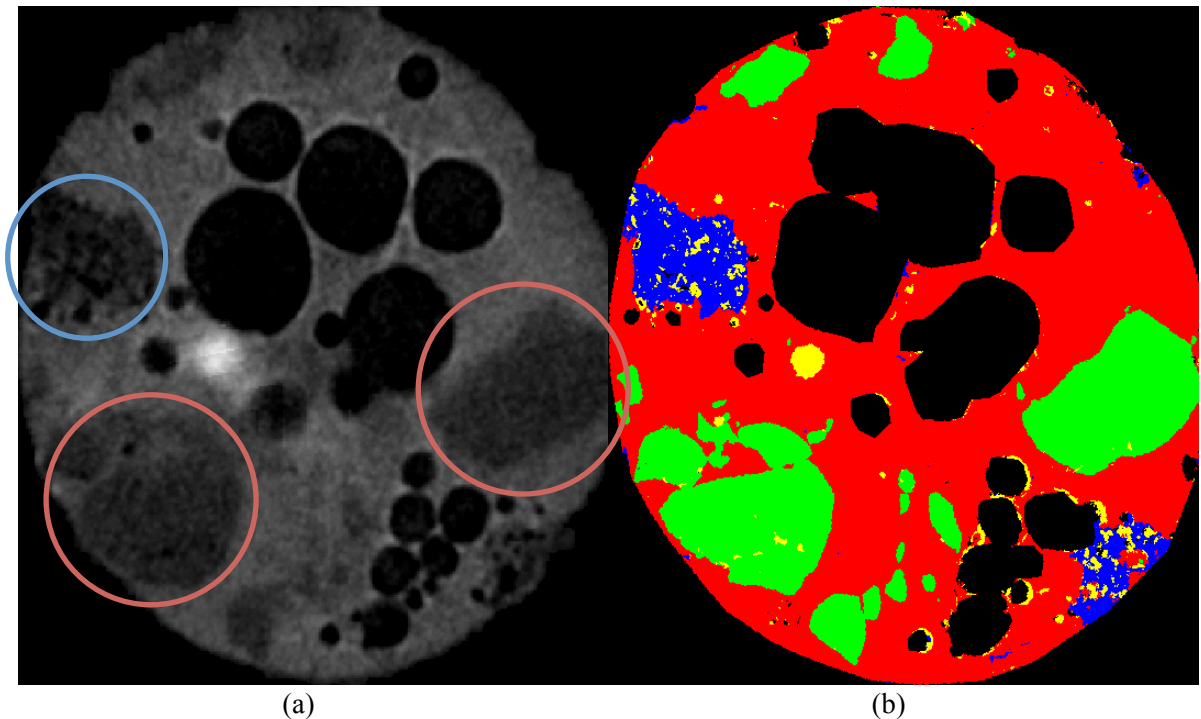
Figure 3.3 – Data from one cross section of a flyash particle: (a) μCT result –Different materials are marked with different color circles; (b) material segmentation based on SEM data – Different materials are marked with different colors. [32]

In order to segment the region with more porosity in Fig 3.3(a), a circular Gabor filter with band width (bw) = 1, phase shift (psi) = $\pi/2$ and frequency (F) = 0.2 was created by trial and error and then convolved with the gray scale image shown in Fig 3.3 (a). The criteria for selecting the parameters of the filter are explained in the next section. The result of this convolution is presented in Fig 3.4, in which the same regions marked in Fig 3.3(a) are marked for better comparison. We note that only the regions with porous characteristics and the edges of the holes in the cross section are passed by this filter. Using some post processing analysis, explained in the next chapter, the edges of the holes can be removed from this image. Accordingly, we propose using circular Gabor filters to cluster these phases.
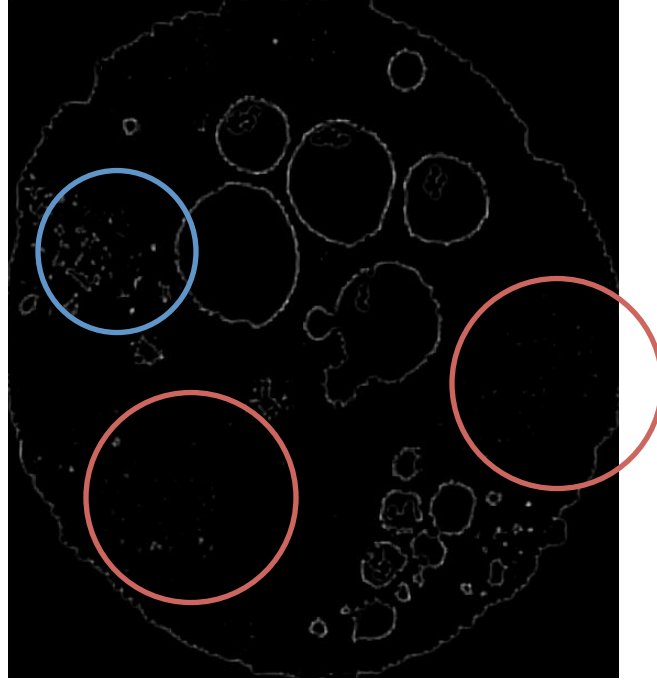
Figure 3.4 – Result of convolving the gray scale image in Fig 3.3(a) with a circular Gabor filter (band width (bw) = 1, phase shift (psi) = $\pi/2$ and frequency (F) = 0.2)

3.3.2 – Gabor Filter Parameter Selection

Considerable research has been done on the subject of defining Gabor filter parameters [23, 25, 26]. Most of the proposed methods involve reducing the degrees of freedom (number of parameters) in Gabor filters based on neurophysiological findings [26]. One important finding is that the spatial frequency bandwidth of the response of human visual cortical cells ranges from 0.5 to 2.5 octaves.

The parameters σ and the frequency F in the CGF satisfy the following relationship with the bandwidth B of the Gabor filter [27]:

$$F\sigma = \lambda\frac{(2^B+1)}{(2^B-1)} \tag{3.7}$$

where

$$\lambda = \frac{\sqrt{2\ln 2}}{2\pi} \tag{3.8}$$

$$B = \log_2\frac{f_1}{f_2} \tag{3.9}$$

As illustrated in Fig 3.5, f_0(center frequency) is the frequency at which the amplitude is maximum. In Gabor filter design, f_1and f_2 which are, respectively, smaller and larger thanf_0, are the frequencies corresponding to the half peak magnitude of the circular Gabor Fourier response. The bandwidth, shown in Fig 3.5, is the frequency range between f_1 andf_2, and is usually expressed in octaves. A frequency range is said to be an octave in width when the upper band frequency f_2 is twice the lower band frequencyf_1. In this project by trial and error we set the value of the bandwidth of the Gabor filter to 1 octave.
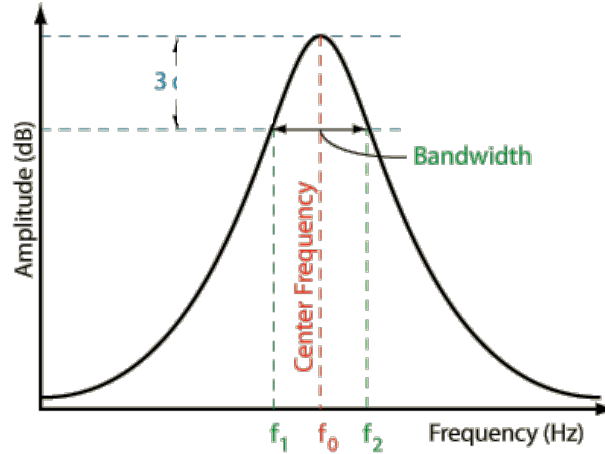
Figure 3.5 - Bandpass Filter Parameters

Our experimental results on images of the cross sections of flyash particles show that, when the
frequency (F) and phase shift of the Gabor filter is selected properly, the region with porosity in
the gray scale image shows the highest response to the circular Gabor filter, compared with non-
porous regions. When the frequency is too high, the filter amplifies every single pixel in the
image. When the frequency is too low, details from the pattern are filtered out.

3.3.2.1 – Effects of Frequency and Phase Shift in the Shape of CGF

As explained before three major factors that define the shape of a circular Gabor filter are band
width, phase shift and frequency. Based on the proposals found in the literature and our trial and
error tests on flyash particle cross section images, we set the band width at 1 octave. Phase shift
and frequency are the two independent factors that can modify the shape of the filter. But in order
to design a certain shape CGF, there are multiple combinations of phase shift and frequency that
can be used to design the filter.

When a circular Gabor filter is plotted in a gray scale image, the peaks (with higher values) are
presented with bright gray values and the valleys (lower values) are presented with dark gray
values. So the representation of a circular Gabor filter in a gray scale image is a bright "donut

46

ring", which represents the size of the circular shaped pattern that it can magnify when convolved with an image.

Fig 3.6 shows nine different CGFs, all of which have phase shift set at $\pi/2$, with the frequency increasing gradually ranging from 0.1 cycles/pixel in the top left image to 0.26 cycles/pixel in the bottom right image. Note than in these plots, as the frequency increases (with a constant phase shift), the filter becomes smaller. In Fig 3.7 nine different CGFs are represented. In all of these filters the frequency was kept constant at 0.1, but the phase shift increased gradually from 1.57 rad ($\pi/2$) in the top left image to 4.36 rad in the bottom right image. We note that as the phase shift increases, the CGF becomes smaller. Comparing Fig 3.6 and 3.7, we observe that different sizes of CGF can be designed by different combinations of frequency and phase shift.
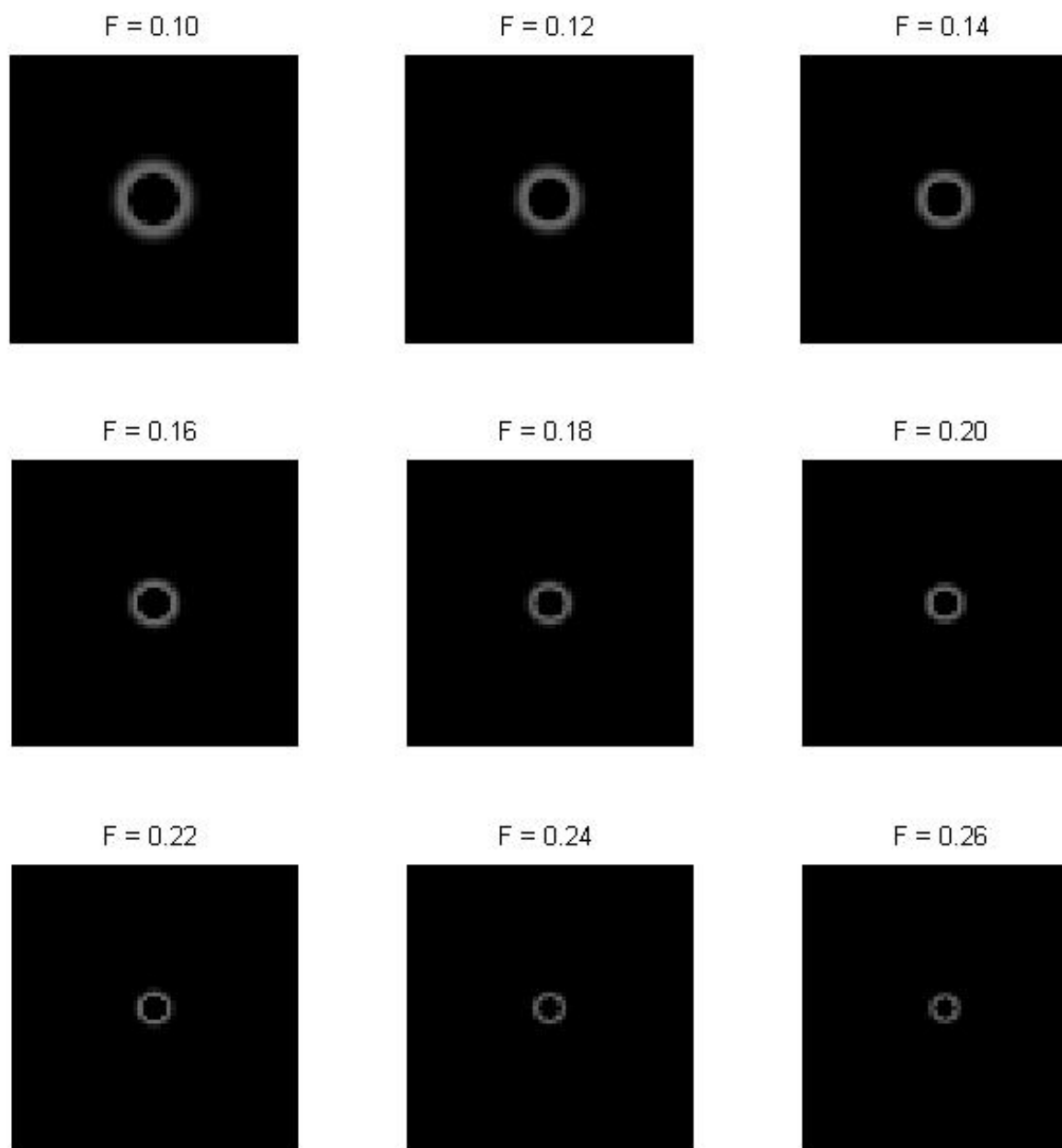
Figure 3.6 – CGF designed with a constant phase shift (π/2) but different frequencies (cycles/pixel)
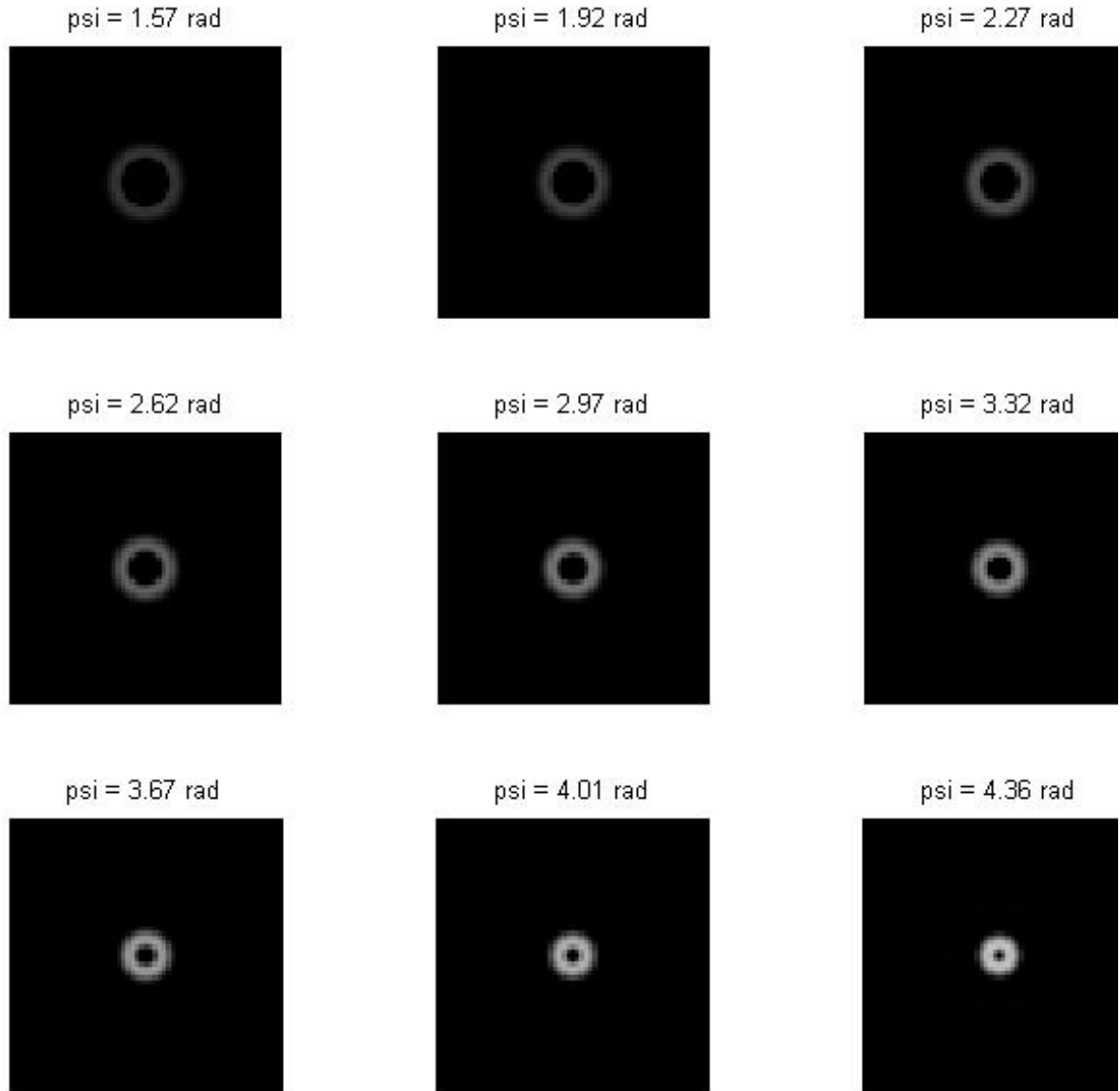
Figure 3.7 – CGF designed with a constant frequency (0.1 cycles/pixel) but different phase shifts

Figure 3.8 shows a selected region from a cross section of a flyash particle. This specific region was then convolved with circular Gabor filters with different frequencies, and the responses are shown in Figure 3.9. As explained before, if the frequency is too high or too low, the response of the pattern to the filter is not very meaningful. So in this example, the frequencies were selected such that they produce meaningful responses to the Gabor filter, namely responses in which the filter does not overly magnify everything or filter out everything. The goodness of a filter is based

on the similarity of the convolved image with the original image, as determined by the manual observation. In other words, a good convolution should appear like an amplified version of the original gray scale image, magnifying some characteristics of interest in the image, which in our case is porosity. This means that the filter preserves the size of porosity in the pattern and amplifies the heights and valleys in the porosity pattern.
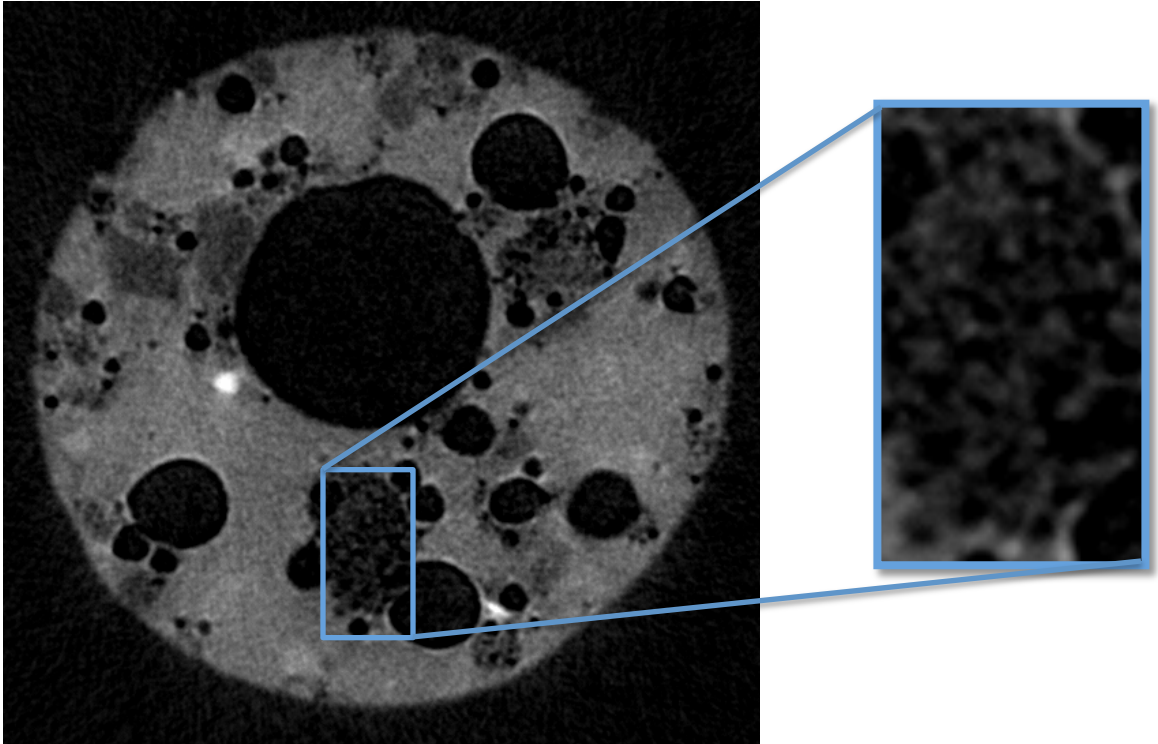
Figure 3.8 – A porous region selected from a cross section of a flyash particle to be convolved with circular Gabor filters with different frequencies

| F = 0.06 | F = 0.13 | F = 0.16 | F = 0.21 |
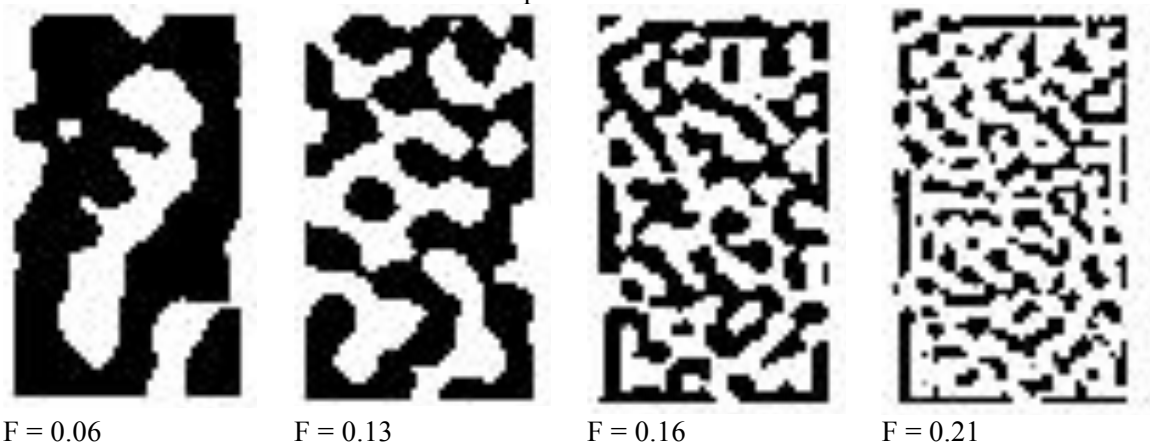
Figure 3.9 – response of the selected region in Figure 3.8 to circular Gabor filters with band width (bw) = 1, phase shift (psi) = $\pi/2$ and various Frequencies (F) (cycles/pixel)

By manually comparing the results in Figure 3.9 with the region selected in Figure 3.8, we determine that the CGF with F=0.13 (cycles/pixel) seems to produce the best response among the four.

In order to quantify the goodness of the filter, different statistical measures such as entropy, correlation and homogeneity were calculated for the results of convolving the selected region with a circular Gabor filter. Among these factors, correlation showed the most meaningful relationship with the goodness of convolution, explained below.

3.3.2.1 - Using Entropy for quantizing the goodness of convolution

The region shown in Figure 3.8 was convolved with circular Gabor filters with various frequencies. For this specific region, based on visual observations, the frequency of the circular Gabor filter with the most meaningful result was F = 0.13 (cycles/pixel).

Entropy is a statistical measure of uncertainty in a random variable [28]. In this case it can be used to characterize the texture of the input image. Entropy is defined as [28]:

$$E = -\sum_i P_i \log_2 P_i \qquad (3.10)$$

Where Pi is the probability that the difference between two adjacent pixels is equal to i.

The entropy of the result was then calculated and plotted versus the Gabor filter frequency, shown in Figure 3.10. In this figure, as the frequency increases, entropy exhibits two major peaks, and the frequency of the best response (based on the visual observations of the result) is at the first (leftmost) peak of this curve. Increases in entropy mean that convolution produces more details in the pattern of the selected region. Accordingly, the second peak at a higher frequency occurs where the CGF amplifies edges in the image. This trend (entropy graph with two major peaks,

51

with the best result lying in a close neighborhood of the major peak with lower frequency) applies

to other sample regions with porosity that we examined.
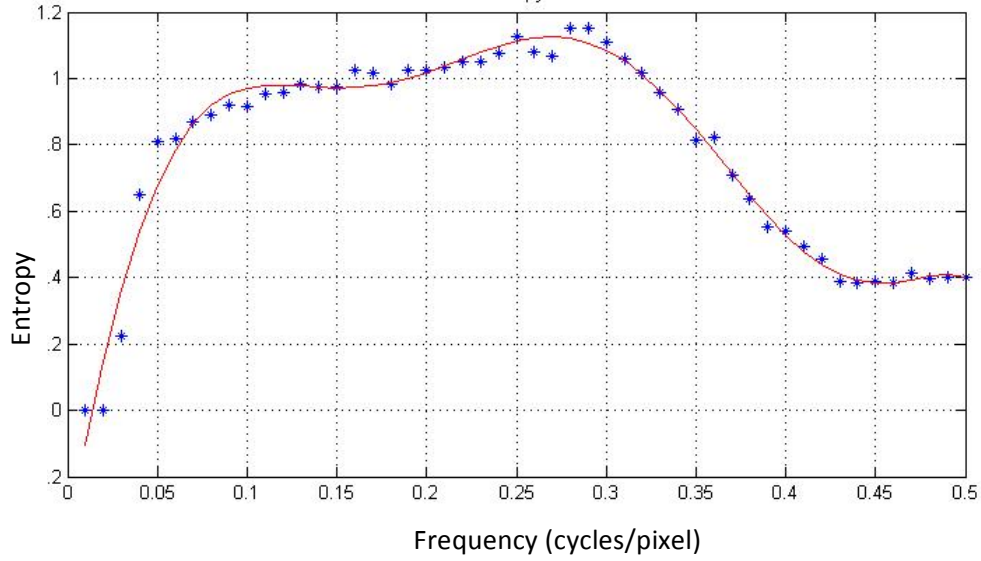
Figure 3.10 – Entropy of the convolution result versus the frequency of the circular Gabor filter

Entropy can be a measure for finding the proper frequency for the Gabor filter, but its accuracy

appears only good enough to find the neighborhood of the best frequency.

3.3.2.2 - Using Correlation for quantizing the goodness of convolution

As described before, a good convolution should look like an amplified version of the original

gray scale image, such that no information from the pattern is lost. Therefore one measure of

goodness of the filter is the amount of correlation between the result of the convolution with the

original image. Digital Image Correlation (DIC) is an optical method that employs image

registration techniques for measurements of changes in images [29,30]. Using Equation (3.11)

we can compute the correlation coefficient (r) between image matrices A and B, given by:.

$$r = \frac{\sum_m \sum_n (A_{mn} - \bar{A})(B_{mn} - \bar{B})}{\sqrt{(\sum_m \sum_n (A_{mn} - \bar{A})^2)(\sum_m \sum_n (B_{mn} - \bar{B})^2)}}$$

(3.11)

where $\overline{A}$ and $\overline{B}$ are the mean values of matrices A and B.

Following the same process as in the previous section, we calculated the amount of correlation between the result of the convolution and the original image for every frequency that was used in the CGF. From the visual inspection, the best result occurs at F=0.13 (cycles/pixel). The correlation value versus the frequency of the CGF is plotted in Figure 3.11. We note that the graph has a maximum at $F \approx 0.13$ (cycles/pixel).
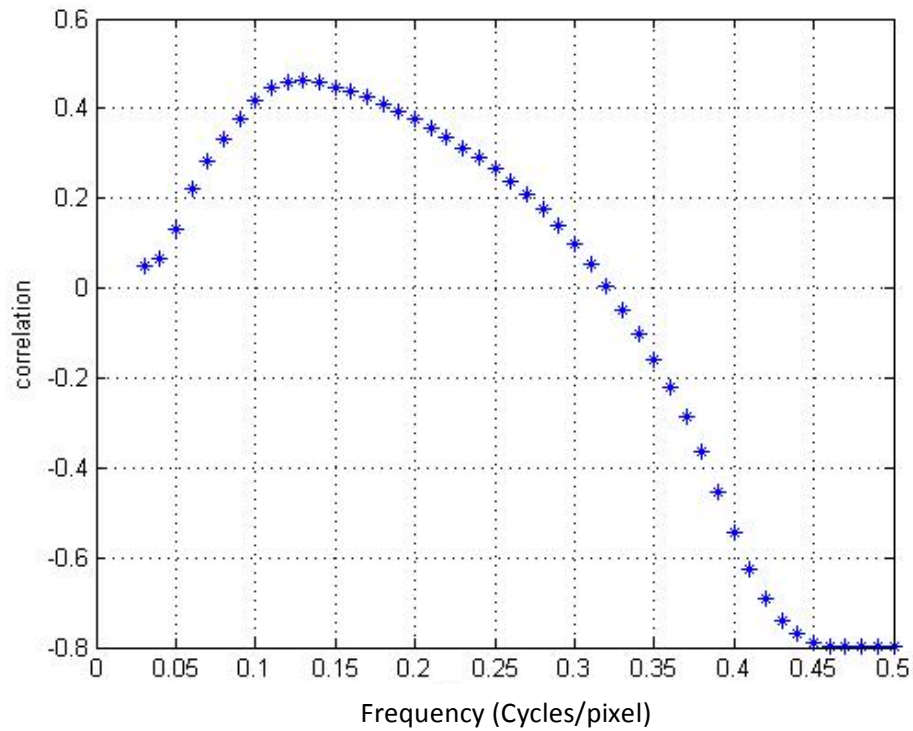
Figure 3.11 – Correlation between the convolution result and the original image versus the frequency of the circular Gabor filter

These results can be seen in Figure 3.12, where the result of convolution of the original image with a CGF with the frequency F=0.13 (cycles/pixel) is presented alongside the original image, which is a phase with porosity cut from a cross section of a flyash particle.
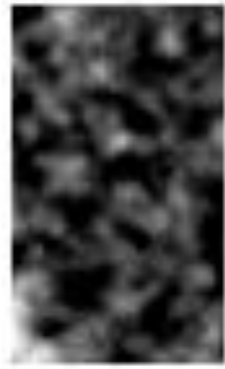
Original image   Convolution Result, F = 0.13 (cycles/pixel)

Figure 3.12 – Comparison of the original image and the result of convolution using the best frequency for Gabor filter

Accordingly, correlation can be used as a good measure to find the proper frequency for designing a CGF for detecting phases with porosity.

In the next chapter, post processing procedures, after applying the circular Gabor filter, are presented. Post processing is necessary because as can be seen in Figure 3.4, the CGF not only amplifies the pattern of interest, but it also magnifies some the noise in the gray scale image, as well as the edges and holes. Following this, all our techniques introduced for clustering different phases of material in flyash particle will be combined into one program to segment these phases simultaneously in every cross section.

CHAPTER IV

POST PROCESSING AND CLUSTERING

For each of several available flyash particles the µCT scan of 4 to 5 hundred cross sections and

SEM scan result of one cross section is available [32]. Since SEM is a destructive test and can be

used to define the exact material in the cross section from which it is taken from, we can use it as

our ground truth. Then by correlating the µCT scan result of the corresponding cross section gray

scale pattern, different phases can be determined. An example of this data (SEM scan of a cross

section of a fly ash particle and the µCT scan of the corresponding cross section) is presented in

Fig 3.3. Using correlation between these two images, we can define the boundaries of the phase

with porous texture in the gray scale µCT result. This region can then be used in the procedure

explained in Section 3.3.2 to find the proper frequency for designing the circular Gabor filter.

Using the procedure in Section 3.3.2 will help assure that the designed Gabor filter has

characteristics that highlight the pattern in the selected region. Since the selected region is a valid

representative of the desired phase (based on the data from the ground truth – SEM), this Gabor

filter can be applied to the µCT scan result of the remaining cross sections to determine the phase

with that specific pattern. This procedure is diagramed in Fig 4.1.

```
┌─────────────────┐     ┌─────────────────┐          ┌─────────────────┐
│      SEM        │     │      μCT        │          │      μCT        │
└────────┬────────┘     └────────┬────────┘          └────────┬────────┘
         │                       │                            │
         ▼                       ▼                            │
┌──────────────────────────────────────────┐                 │
│   Define boundaries of the material with  │                 │
│              porous pattern               │                 │
└─────────────────────┬────────────────────┘                 │
                      │                                       ▼
                      ▼                             ┌──────────────────┐
          ┌───────────────────────────────┐        │   Filter with    │
          │  Design the proper Gabor filter├──────► │   the Gabor      │
          └───────────────────────────────┘        │    Filter        │
                                                    └────────┬─────────┘
                                                             │
                                                             ▼
                                          ┌───────────────────────────────────┐
                                          │  Segment different phases of material │
                                          └───────────────────────────────────┘
```
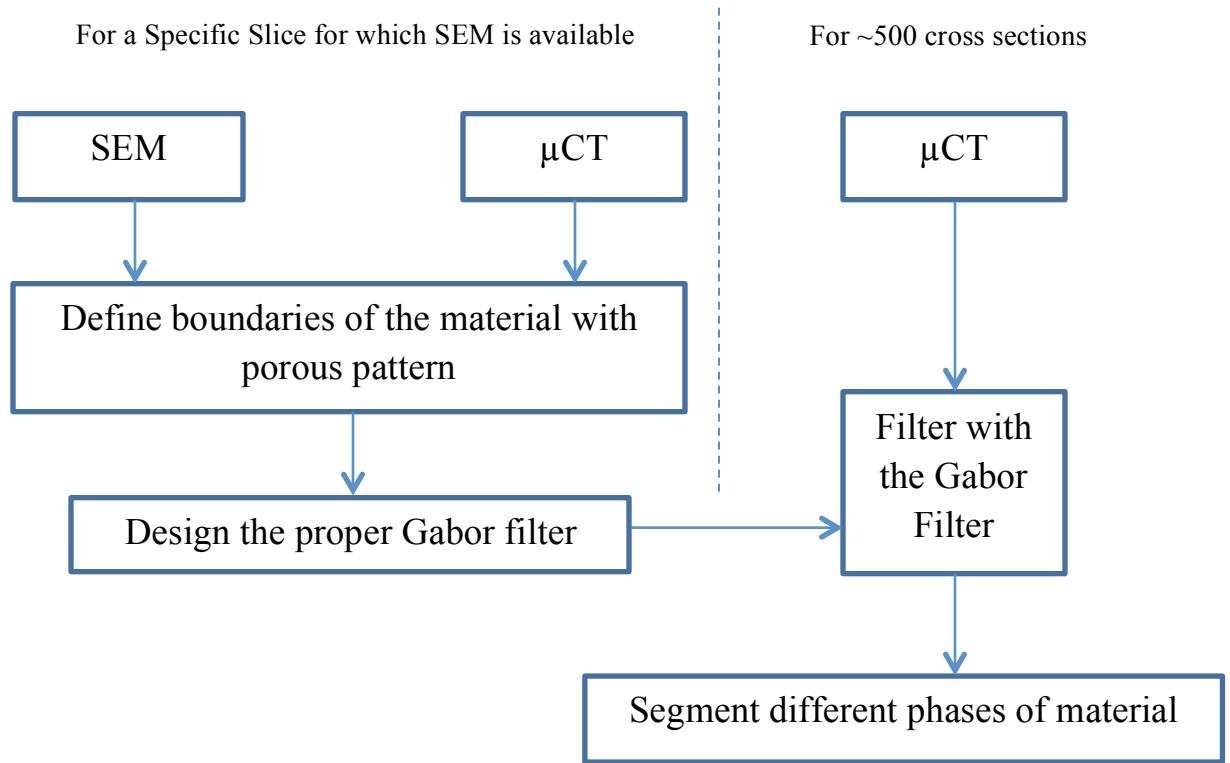
Figure 4.1 – Procedure for segmenting the phase with a porous gray scale pattern

Fig 4.2 shows the result of applying a properly sized Gabor filter on a gray scale cross section of a fly ash particle. As can be seen in this figure, the regions with the highest response to the Gabor filter are the edges (boundaries of the particle and the holes inside the cross section) and the porous phase regions. In order to accurately segment the phase using this response, the edges and noise should be removed.
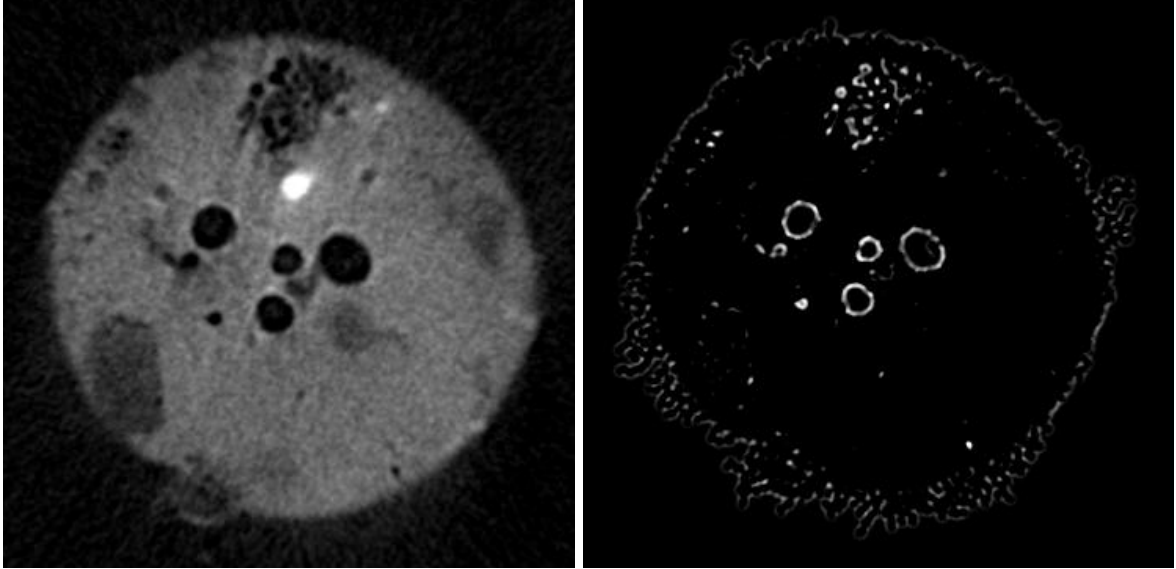
(a) Original Image   (b) Response to the Gabor filter

Figure 4.2 – Result of applying a properly sized Gabor filter to a sample µCT image

4.1 – Noise Removal Technique

After applying the CGF, different types of noise in the image respond to the filter and must be removed to be able to segment different phases of material.

One of the major regions that respond to the CGF is the boundaries of the cross section. In order to find the outer boundaries of the particle cross section, a harsh gray thresholding is applied to the original image, by which the edges of the outer circle can be easily extracted. Then the pixel values of points on the boundary and outside in the CGF output will be set to zero (removed from the image). This procedure is illustrated in Fig 4.3.
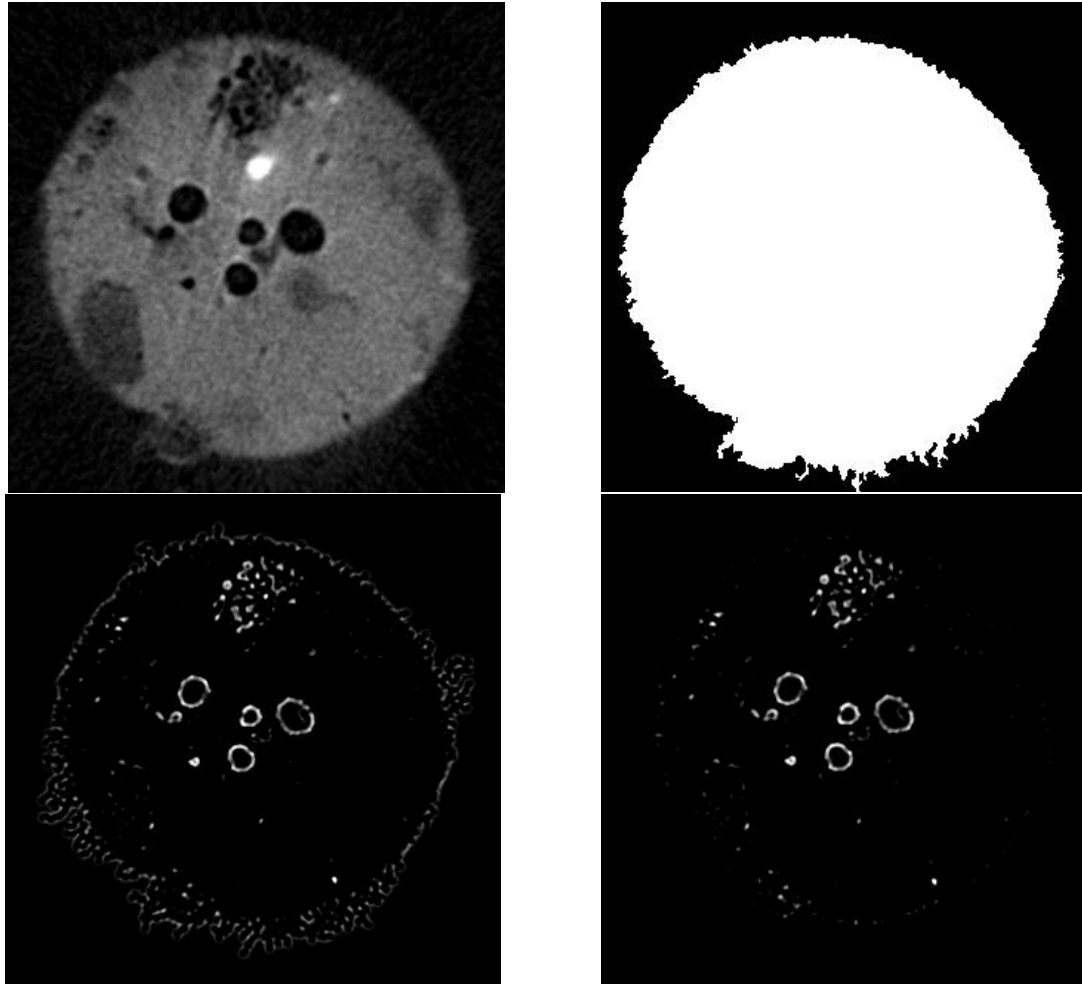
a b   Figure 4.3 – Procedure for removing boundaries - (a) Original Image; (b) Segmented
c d   Boundary; (c) Result of Applying the Gabor Filter to the Original Image; (d) Results
               from applying Gabor filter after removing the boundaries

Other major sources of noise are the edges and the gray values inside the holes in the cross

section of the gray scale images. We used MATLAB's built in function to find circles. This

function uses the Circular Hough Transform [39] for detecting the holes and defines the centers

and radiuses of the holes. The Hough Transform is a technique for detecting certain shapes in an

image; in our case this means finding circular shapes by convolving the image with different

shape filters. As the shape for which we search in the image becomes larger (in this case,

increasing radius), the filter size increases, which leads to long calculation times. In this project,

since the holes in the image are of various sizes, in order to have accurate detection, a wide range

of filter sizes must be tested to find a specific hole in the cross section. Since a circle is simple in shape, instead of searching over a wide range of radii, by trial and error we defined a specific range of radii for our figures and down-sized the image by scaling with different factors determined by trial and error, and applied the same filters to every scaled image to find all hole existing in the cross section. In other words, instead of using a large size filter to find the large holes, the image was compressed so that the holes became smaller and could be detected using small-sized filters. The pixels inside and on the edges of the circles were then removed from the output of the CGF. This procedure is illustrated in Fig 4.4.

After the two stages of noise removal described above, we note in Fig 4.4 (c) that noise is not completely removed from the image, and there are some scattered points in the image that show strong response to the Gabor filter. In the next section, the technique for segmenting the phase from the results in Fig 4.4(c) is explained.

(a)   (b)   (c)

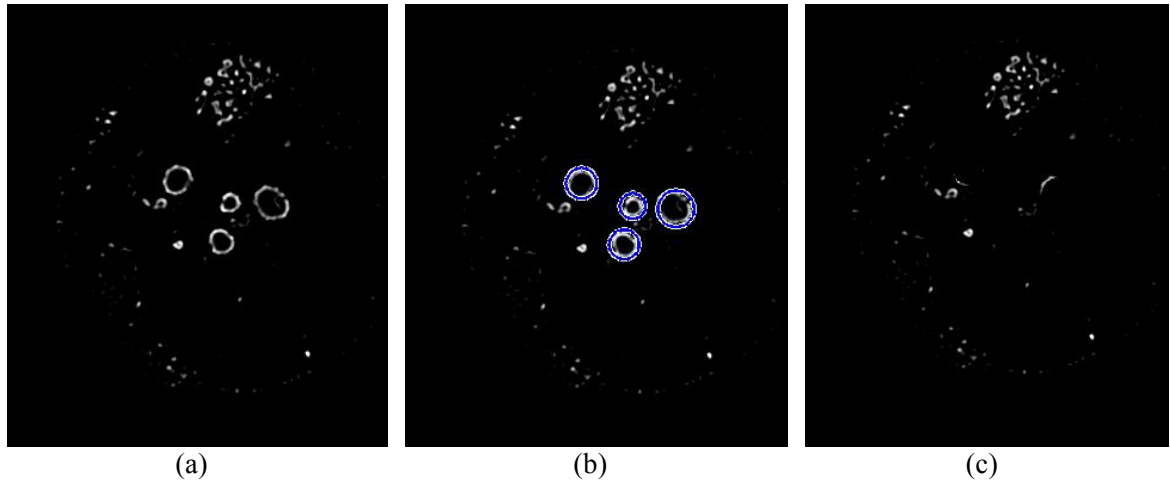Figure 4.4 – The procedure of removing holes from the cross section – (a) Cross section from Fig 4.3d; (b) detected holes in the image; (c) Result of Gabor filtering after removing the holes

4.2 – Using Entropy Segmentation

After removing the boundaries and the holes from the Gabor filtered result, what remain are the porous phase and some scattered noise, shown in Fig 4.4(c). In order to segment the phase,

different statistical measures such as entropy, correlation, homogeneity and contrast were

calculated for the pixels in this figure; we found that entropy had the most meaningful result for

segmenting the phase. Fig 4.5 shows entropy calculations (following (3.10)) on the cross section

of Fig 4.3. In Fig 4.5(b) brighter spots represent regions with higher entropy. These results are

plotted in a 3D format in Fig 4.5(c). By comparing this figure with the original image in Fig

4.3(a), we see that higher entropy regions are the regions with the porous material in the gray

scale cross section. In order to segment these regions in the original image, after linear

normalization of the entropy result in the range 0 to 1, we cluster every pixel with entropy higher

than a certain threshold as a different phase in the original image. The threshold in this project

was set at 0.5, based on testing different particles and considering different cross sections.
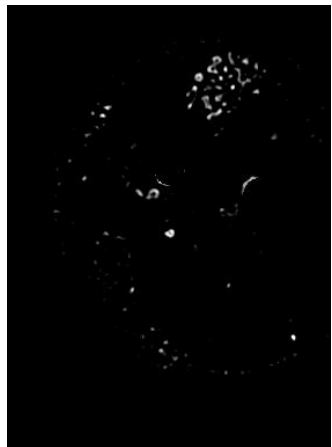
(a)
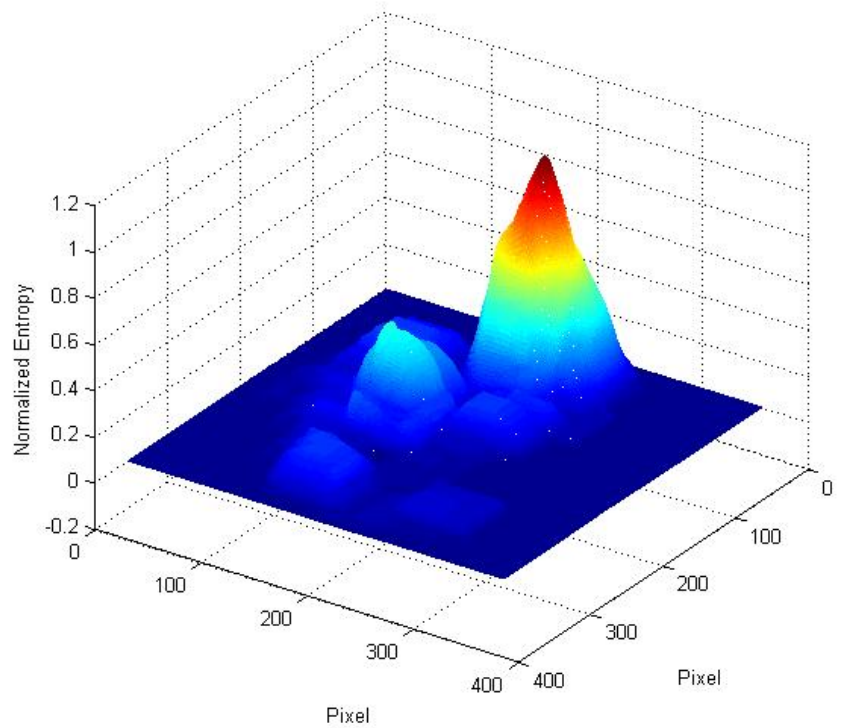
(b)   (c)

Figure 4.5 – Entropy Calculations for Segmenting Phases of Material: (a) Result of Convolution using Gabor Filter; (b) Entropy Calculation; (c) 3D Plot of Entropy

In the next chapter results of segmentation using this method on various cross sections of

different fly ash particles are presented. Then all the techniques designed herein for segmenting

different phases of material were combined, and the results are presented.

CHAPTER V

RESULTS AND CONCLUSIONS

Note: Please read the directions in the following paragraph very carefully before proceeding.

5.1 – Recap of all Techniques

In this report different techniques for segmenting different phases are examined. In this chapter

all these techniques are summarized, and the results of combining them and segmenting cross

sections of fly ash particles are presented. Note that due to the noisy nature of gray scale μCT

images, before applying any of these techniques every image is subjected to preprocessing steps

to decrease the noise.

5.1.1 – Segmenting Porous Phase

As explained earlier, in order to segment a porous phase, we employ a circular Gabor filter and

convolve it with the entire image. This CGF suppresses most of the pixel values, but amplifies

those belonging to the regions with porous texture. To properly design a CGF, a phase with

porous texture (training region) from a cross section image is selected and used for designing the

Gabor filter. For every fly ash particle, an SEM scan of a cross section and its corresponding μCT

scan result are available from our data [32]. This cross section is used as the ground truth, and the

training region is selected from this data. In Fig 5.1 (a) the SEM result of a fly ash particle is shown. Fig 5.2(b) shows the color coded result of the SEM test. In this image, different colors represent different materials, and Fig 5.1 (c) presents the µCT scan result of the same slice. The region, marked in Fig 5.1(b) contains a phase that by manual inspection contains a porous texture in the µCT scan result. This region is also marked in Fig 5.1(c), which can be used as our training region for designing the circular Gabor filter.

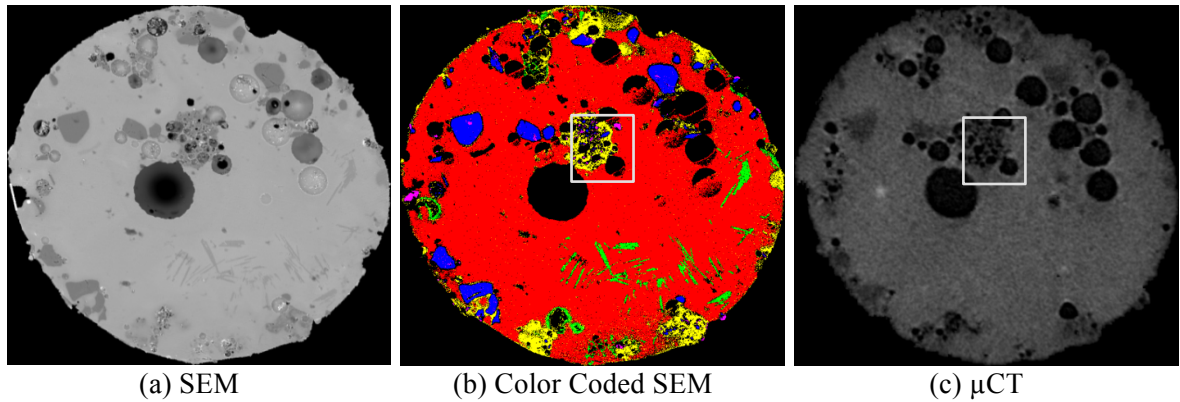<div align="center">(a) SEM   (b) Color Coded SEM   (c) µCT</div>

Figure 5.1 – The SEM and µCT scan result of a cross section available for a sample flyash particle.

After designing a suitable CGF, the filter was then applied to the entire image, and the result of segmentation is presented in Fig 5.2 alongside the color coded SEM data. As can be seen in this figure, other porous regions in blue are detected, as well as the region that was used for designing the CGF. The success in segmenting regions other than the one used for training illustrates that the designed CGF is capable of detecting other regions with similar porous texture.

Note that the µCT image used for segmentation is not taken from the exact section of the particle that the SEM scan is taken, because as stated before, these two scans are done through separate processes. In the SEM scan, sometimes the cut through the particle is not straight and does not represent the scan result of a plane section, such that the corresponding µCT scan result, used as the ground truth, is basically the scan from the closest section from which the SEM was taken.

Therefore there might be minor differences in the regions of different phases between the two images.

<center>(a)   (b)</center>
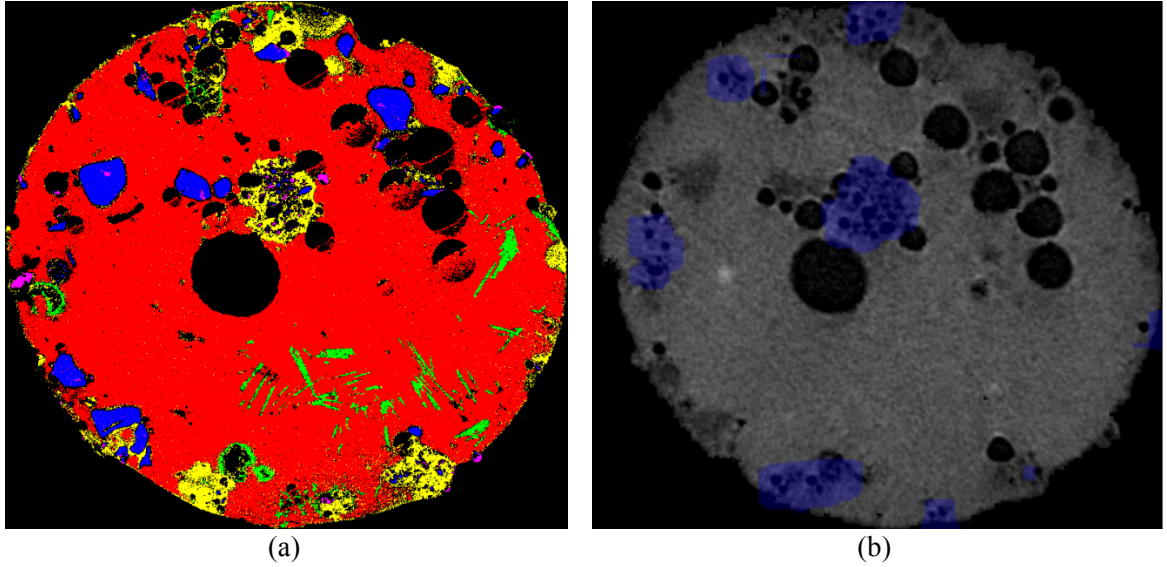
Figure 5.2 – Result of segmenting a porous phase: (a) Color Coded SEM; (b) Segmented μCT using CGF (blue color)

The CGF designed in this stage was then applied to other sections of the same particle, and the results (in blue) of segmenting one of these sections is presented in Fig 5.3.

For this cross section the ground truth is not available, but by manual comparing the section the phase in Fig 5.3(a) with Fig 5.1(c) (both of which belong to the same particle) we can see that the segmented regions shown in Fig 5.3(b) appear reasonable.
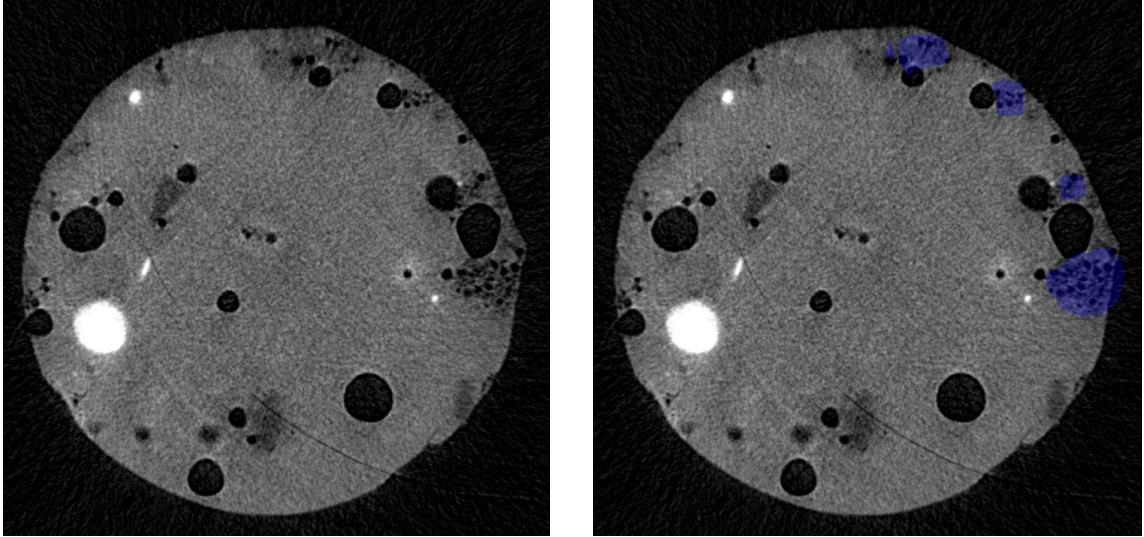
(a) Original µCT Image (b) Result of Segmentation (blue color)

Figure 5.3- Result of segmentation using the CGF designed using the ground truth data of Fig 5.1(c)
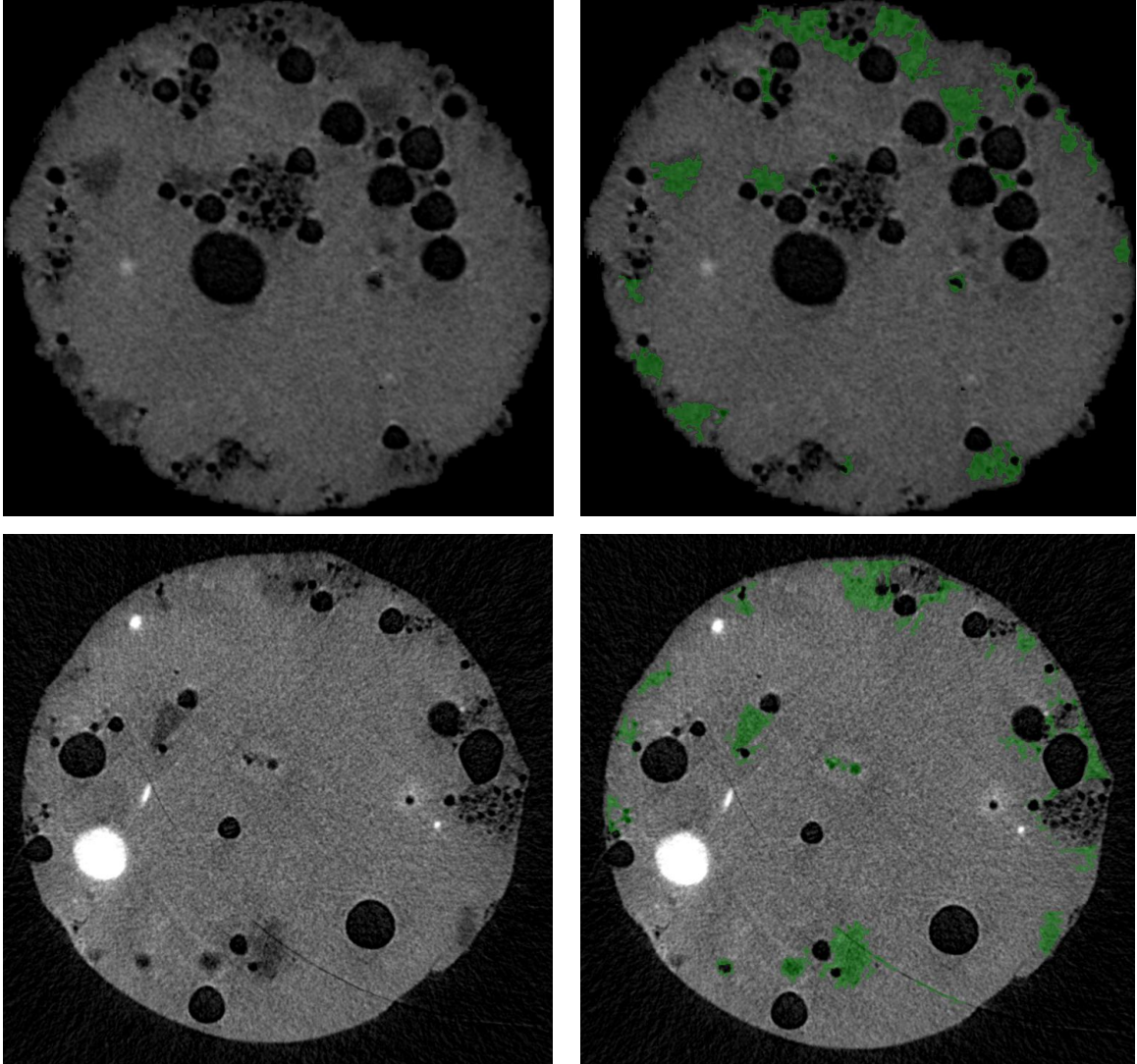
5.1.2 – Segmentation Using Histogram Matching

Segmentation using Histogram Matching and the results are presented in the PhD Preliminary Exam Report by the author [31]. As explained in that report, the contrast of the gray scale images were improved using two different threshold values, and by comparing the results, we segmented the regions with the highest difference in the intensity between the two results as a different phase. This technique segments the phase reasonably well, but the threshold values must be separately selected for every single µCT image. As explained in Chapter 2, we proposed two approaches to solve this problem. 1) Selecting one slice as a reference and finding the threshold values for segmenting it properly (compared to manual segmentation). Then for segmenting any other slice, first, using the "histogram matching technique" (Section 2.3 of this report), we change that slice's histogram such that it is as close as possible to the histogram of the reference image. Then using the same threshold levels that were used for segmenting the reference image, we improve the desired slice's contrast and conduct the segmentation. 2) The histogram of every slice can be represented by the summation of two Gaussian functions as shown in Fig 2.4(c). For

every slice we first generate an artificial histogram, composed of two Gaussian functions, similar

in size and shape to the two Gaussian functions creating the original histogram, but further apart.

Then using "histogram matching" we change that slice's histogram such that it matches the

artificially created histogram. Using a simple threshold, we can then separate into different

categories the pixels falling under each separated region, of the new histogram.

Since for every flyash particle, one cross section with ground truth (SEM scan) is available, we

used that slice as the reference slice for this technique and conducted the segmentation on the

remaining slices. The results (in green) of the segmentation using this technique on the slices used

in the previous section (Fig 5.1(c) and Fig 5.3(a)) are given in Fig 5.4. We first applied the

technique to the image in Fig 5.4(a) and found the best set of threshold values that segment the

regions of the different phases properly. We then used the histogram of that image and the

threshold set to segment the slice in Fig 5.4(c), which is another cross section of the same

particle, and the result (in green) of this segmentation is shown in Fig 5.4(d).

a b
c d

Figure 5.4 – Result of segmentation using histogram matching and contrast stretching – (a) μCT scan result of a cross section for which SEM is available; (b) Result (in green) of segmenting the slice in (a); (c) μCT scan result of another cross section of the same particle; (d) Result of segmenting the image in (c) (in green)

5.1.3 – Segmenting the Bright Spots

There are certain spots in some of the slices that are very bright. They represent a certain type of material, and since the brightness of these regions is noticeably higher than the rest of the pixels, we locate these spots by applying a simple gray scale threshold and mark them as another type of material. Fig 5.5 shows this segmentation in pink on the same slices segmented in Section 5.1.1 and 5.1.2.
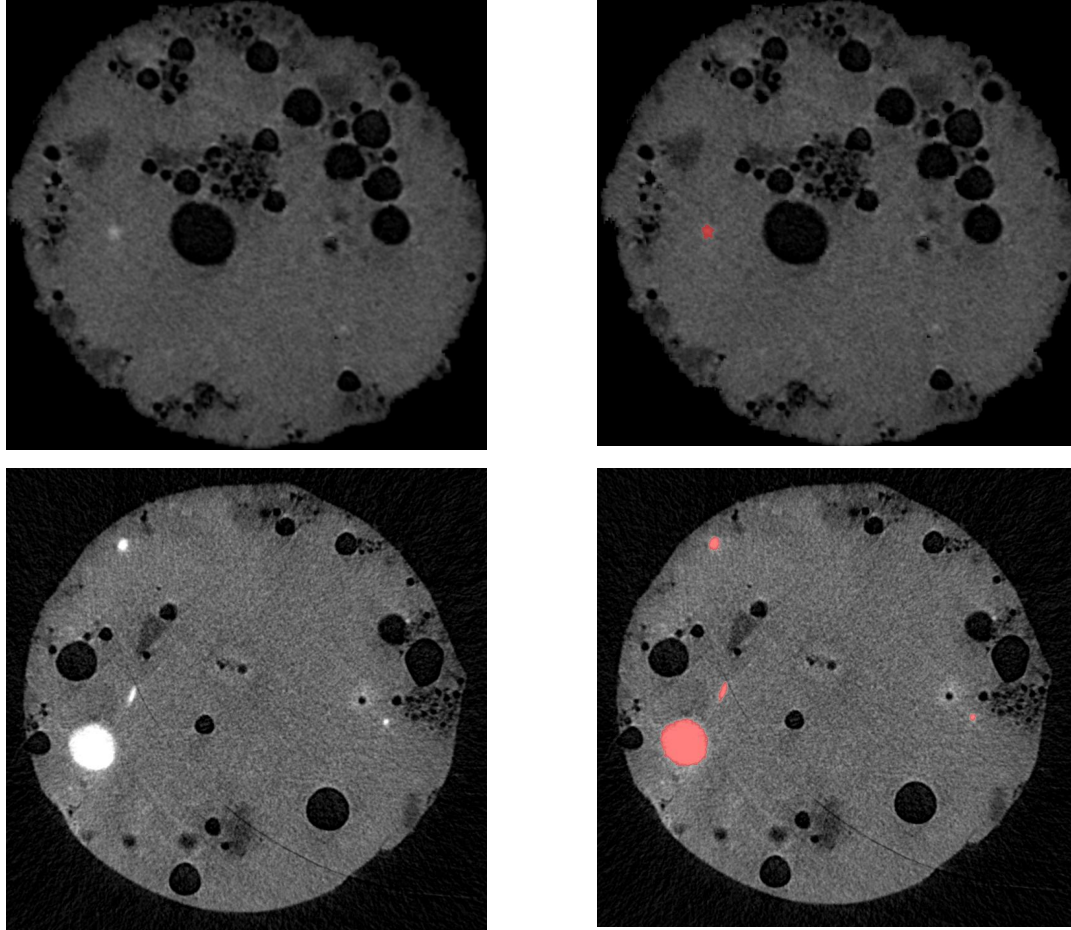
a b   Figure 5.5 – Result of segmenting the bright spots using gray scale threshold - (a) µCT
c d   scan result of a cross section of a flyash particle; (b) Result (in pink) of segmenting the
           bright spots on the slice in (a); (c) µCT scan result of another cross section of the same
           particle; (d) Result of segmenting the bright spots on the image in (c) (in pink)

5.2 – Combining all Techniques

The three techniques explained earlier are combined to provide a new approach to clustering

different phases in flyash particles, and each technique does not interfere with the others, such

that they can be applied to the gray scale image separately for segmenting different phases of

material. Figs 5.3(b) and 5.4(d) show the result of segmentation using CGF and Histogram

Matching techniques, respectively, and show different phases of material using different

techniques. Comparing these images, we note that there are some regions that are segmented by

both of techniques. As explained earlier in Section 2.3 (Inadequacies of Contrast Stretching and

Histogram Matching Technique), due to the gray values of the regions with porous phase, they are usually clustered in the same category as non-porous regions using the Contrast Stretching Technique. Since the CGF technique segments only porous phase, in our combined approach, we consider all the regions segmented by both techniques as regions of material with porous texture. In other words, we employ the CGF technique as the primary method for segmentation, and the remaining regions (pixels not segmented using CGF) are analyzed using the Histogram Matching technique for detecting different phases.

The segmentation procedure using combined techniques is diagramed in Figure 5.6. In order to perform segmentation for the μCT slices of each particle, two separate procedures are executed. First, a training procedure is used, through which a CGF is designed and the proper threshold for Contrast Stretching is selected (Fig 5.6(a)); then, in Fig 5.6(b) we employ our segmentation procedure in which all the gray scale images of different cross sections of the particle are processed and different phases of material are color marked.

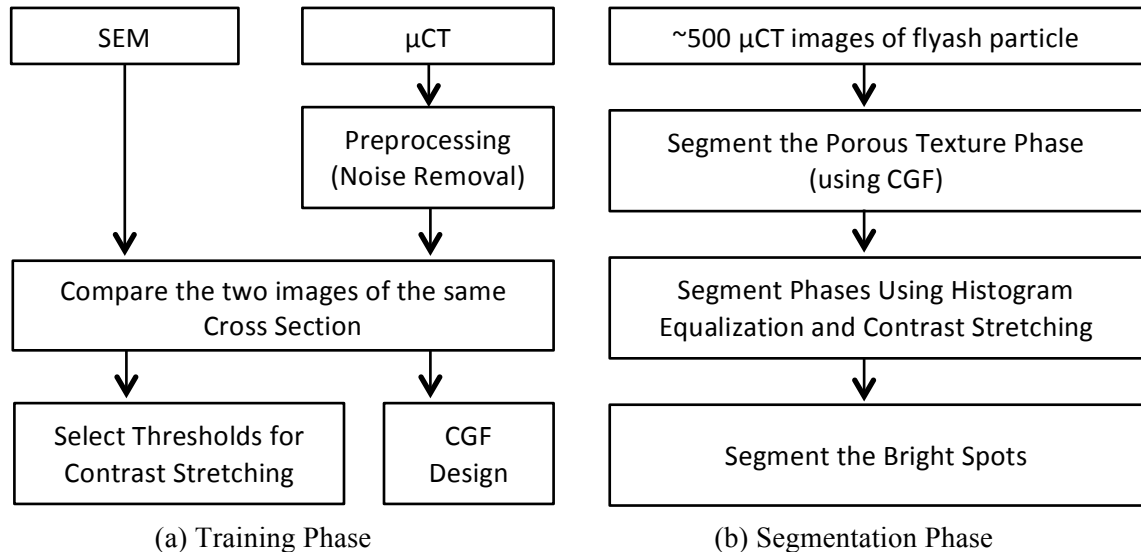(a) Training Phase   (b) Segmentation Phase

Figure 5.6 – The segmentation procedure combining all techniques

The result of segmentation on the slices shown in the previous section after combining all of the techniques is presented in Fig 5.7, together with the original images. In these figures, different colors represent different phases of material. In Figs 5.7(b) and (d) the porous phase is marked with blue. Then, the contrast stretching technique is applied to the remainder of the image and the detected phase is marked with green. And finally, the gray scale threshold is applied to the result and the bright spots which contain another phase of material are segmented and are represented with red in these figures. Comparing the regions of different phases of material, segmented by our technique, with the SEM result, available for only one cross section of a flyash particle (in this case only available for the section shown in Fig 5.7(a)), we note that regions segmented in different steps of our technique (CGF, Contrast Stretching, Gray Scale Thresholding) contain different phases. For that reason we segmented them in separate groups and color marked them differently.
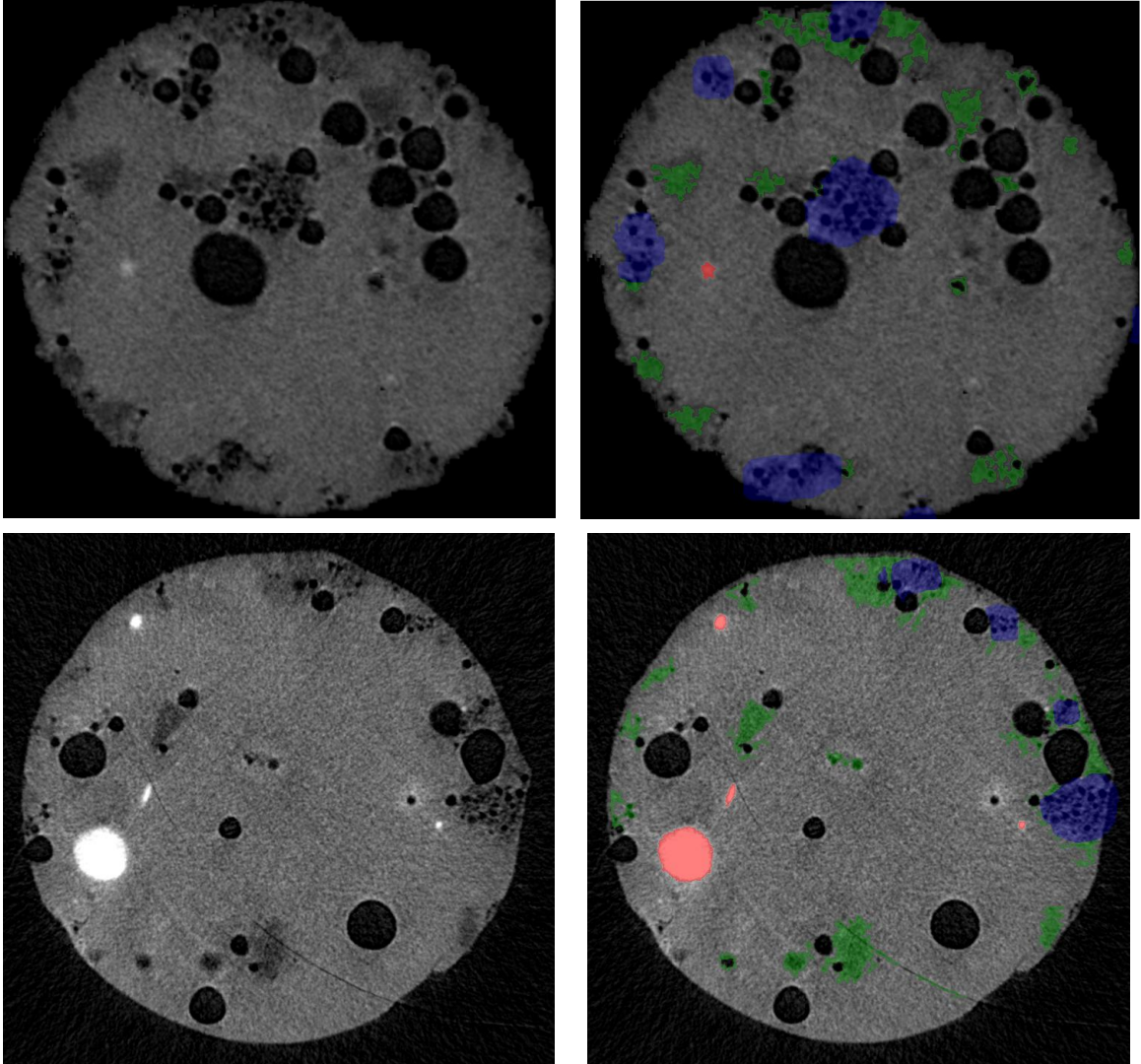
a b   Figure 5.7 – Result of segmentation on two sample slices of a fly ash particle after
c d   combining all the proposed techniques. Different colors in the image represent different
         phase of material detected. (a) µCT scan result of a cross section of a flyash particle; (b)
         Result of segmentation on the slice in (a); (c) µCT scan result of another cross section of
         the same particle; (d) Result of segmentation on the image in (c)

Figure 5.8 shows the result of segmentation using this approach in 4 other cross sections, which

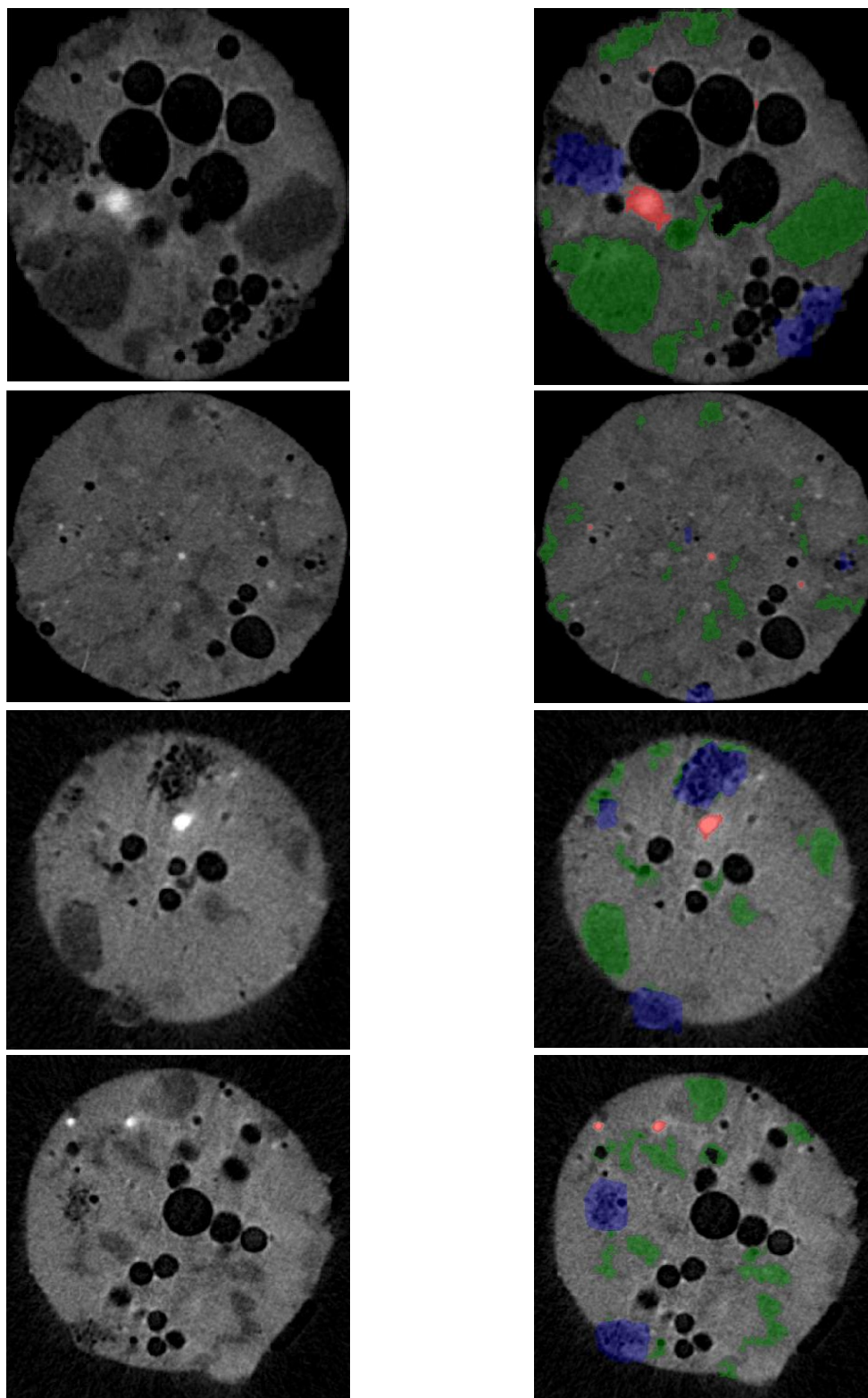belong to 4 different flyash particles.

Figure 5.8 – Result of segmentation on cross sections from 4 different flyash particles – In each row, the images on the right is the result of segmentation of the image on the left

5.3 – Creating a 3D model of the particle

The segmentation technique can be applied to all of the slices of a particle, and by putting this data together, we can create a 3D model of the particle for better understanding of the locations of the different phases of material in the particle. The 3D visualization of the data was done in the AMIRA [38] software program, and the results are shown in Fig 5.9 to 5.12. In these figures different phases of flyash particles are shown in different colors; the phases detected using a Gabor filter, histogram matching, and gray value thresholding are presented in blue, green and yellow, respectively. In Fig 5.9 to 5.12, figures (a) and (b) show a side view and the top view of the particles, and in Fig 5.9(c), a perspective view of the same particle is presented. In figure (c), the gray transparent layer covering the particle defines the outer shell of the particle.

(a)

(b)
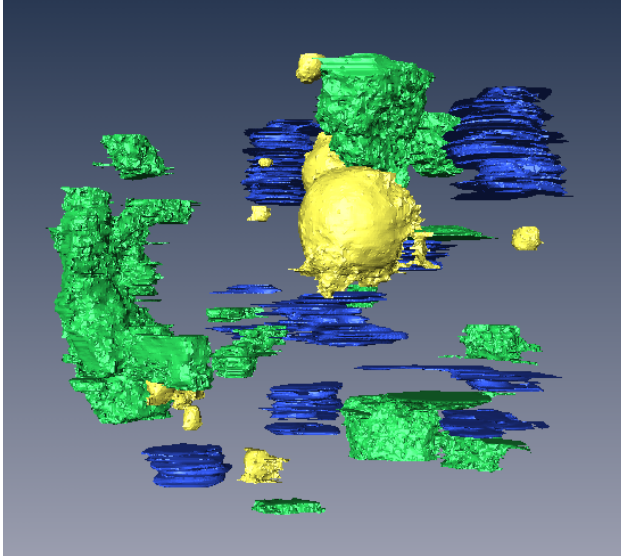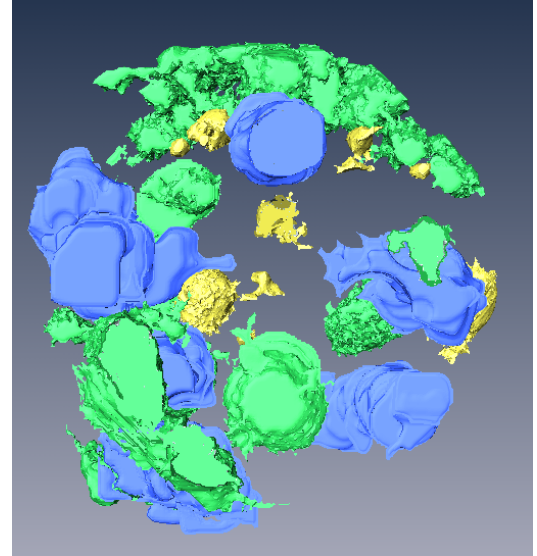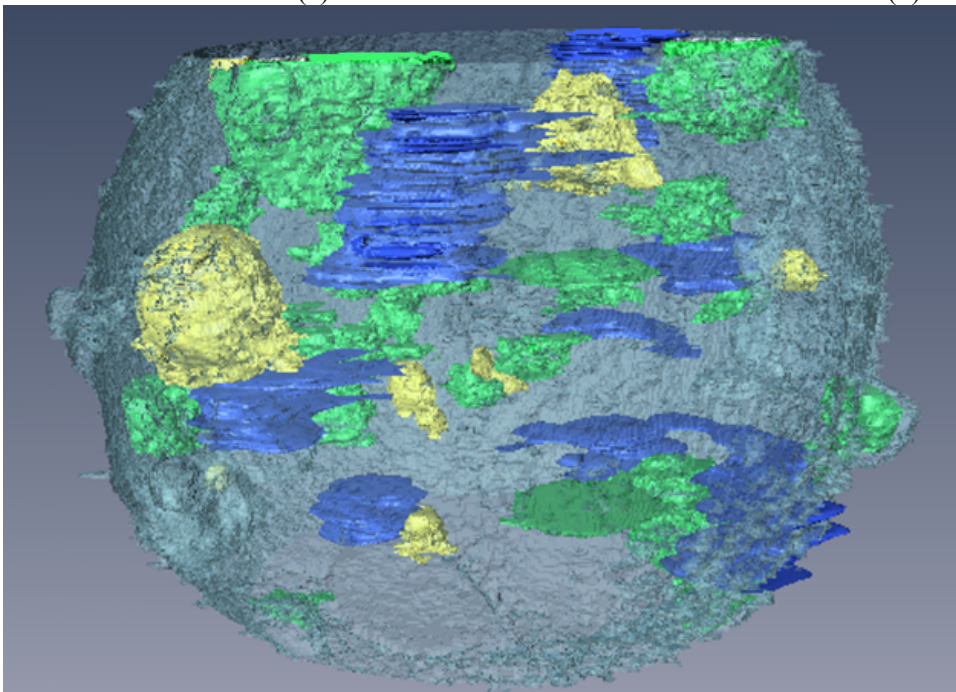
Figure 5.9 – Particle 1; 3D model of a flash particle generated by AMIRA [38]; (a) side view (b) top view (c) perspective view

(c)

(a)

(b)
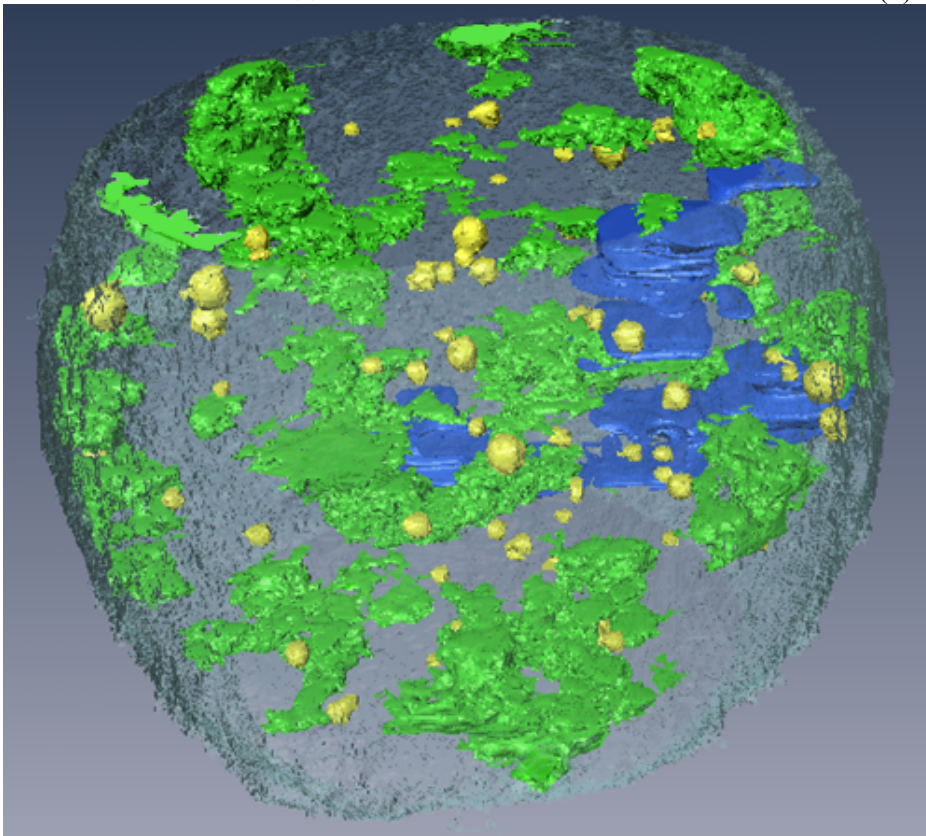
Figure 5.10 – Particle 2; 3D model of a flash particle generated by AMIRA [38]; (a) side view (b) top view (c) perspective view

(c)

(a)

(b)
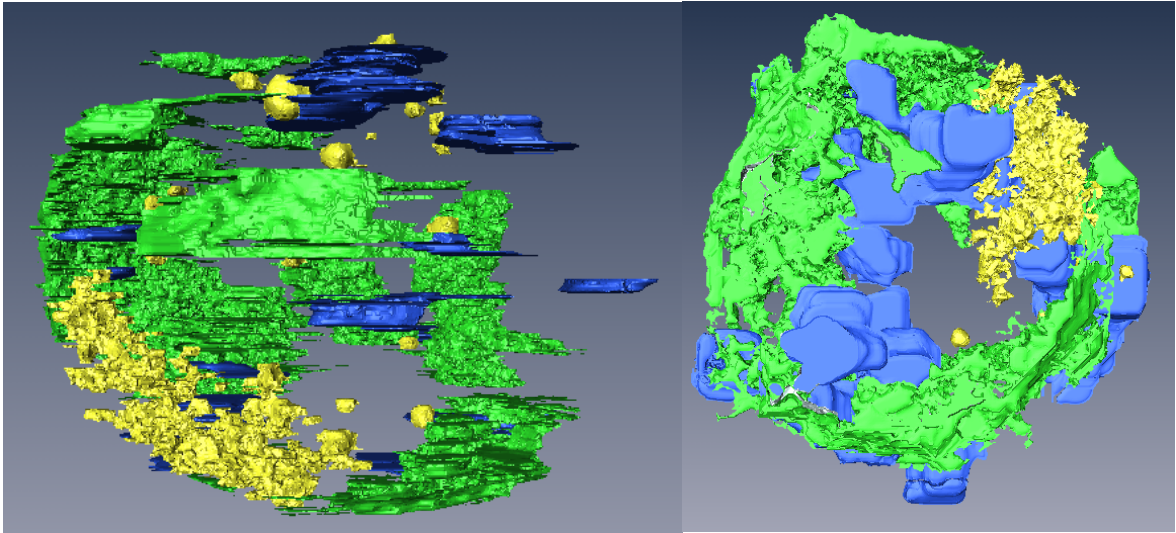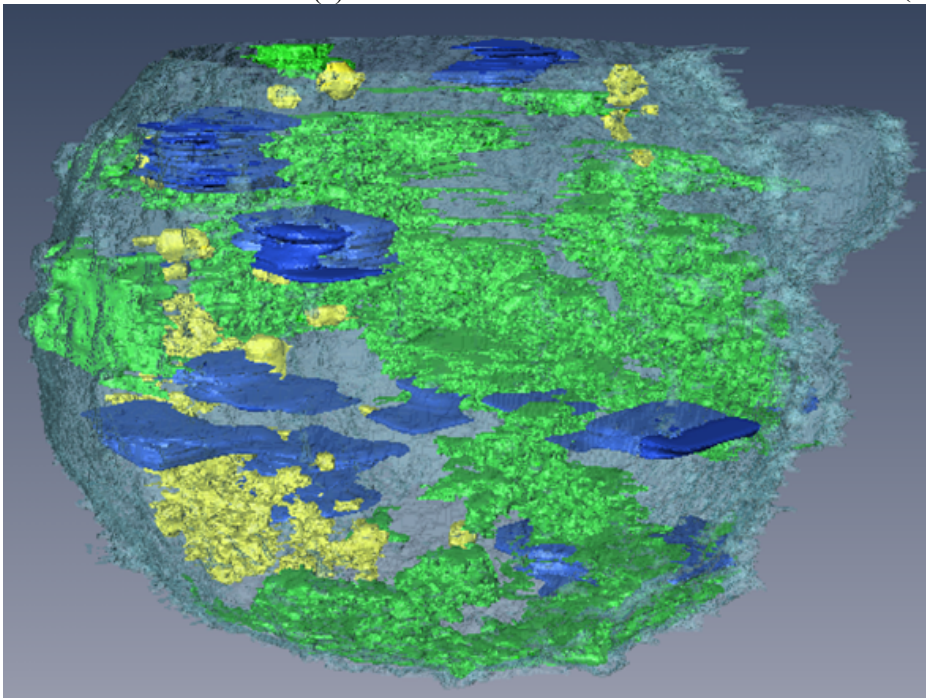
Figure 5.11 – Particle 3; 3D model of a flash particle generated by AMIRA [38]; (a) side view (b) top view (c) perspective view
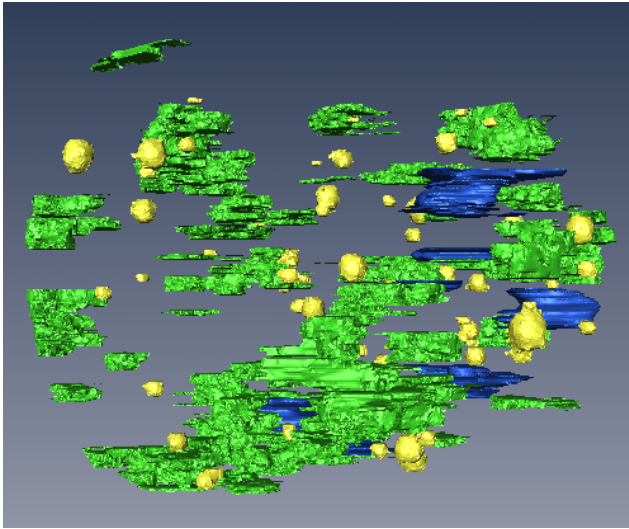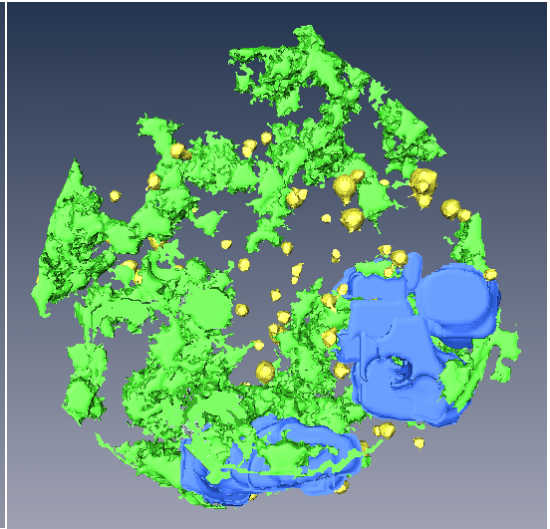
(c)

(a)

(b)

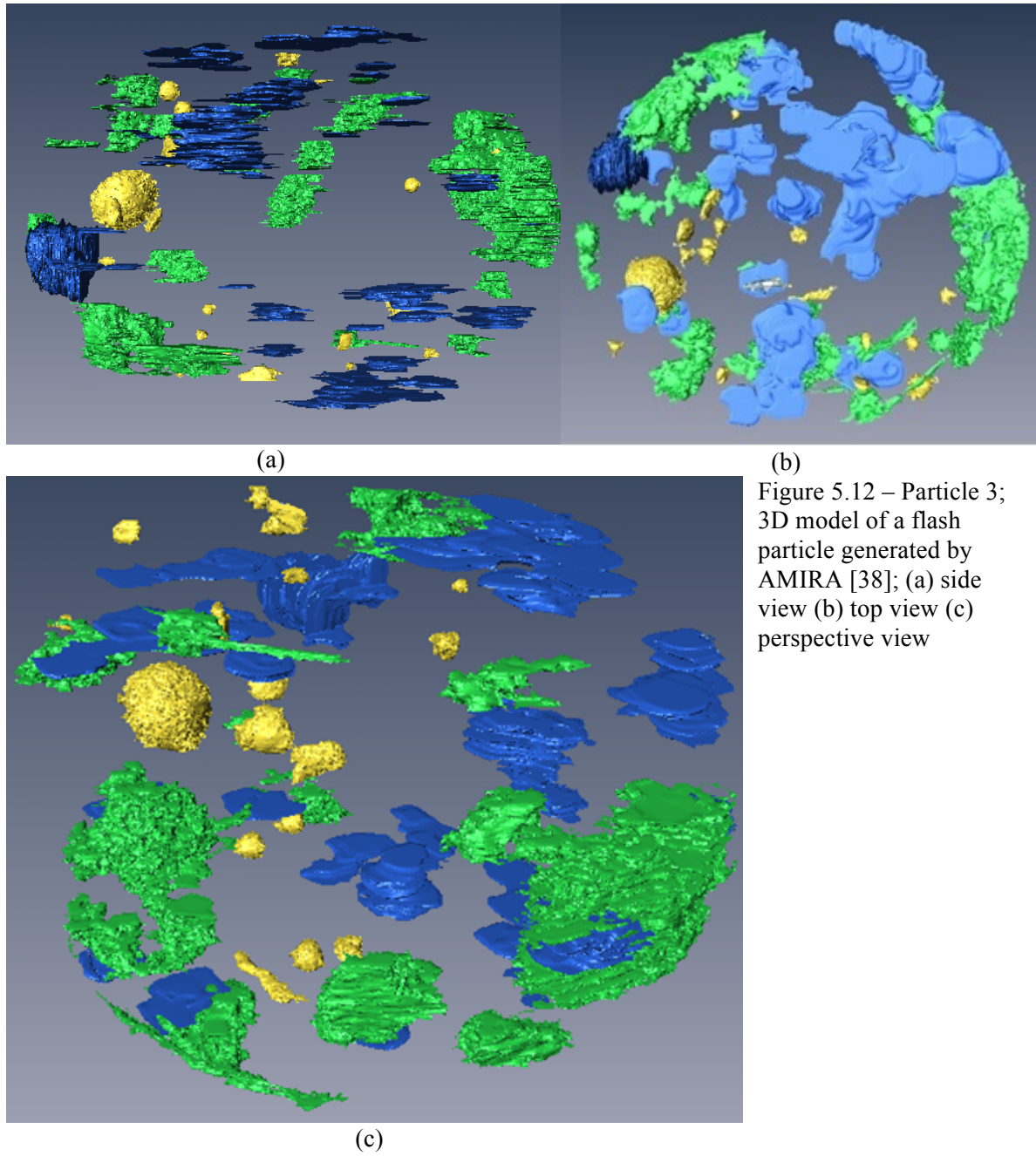Figure 5.12 – Particle 3; 3D model of a flash particle generated by AMIRA [38]; (a) side view (b) top view (c) perspective view

(c)

The volumetric percentages of different phases in each of the particles (shown in Fig 5.9 to Fig 5.12) are presented in Table 5.1. In this table "Phase1" is the phase detected by gray scale thresholding (the bright spots in the gray scale image); "Phase2" is the phase segmented using

histogram matching and "Phase 3" is segmented using Circular Gabor Filter. Phases 1,2 and 3 are presented in yellow, green and blue respectively in Figures 5.9 to 5.12.

	Phase 1 (%)	Phase 2 (%)	Phase 3 (%)	Total (%)
Particle 1 (Fig 5.8)	1.19	7.39	4.27	12.85
Particle 2 (Fig 5.9)	0.36	2.82	3.42	6.6
Particle 3 (Fig 5.10)	0.67	18.41	5.94	25.02
Particle 4 (Fig 5.11)	0.42	7.63	2.80	10.85
Average	0.66	9.06	4.11	

Table 5.1 – Volumetric Percentage of different phases in the particles shown in Fig 5.8 to 5.11

As this table shows, the volumetric percentages of material phases vary widely over the 4 particles, from a low of 6.60% to a high of 25.02%. On average phase 1 appears in the smallest amount, while phase 2 appears in the largest.

5.4 – Original Contributions of this Study

In summary, the original contributions of this work are:

1 – A technique for sizing a circular Gabor filters such that it has the maximum response to regions with porous patterns.

2 – Use of histogram matching for segmenting the patterns based on their gray scale values, even when these values are very similar.

3 – Improved accuracy of techniques for segmenting different phases of flyash particles.

4 – Use of image-processing techniques for noise removal of gray scale images attained by X-Ray scanners to improve segmentation accuracy.

5.5 – Future Work

We suggest that the training technique for constructing Circular Gabor Filters (explained in Section 3.2) can be applied to other segmentation problems, enabling detection of different textures (after properly training with sample "ground truth" regions entered into the program). In follow-on work, we recommended examining this. Medical imaging appears to hold some promise.

To render the training phase more accurate, the system might be improved by using more data, instead of entering only one sample region as the training set. By entering different regions (containing the same phase) and finding the best sized CGF capable of segmenting all these regions properly, one might find an improved CGF to be used for segmenting the remaining cross sections of that flyash particle. Usually, in every cross section of a flyash particle, there is more than one phase with porous texture, and all these regions might be used for training. If more than one SEM test could be conducted on a flyash particle, more sample regions could be entered to make the designed CGF more accurate.

REFERENCES

Note: Please read the directions in the following paragraph very carefully before proceeding.

[1] Commission on Energy and the Enviroment, 1981. Coal and the Environment. HMSO, London, 257pp.

[2] Lightman, P. & P. J. Street, 1983. Single drop behaviour of heavy fuel oils and fuel oil fractions. J. Inst. Energy 56: 3–11

[3] Goldberg, E. D., 1985. Black Carbon in the Environment: Properties and Distribution. Wiley Interscience Publication, New York, 198pp.

[4] Raask, E., 1984. Creation, capture and coalescence of mineral species in coal flames. J. Inst. Energy 57: 231–239.

[5] Rose, N. L.. 1996. Inorganic fly-ash spheres as pollution tracers. Envir. Pollut. 91: 245–252.

[6] Disposal and market sources of flyash, Wikipedia (Aug, 2013)

[7] Environmental Building News, Vol 18, No. 2

[8] ASTM – C618-12, Standard specification for Coal Fly Ash and Raw or Calcined Natural Pozzolan for Use in Concrete

[9] Sai Venu Gopal Lolla, New Techniques for clustering, selection of number of histogram bins, and estimation of quantiles of pairwise distances, Ph.D. Dissertation, Oklahoma State University, Dec 2011.

[10] T. Lindeberg, Scale-Space Theory in Computer Vision. Norwell, MA, USA: Kluwer Academic Publishers, 1994.

[11] J. B. T. M. Roerdink and A. Meijster, "The watershed transform: Definitions, algorithms and parallelization strategies," Fundamenta Infomaticae, vol. 41, no. 1-2, pp. 187–228, 2000..

[12] M. Bicego, M. Cristani, A. Fusiello, and V. Murino, "Watershed-based unsupervised clustering," in Rangarajan et al. [68], pp. 83–94.

[13] Dr. Tyler Ley's research team report on Sep 26th 2012

[14] Anita Khanna, Meenakshi Sood, and Swapna Devi, "US Image Segmentation Based on Expectation Maximization and Gabor Filter" International Journal of Modeling and Optimization, Vol.2, No. 3, June 2012

[15] J. A. Nobel, "Ultrasound Image Segmentation; A Survey," IEEE Transactions on Medical Imaging, vol. 25, no. 8, 2006

[16] M. Sivalingamaiah, B. D. Venakramana Reddy, "Texture Segmentation Using Multichannel Gabor Filtering" IOSR Journal of Electronics and Communication Engineering Volume 2, Issue 6 (Sep-Oct 2012), PP 22-26

[17] Xuewen Wang, Xiaoqing Ding, Changsong Liu, "Gabor filters-based feature extraction for character recognition" Journal of Pattern Recognition Vol 38 (2005), PP 369-379

[18] X. Wang, X. Ding, et al., A gray-scale image based character recognition algorithm to low quality and low resolution images, Document Recognitiotn and Retrieval VIII, Electronic Imaging 2001, San Jose, CA, USA

[19] L. Wang, T. Pavlidis, Direct gray-scale extraction of features for character recognition, IEEE Trans. PAMI 15 (10) (1993) 1053-1066

[20] D.R. Cowan, G.R.J. Cooper, "Merging radiometric grids using histogram matching", Journal of Computer and Geosciences Vol. 34 (2008)

[21] Neeru Jaiswal, C.M. Kishtawal, P.K. Pal, "Cyclone intensity estimation using similarity of satellite IR images based on histogram matching approach", Journal of Atmospheric Research Vol. 118 (2012)

 [22] Yiheng Liu, Yanmei Liang, Zhengrong Tong, Xiaonanong Zhu, Guoguang Mu, "Contrast enhancement of optical coherence tomography images using least squares fitting and histogram matching", Journal of Optics Communication Vol. 279 (2007)

[23] Rafael C. Gonzalez, Richard E Woods, Steven L. Eddins [2009], "Digital Image Processing using MATLAB", 3rd ed., Gatesmark Publishing, p. 84

[24] Rafael C. Gonzalez, Richard E Woods, Steven L. Eddins [2009], "Digital Image Processing using MATLAB", 3rd ed., Gatesmark Publishing,, p. 103

[25] Aach, T.; Kaup, A.; Mester, R.: ,On texture analysis: Local energy transforms versus quadrature filters." In Signal Processing, vol. 45, pp. 173-181, 1995

[26] D. Scharstein and R. Szeleiski, "A taxonomy and evaluation of dense two frame stereo correspondence algorithm," International Journal of Computer Vision, vol. 47, no. 1/2/3, pp. 7-42, 2002

[27] J. G. Daugman. Uncertainty relation for resolution in space, spatial frequency, and orientation optimized by two-dimensional visual cortical filters. Journal of the Optical Society of America A, 2(7):1160–1169, July 1985.

[28] D. J. Field, Relation Between the Statistics of Natural Images and the Response Properties of Cortical Cell, J. Opt. Soc. Am. A. 4, 2379-2394 (1987).

[29] A. C. Bovik, N. Gopal, T. Emmoth, and A. Restrepo, Localized Measurement of Emergent Image Frequency by Gabor Wavelets", IEEE Trans. on Inf. Theory, 8,2,691-712(1992).

[30] O. Nestares, R. Navarro, T. Portilla, and A. Tabernero, Efficient Spatial-domain Implementation of Multiscale Image Representation Based on Gabor Functions. J. Electronic Imaging, 7, 166-173 (1998).

[31] J. Portilla, R. navarro, O. nestares, and A. Tabernero, Texture Synthesis-by-Analysis Based on a Mutiscale Early Vision Model, Optical Engineering, 35, pp. 2403-2417 (1996).

[32] A.K. Jain and F. Farrokhnia, Unsupervised Texture Segmentation Using Gabor Filters, Pattern Recognition, Vol.24, No.12 (1991), pp1167-1186

[33] Ihara, Shunsuke (1993). Information theory for continuous systems. World Scientific. p. 2. ISBN 978-981-02-0985-8.

[34] H. Pohl, O. Weibrecht, and U. Wiesenburg, "Arrangement for control of aerial cameras," US Patent 3997795, filed 4-23-1975.

[35] T.J. Keating, P.R. Wolf, and F.L. Scarpace,"An Improved Method of Digital Image Correlation," Photogrammetric Engineering and Remote Sensing 41(8):993-1002,(1975)

[36] Ali Asmari, "PhD Preliminary Exam Report" Department of Mechanical and Aerospace Engineering, Oklahoma State University, 2012

[37] All SEM and µCT data provided by Dr. Tyler Ley, Associate Professor of Civil and Environmental Engineering, Oklahoma State University, Stillwater, OK, and his research group throughout personal communication Aug 2012 – September 2013

[38] http://en.wikipedia.org/wiki/Amira_(Software)

[39] http://en.wikipedia.org/wiki/Hough_transform

VITA

Ali Asmari

Candidate for the Degree of

Doctor of Philosophy

Thesis: CLUSTERING FLYASH PARTICLES USING IMAGE PROCESSING TECHNIQUES

Major Field: Mechanical Engineering

Biographical:

Education:

Completed the requirements for the Doctor of Philosophy in Mechanical Engineering at Oklahoma State University, Stillwater, Oklahoma in July, 2014.

Completed the requirements for the Master of Science in Mechanical Engineering at Oklahoma State University, Stillwater, Oklahoma in December, 2011.

Completed the requirements for the Bachelor of Science in Mechanical Engineering at Ferdowsi University, Mashhad, Iran in 2009.